INFORMATION RETRIEVAL FROM MOIRÉ
FRINGE PATTERNS IN THERMAL
STRAIN FIELDS

By

DONALD L. G. STURGEON

UNIVERSITY OF FLORIDA

April, 1966

ACKNOWLEDGMENTS

TABLE OF CONTENTS

TABLE OF CONTENTS (Continued)

LIST OF TABLES

LIST OF FIGURES

LIST OF SYMBOLS

a	Defocal length or interior radius of a ring or a constant
a_p	Weight functions of a linear in-phase filter
a_p^*, a_n	Shannon's coefficients
$A(f)$	Real part of $H(f)$
$A_o(x,y)$	Amplitude distribution over the output plane
$\bar{A}_o(\omega_x, \omega_y)$	Fourier transform of A_o
$A_{in}(x,y)$	Amplitude distribution over the input plane
$\bar{A}_{in}(\omega_x, \omega_y)$	Fourier transform of A_{in}
b	Exterior radius of a ring or a constant
b_p	Weight functions of a linear in-quadrature filter
C	Contrast of the object test target
$c^i(\omega)$	Contrast of the image at spatial frequency ω
$c^o(\omega)$	Contrast of the object at spatial frequency ω
C_o, C_1, C_2	Constants
d	Diameter of the aperture
D	Photographic density unit
$D(x)$	Photographic film density in the x direction
$D_n(x)$	Negative film density in the x direction
DCR	Dynachem Photo Resist

E	Modulus of elasticity or film exposure
E_{avr}	Modulus of elasticity for average temperature
$E_n(x)$	Negative exposure variation along the x direction
f	Spatial frequency
f_α	Highest frequency present in the raw signal
f_o	Center frequency of the desired signal
f_c	Cut-off frequency of the desired signal
f_t	Highest frequency of the desired signal
Δf	Band width
Δf_1	Roll-off frequency interval
$f(\alpha,\beta)$	Complex amplitude distribution over the surface of the aperture
$f^*(\alpha,\beta)$	Complex conjugate of $f(\alpha,\beta)$
G	Shear modulus
G_{avr}	Shear modulus for average temperature
h	Sampling wavelength
$h(x)$	Impulse response of a linear system
$h_A(x,y)$	Amplitude response to a point source
$\overline{H}_A(\omega_x,\omega_y)$	Fourier transform of $h_A(x,y)$
$h_I(x,y)$	Intensity response to a point source
$\overline{H}_I(\omega_x,\omega_y)$	Fourier transform of $h_I(x,y)$
$H(f)$	Filter transfer function

$\bar{H}(f)$ Infinite series approximation to H(f)

$\bar{H}_N(f)$ Finite series approximation to H(f)

i Summation variable, summation limit or $\sqrt{-1}$

$I(x)$ Intensity variation in the x direction

I_o Background intensity

I_1 Intensity amplitude coefficient

I Intensity of a point source

$I_{in}(x,y)$ Intensity distribution over the input plane

$\bar{I}_{in}(\omega_x,\omega_y)$ Fourier transform of $I_{in}(x,y)$

$I_o(x,y)$ Intensity distribution over the output plane

$\bar{I}_o(\omega_x,\omega_y)$ Fourier transform of $I_o(x,y)$

$I^*(x)$ Signal plus noise intensity function

I_{max} Maximum of a sinusoidal intensity function

I_{min} Minimum of a sinusoidal intensity function

I^*_k Digitalized version of $I^*(x)$

$\tilde{I}^*_k$ Finite series approximation to I^*

$\tilde{I}_k$ Filtered version of I^*_k

$I_q(x)$ In-quadrature intensity function

$(I^*_q)_k$ Digitalized version of $I^*_q(x)$

$(\tilde{I}^*_q)_k$ Finite series approximation to $I^*_q(x)$

$(\tilde{I}_q)_k$ Filtered version of $(I^*_q)_k$

j	Summation variable
J_1	Bessel function of the first order
k	Parameter defining extent of parabolic transition in an Ormsby filter, summation limit , $2\pi/\lambda$, or data point number
KPR	Kodak Photo Resist
L	Radius of a lens or a linear operator
ℓ_o	Initial length
ℓ_f	Final length
m	Summation limit
$\lvert M \rvert$	Real part of a complex transmittance
MTF	Modulation transfer function
$M_o(\omega)$	Modulation transfer function of the photo-optical system
$M_F(\omega)$	Modulation transfer function of a film
$M_L(\omega)$	Modulation transfer function of a lens
N	Summation limit
$N(x)$	Noise content of a signal
n	Summation variable
p	Master grid pitch or summation variable
r	Summation variable , radial coordinate of a lens disk or ring
s	Summation limit

LIST OF SYMBOLS (Continued)

t	Time
T	Transmittance or temperature
T_n	Transmittance of a negative
T_p	Transmittance of a positive
$T_{max}(\omega)$	Maximum of a sinusoidal transmittance function at frequency ω
$T_{min}(\omega)$	Minimum of a sinusoidal transmittance function at frequency ω
$U(x)$	Displacement function in the x direction
u	Object distance
u_k	Digitalized version of $U(x)$
$\bar{u}_k$	Filtered version of u_k
v	Image distance
w_r	Weights of a smoothing filter
x	Cartesian coordinate or raw input to analog circuit
$\bar{X}$	Filtered output from analog circuit
$\dot{\bar{X}}$	Filtered and derived output from analog circuit
x_o	Particular value of x
y,z	Cartesian coordinates
α	Summation variable or angular coordinate, analog filter parameter or thermal expansion coefficient
α_{avr}	Thermal expansion coefficient for average temperature, angular coordinate or analog filter parameter
β_o	Frequency location of a maximum in the transfer function of an annular aperture

LIST OF SYMBOLS (Continued)

γ	Slope of the straight line portion of the characteristic curve of a film
γ_n	Slope of the straight line portion of the characteristic curve of a negative film
γ_P	Slope of the straight line portion of the characteristic curve of a positive print
δ	Distance between fringes
$\delta(x)$	Input to a linear system
ϵ	Eulerian strain or a variable
ϵ_k, ϵ_n	Digitalized raw value of the strain
$\bar{\epsilon}_k, \epsilon_n'$	Filtered version of ϵ_k
$\bar{\epsilon}$	Natural strain
ϵ^E	Eulerian elastic strain component
ϵ^P	Eulerian plastic strain component
ϵ^T	Eulerian total strain
ϵ_θ	Eulerian circumferential strain
ϵ_r	Eulerian radial strain
ϵ_{avr}	Average strain in a traction sample
η	Limit of integration
$\theta(f)$	Argument of $H(f)$
λ	Spatial or light wavelength
$\lambda_o, \lambda_c, \lambda_t$	Center, cut-off and shortest spatial wavelength in the desired signal
μ	Mean value of a random variable
ν	Poisson's ratio
ν_{avr}	Poisson's ratio for the average temperature

xiv

LIST OF SYMBOLS (Continued)

$\rho(x)$	Argument function of the coordinate x
σ	Normal stress
σ_s	Yield stress of stainless steel
σ_θ	Normal circumferential stress
σ_r	Normal radial stress
$\varphi(x)$	Output of a linear system
$\Phi(f)$	Fourier transform of $\varphi(x)$
$\psi(x)$	Input to a linear system
Ψ	Fourier transform of $\psi(x)$
$\Phi(x)$	Complex intensity function
φ_n, ψ_n	Sampled version of $\varphi(x)$ and $\psi(x)$
$\overline{\varphi}_n$	Finite series approximation to φ_n
ω	Spatial frequency
ω_x, ω_y	Spatial frequency in a given direction
ω_r	Spatial frequency in the radial direction

Abstract of Dissertation Presented to the Graduate Council
in Partial Fulfillment of the Requirements for the
Degree of Doctor of Philosophy

INFORMATION RETRIEVAL FROM MOIRÉ FRINGE
PATTERNS IN THERMAL STRAIN FIELDS

By

Donald L. G. Sturgeon

April, 1966

Chairman: Dr. C. A. Sciammarella
Major Department: Engineering Science and Mechanics

This research deals with the implementation of a linear filter-
ing system capable of yielding the strains in a solid body from the
information on the displacement field contained in the light intensity
trace of moiré fringes.

An analysis of the photo-optical device used to produce and
record the fringes illustrates quantitatively the filtering abilities
of the lens-film combination. Solutions to the non-linear sensitometric
characteristics of the film are applied to moiré data.

Several experiments of optical filter synthesis that increase
substantially the quality of recorded patterns are reported.

The retrieval of the meaningful phase modulation of the light
intensity trace from the spurious amplitude and phase variations due to
noise is successfully accomplished by the implementation of numerical
filters in quadrature. This is used to determine new bounds on auto-
matic fractional moiré fringe interpolation.

The numerical differentiation of the empirically determined displacement curve is critically reviewed and a significant increase in the accuracy of this process is obtained by the use of several numerical methods.

Necessary techniques of model grid engravure able to withstand high temperatures are developed.

The above improvements on the moiré method are used to measure thermal strains in stainless steel rings, under steady state thermal loading, up to a maximum temperature of $1600^{\circ}F$.

CHAPTER I

INTRODUCTION

The moiré method has the inherent capability of performing
large field strain determinations in such important areas of solid
mechanics as elasticity, viscoelasticity, plasticity and fracture,
under mechanical, thermal, static and dynamic loading conditions.

In some of these fields the experimental stress analyst has a
choice of several applicable methods, in others, moiré today offers
the only possible solution.

It is unnecessary to review here the history of the development
of the moiré method as an experimental stress analysis tool. Complete
chronological listings of work performed on this subject are available
[1, 2].

Though in principle the method can yield the information which
we desire on the strain field in the body, not always does this come
in a convenient and direct form. A certain degree of sophistication
in the photo-optical instrumentation involved is therefore necessary
if the required degree of sensitivity and accuracy in the quantitative
results is to be achieved.

In this connection it is important at this early stage of our
presentation to stress as fundamental the difference between the dis-
crete and the continuous approach to the information contained in the
moiré fringes as was explained by Sciammarella [3].

1

The foundation of what will be said in this entire work will be found in the moiré light intensity-displacement law derived by Sciammarella [3] and tested by Ross, Sciammarella and Sturgeon [4].

We accept therefore that the displacement component in the direction normal to the master grid at a point in the deformed body is related in a continuous form to the light intensity at that point by the expression

$$U(x) = \left\{ \frac{1}{2\pi} \text{ arc cos } \frac{I(x)-I_o}{I_1} \right\} p \qquad (1.1)$$

where the coordinate x is measured in the direction normal to the master grid.

It has been shown [4] that by the proper use of (1.1) it is possible to increase the sensitivity and accuracy of the moiré method using coarse grids of 300 lines per inch far beyond the bounds set by the discrete theory [5]. Furthermore, it was shown that the processing of moiré data could be made almost totally objective when instrumentation was designed to perform the operations made by hand in the discrete approach [6].

The principal goal of this research was to implement an experimental setup capable of performing quantitative strain determinations with sufficient accuracy in metals at high temperatures by the moiré method.

Since a careful systems analysis of the entire moiré process was thought to be indispensable to achieve our purpose, several auxiliary tests under mechanic loading had to be performed whenever these

helped to clarify aspects of our analysis. Traction tests on bars and compression tests on disks were made for this purpose.

The optical synthesis of moiré data, not previously attempted, seemed to offer interesting possibilities to filter out the inevitable photographic noise present in all moiré patterns obtained under anything but the ideal conditions of illumination and surface characteristics. This matter was therefore pursued and definite improvements in the quality of the moiré patterns were obtained.

Previous to this research, an electronic band-pass filter able to operate between 0.02 cps and 2000 cps, had been used to filter both high and low spurious spatial frequencies from the moiré light intensity trace [6]. By means of an initial mismatch the frequency of the moiré signal before and after deformation was made to fall within the range of the instrument.

However, the inclusion of the electronic filter caused large oscillations of long duration on the analog voltage output of the photo-reading device every time a negative was introduced or removed from the electro-optical circuit. The decay time of these oscillations, caused by the response of the instrument to a step load, was found to be in excess of one hour.

Furthermore, the displacement information due to the deformation of the solid body had to be obtained as the difference between the final and initial pattern. When strong mismatch was present, in conjunction with small deformations, this difference between two large quantities of approximately the same magnitude impaired the accuracy of the procedure.

Since the amplitude variations were not corrected by the electronic filter, a numerical normalization technique was necessary in the digital program that handled the moiré data [6]. The errors involved in this step were found to be considerable and are discussed fully in [6].

As an alternative to the above procedure, numerical filtering with the aid of a digital computer was introduced here as a means of retrieving the meaningful spatial phase modulation of the light intensity trace from the spurious variations of phase and amplitude. This was possible by the implementation of in-quadrature filters that not only removed all the unwanted frequency components of the signal with no transient perturbations, but also produced an output completely independent of the amplitude of the moiré light intensity trace. This was instrumental in establishing the practical bounds on the fractional fringe interpolation that is possible by application of the continuous law (1.1).

The differentiation process that enables us to obtain the strains from the displacement field was also given a good deal of attention. A critical evaluation of several differentiation procedures of experimental data was made. This permitted a considerable increase in the accuracy of the strain determination which is perhaps the single most undesirable feature of the moiré method as applied to experimental stress analysis.

We mentioned at the beginning of this introduction several possible applications of the moiré method in solid mechanics; none is more challenging than the measurement of strains in metals subjected to

thermal loading. In this case the absolute value of the strains and of their difference across the body are small, so both the sensitivity and accuracy of the method of measurement are factors of primary importance.

Therefore, the ability of moiré to produce good results under these conditions is a suitable test of excellence for the entire system performance. Such results were obtained in this research.

The extension of the moiré method to high temperatures, at which conventional photoengravure techniques of model line printing fail because the photosensitive materials used burn off, required the establishment of new methods of grid manufacture. Several such methods were devised for aluminum, copper, mild and stainless steel.

By the use of these grids, moiré fringe patterns were photographed up to a maximum temperature of $1600^{\circ}F$.

CHAPTER II

THE PHOTO-OPTICAL SYSTEM

2.1 Introduction

The photo-optical system used to produce and record moiré
patterns, has the ability to perform as a linear low-pass filter of
spatial frequencies.

The system is composed of the lens and the film, both of which
have individually this ability. Thus, they operate together as two
linear filters in series.

The filtering effect can be thought of as the process by which
the higher spatial harmonics of the Fourier decomposition of the object
are unable to pass onto the recorded image. This has a degrading effect
on the image, since the infinite expansion that represents the object
in all its detail, is interrupted after a given finite number of terms.

Moreover, we will see that the effect of the system is to damp,
with progressive vigor as frequencies increase, the corresponding ampli-
tude coefficients of the Fourier expansion. This produces an increasing
loss of contrast as the spatial wavelengths get shorter.

In what follows, we will understand by system analysis the proc-
esses by which we record passively the action of a given system on the
moiré information.

We will call system synthesis the processes by which we act on
the system to change its frequency response characteristics to suit
our purposes.

6

where $C^i(\omega)$ and $C^o(\omega)$ are the contrast of the image and the object at frequency ω.

The MTF is then a measure of the relative degradation in amplitude of the image of a sinusoidal object.

Under incoherent illumination, a condition common in moiré work, the optical response of the lens and the film may be regarded as two linear operations in series. This requires, however, that the exposure level of the photograph be adjusted so that the entire amplitude of the sinusoidal input will lie within the straight line portion of the H & D characteristic curve of the film.

Under the above conditions of linearity, the MTF of the photo-optical system can be expressed as

$$M_o(\omega) = M_L(\omega) \cdot M_F(\omega) \tag{2.3}$$

where $M_o(\omega)$, $M_L(\omega)$ and $M_F(\omega)$ are the transfer functions of the photo-optical system, the lens and the film, in that order.

The MTF technique offers the following advantages for moiré work:

a) The test targets used in the method resemble exactly the actual objects, in fact, the sinusoidal test targets can be considered as perfect, noiseless, undistorted moiré fringes.

b) The performance of the system is evaluated over a large area in the object plane.

c) The MTF can not only be used to predict the response of the entire system, but can also be used to examine each element in the

photo-optical process to determine what degradation of the image is introduced at each stage.

d) The MTF of a system can be obtained from those of its component elements by simply multiplying the corresponding MTF curves, ordinate by ordinate, for each abscissa value.

e) The knowledge of the MTF curves of the system, as will be explained later, enables us to determine the largest maximum displacement that can be measured by the system.

f) For the critical work of reproduction of moiré line masters, the MTF offers again quantitative information regarding the contrast that can be expected between dark and clear lines in the copy.

g) Finally, the MTF curve adequately represents the optical-filtering capabilities of the system.

Notwithstanding the above, Hempenius [7] has found that photographic systems analysis based only on the MTF characteristics may be in some cases significantly in error and that the effect of grain should be taken into account. This is not believed to be the case in moiré fringe photography.

2.3 Modulation Transfer Function of Lenses

Camera lenses degrade the arriving light signal by aberration and by diffraction.

We will first consider the diffraction effects, assuming for this purpose that we possess an ideal aberration-free lens.

Between the spatial wavelengths large enough to be passed without attenuation of amplitude and the one that represents the limit of resolution, the MTF of an ideal lens varies as shown in Figure 1a.

We will now turn to the aberration losses, which depend on the lens construction. Photographic lenses must be made to operate at various aperture settings and the best any manufacturer can do is offer several different compromises between the various types and amounts of aberrations: distortion, astigmatism, curvature of the field, etc. However, the optimum chromatic correction available should be preferred for both moiré master and fringe photography.

Regarding the other aberration losses, unfortunately no recommendations of such a general nature can be given. Kelly [8] reports tests on a 50 mm f/2.8 photographic lens that show that geometrical aberrations are responsible for most degradation at f/2.8 while at f/8 most degradation is due to diffraction. Hence the aperture setting of the iris has an important effect on the MTF.

This situation obliges us to resort to actual testing of the lens we intend to use for a future optical filtering application. Modification to the curve of Figure 1a due to aberration must be determined experimentally for the magnification and aperture setting we intend to use if this information is not supplied by the lens manufacturer.

A test of this nature is described in Section 2.5 in detail.

2.4 Modulation Transfer Function of Films

The Modulation Transfer Function of a film decreases with increasing spatial frequency and resembles, in a general way, that of a lens. The damping of high frequency amplitude coefficients reflects the effect of the diffusion of light within the emulsion on the microstructure of the image.

However, all films do not possess the same limiting curve of maximum resolution as is the case with lenses. Films with a MTF approximately equal to one over a broad range of spatial frequencies are manufactured for spectroscopy and document reproduction.

The MTF for the Kodak Royal Ortho film used in the photo-optical test described in Section 2.5 can be seen in Figure 1b.

Complete information on the MTF of numerous photographic films and plates is available from the manufacturers [9].

2.5 Experimental Determination of the Modulation Transfer Function of the Photo-Optical System

Tests were conducted to determine the MTF of a 12 in., f/10, Alphax copying lens, and of this lens together with Kodak Royal Ortho film.

The lens and film were used later in the thermal test of Chapter IV. The magnification tested was one to one and the aperture setting was f/10.

Since the MTF will vary across the image plane of a photographic object, from its highest value near the optical axis to a lower value near the edges, test targets were placed in the center and at one edge of the object plane.

The test targets manufactured by the Eastman Kodak Company vary sinusoidally in transmittance, with harmonic distortion of less than 2%, and range in spatial frequency from 3/8 to 42 cycles per millimeter. The modulation of transmittance is approximately 65% for the target placed in the center of the field and 30% for the one placed at the edge.

The targets also possess a grey scale for calibration purposes. The
optimum performance of the lens was found to be restricted to a circle
with center at the optical axis and radius 0.16 the focal distance.

Since the focussing of the camera has a great influence on the
MTF the exact focus will provide the highest limit of resolution. For
every position other than the true focus the lens performs with a differ-
ent MTF. The further the image plane is removed from the focal plane,
the poorer the resolution becomes [10].

This immediately suggests a way of filtering out excessive low
frequency passed by the lens by slightly defocussing the optical system.

This also obliges us to perform the lens test for the same posi-
tion of the image plane with respect to the true focal plane as that
at which we will operate during the actual running of the moiré test.
This is not an easy matter since both tests may be performed at differ-
ent locations and with different optical equipment except for the lens
tested.

The recommended technique [11] of taking several photographs at
positions close to the true focus and selecting the optimum between them
is too lengthy for most experimental stress analysis applications where
the object may have to be moved several times during the test.

We have used, to select the optimum focussing in both the lens
and thermal tests, the visual inspection with the aid of a 60X micro-
scope of the image of 12 lines per millimeter produced on a finely
ground glass manufactured by us for this purpose.

To record the image we selected Kodak Royal Ortho film with an
ASA speed of 400 because of its known MTF, H & D characteristic, and

proven ability to record moiré patterns at elevated temperatures. Care was exercised to expose the sinusoidal test patterns entirely in the straight line portion of the sensitometric curve.

The MTF of the film is represented in Figure 1c. The MTF of the lens-film combination was obtained by scanning both the test object and the negative with a Joyce and Loebl microdensitometer. By scanning the grey scales of the target, a calibration curve can be obtained relating the densitometer reading to the corresponding density [6].

The scans of the sinusoidal patterns were then analysed to determine the average values of the maximum and minimum densities for a given frequency.

The modulation was then obtained by the use of the formulas [12]

$$\Delta D = \log T \min (\omega) - \log T \max (\omega) \tag{2.4}$$

$$C(\omega) = \frac{T \max (\omega) - T \min (\omega)}{T \max (\omega) + T \min (\omega)} \tag{2.5}$$

The plot of the modulation transfer function $M_o(\omega)$ corresponding to the lens-film combination that was obtained from the experiment can be seen in Figure 1d.

According to (2.3), if we have measured $M_o(\omega)$ and we are given $M_F(\omega)$, the MTF of the lens alone can be obtained. The results have been plotted in Figure 1e.

The product of the MTF of the ideal lens and the film differs considerably from the measured values of the combination. This is particularly so as the wavelengths get shorter. The vigor of this damping

is undoubtedly due to incorrect focussing and aberrations rather than
to the latter alone. This emphasizes the strong dependence of the
transfer characteristics of the lens on the correct focussing [10].

Figure 1f shows the results of testing the lens-film combina-
tion at one edge of the image plane. Comparison of Figure 1d with
Figure 1f shows how the system performs better for smaller angular
apertures. The damping of the very long wavelengths indicates loss of
focus by lack of parallelism of the image plane with respect to the
object plane.

2.6 Light Intensity Trace of Moiré Fringes

The light intensity variation along a line in a moiré pattern
given by

$$I(x) = I_o + I_1 \cos 2\pi \rho(x) \tag{2.6}$$

can be obtained from the photographic negative used to record the
pattern. A photo-reading device as the one presented in [4] can be
used to obtain the trace of the transmittance of the negative, or
a scanning microdensitometer can be employed to record the density varia-
tions of the film.

The incident exposure on the film can then be retrieved from the
transmittance or from the density trace by performing the operations

$$E_n(x) = I(x) \cdot t = T_n(x)^{-\frac{1}{\gamma n}} \tag{2.7}$$

or

$$E_n(x) = I(x) \cdot t = \left[\text{Log}^{-1} D_n(x) \right]^{\frac{1}{\gamma n}} \tag{2.8}$$

as the case may be.

It has been the custom in moiré work to regard the negative, obtained by photographing the fringes, as a suitable representation of the original exposure pattern. The clear fringes in the model appeared as dark fringes in the negative and vice versa, but no consequence was attached to this since the curve of displacements was plotted with respect to an arbitrary origin.

A look at the characteristic curve of a film shows immediately that the output of a film to incident exposure is transmittance or density of silver deposit. Furthermore, this relationship is non-linear and independent of the spatial frequency of the input. There-fore, what is recorded on film of an arriving spatial sinusoidal varia-tion of intensity is a harmonically distorted waveform of spatial den-sity or transmittance, Figure 2.

The amount of this distortion is illustrated in Figure 3 where exposure rather than the logarithm of the exposure has been plotted in the abscissas. In Figure 4 we show the strong distortion of an actual transmittance trace of a sinusoidal light intensity variation corre-sponding to a moiré pattern of fringes.

Since the application of the continuous light intensity dis-placement law makes use of the light intensity of all portions of the spatial waveform, the undistorted reproduction of the signal is manda-tory and Equations (2.7) or (2.8) should be applied always.

It will be seen in Section 2.7 that it is possible to perform photographically these operations.

It is interesting to note that there is no space shift of the maximums and minimums of the intensity curve with respect to those of

the transmittance curve. Therefore, the usual method of hand analysis, that only takes these points into account for the plot of the displacement curve, will be free of the errors due to photographic reproduction discussed here.

The continuous trace of incident exposure will contain, in addition to the phase modulated spatial curve containing the information on the displacement in the body given by (2.6), spurious amplitude and phase variations due to noise. These disturbances are visible in Figure 4.

We wish to extract (2.6) from the noise in which it is submerged before proceeding with the determination of displacements to increase the accuracy of the procedure.

The amplitude variations are caused by the non-uniform illumination of the object, by changes in the reflectance of the model surface, and by the progressive vigor with which the amplitude coefficients of the Fourier decomposition of the image are damped by the filtering action of the photo-optical system.

The more frequent causes of short wavelength variations are the image of the master and model grid lines on the moiré fringe, the scratches and pits in the model surface, and the dust that can settle over the model during testing. The long wavelength variations, on the other hand, are often due to non-uniform illumination and surface reflectance or transmission.

Since these perturbations in the trace are of both longer and shorter wavelengths than those of the useful signal, a band-pass filter is necessary to eliminate them.

Optical band-pass filters cannot be easily synthesized; however, the photo-optical system used to produce and record the moiré fringes has inherent low-pass filter capabilities of which we can take advantage. This will allow us to implement, optically at least, one part of our filter requirements.

Both long wavelength and amplitude perturbations may be removed by other than optical means, and, to do this, digital in-quadrature filters have been used successfully as will be seen in Chapter III.

It remains for us to develop in this chapter the techniques to photographically correct the wave distortion due to the non-linear film response and to substantially reduce optically the noise content of the moiré fringe light intensity trace.

2.7 Correction of Spatial Waveform Distortion

The so-called straight line portion of the characteristic curve of the film is a linear relationship between the density and the logarithm of the exposure. The logarithm of a sinusoidal exposure variation is shown in Figure 5.

Therefore, a sinusoidal exposure within the straight line portion of the sensitometric curve will produce a spatial density variation linearly proportional to the logarithm of the arriving sinusoidal spatial waveform. However, if the exposure cannot be kept entirely within this straight section of the sensitometric curve and the toe of this curve is used to record the arriving signal, further distortions are produced as shown in Figure 6.

If we wish to eliminate photographically the spatial harmonic distortion due to the non-linear response of the negative film, the following two processes have been proven effective.

a) Negative-positive film combination

A combination of negative and positive films can be chosen such that the products of their gamma coefficients is equal to one [13].

For the straight line portion of the characteristic curve of the negative, the following holds

$$D_n = \nu_n \log E_n + C_1 \qquad (2.9)$$

where D_n is the density of the developed film, E_n is the exposure, γ_n the slope of the sensitometric curve which in general will be positive and larger than one, and C_1 is a constant. The subscript n refers to the negative.

The transmission of the negative is given by

$$T_n = C_2 E_n^{-\nu_n} \qquad (2.10)$$

where C_2 is a constant. If we print this negative on a positive film with a ν_p such that

$$\nu_n \nu_p = 1 \qquad (2.11)$$

we obtain

$$T_p = C_2 E_n e^{\gamma_n \gamma_p} = C_2 E_n \qquad (2.12)$$

where T_p is the transmission of the positive and C_2 is a constant. Thus a film linearly proportional in transmission to the exposure of the object has been obtained.

This process cannot always be applied in moiré work because of the diversity of films that are used as negatives depending on the applications and the very few pairs of films whose product of gammas is equal to one.

In the thermal test reported in Chapter IV, for example, six different films were used to record the fringe patterns, since variations in the ASA speed became necessary as temperatures increased.

Since the value of γ depends on the developing time, some suitable pairs of films can be obtained if the stringent requirements on processing can be enforced.

b) Non-linear density wedge method

In this method we make use of a microdensitometer as the Mark III C manufactured by Joyce Loebl and Company of Gatehead, England. This machine measures density on the negative by balancing it with a known density located on a linear density wedge.

The principle of operation is based on a true double-beam light system in which two beams from a single light source are switched alternately to a single photo-multiplier.

One beam of light is passed through a point on the film, the other through a calibrated reference wedge of linear density variation. If the two beams arriving at the photo-amplifier are of different intensity, a servo motor is activated that causes an optical attenuator to reduce this difference to zero. In this way a continuously null balancing system is obtained in which the position of the optical alternator is made to record the density at any point of the specimen.

Under the above mentioned conditions the machine will perform linear density measurements. However, since we are interested in retrieving the exposure sinusoidal variation, the density wedge of the machine can be modified to achieve this.

Figure 7 shows the density trace of a sinusoidal exposure, the sensitometric characteristic curves of the linear wedge and of a non-linear wedge with the corresponding output functions.

The linear wedge produces a true density measurement at each point which results in a distorted exposure curve. The non-linear wedge will produce an output identical to the exposure input, if the sensito-metric curves of the film and wedge are identical.

To accomplish this practically, we have printed on the type of film being used as a negative, the appropriate linear density wedge. The developing process was identical for both the negative and the non-linear wedge so the resulting γ coefficient of both sensitometric curves was the same. The results obtained by this method are shown in Figure 8.

The linear wedges photographed on film were placed between two glass plates held together with Canada Balsm. The resulting non-linear wedges were placed in the travelling carriage of the microdensitometer, which then performed linear measurements of exposure for this particular film.

The advantage of this procedure over the negative-positive film combination is that the appropriate non-linear wedge characteristic curve can always be obtained for any negative. Both share the dis-advantage of requiring strict film processing control.

2.8 Filtering of a Moiré Signal

Several successful optical filtering operations have been
reported in the communication sciences and optical literature [14, 15,
16], however, moiré work has not previously benefitted from these use-
ful techniques.

We will describe in what follows several experiments in which
the quality of moiré fringes has been substantially increased by
optical filtering.

As we said in Section 2.6, an optical filter of the low-pass
type can be readily implemented, in fact, the tests reported in Sec-
tion 2.5 indicate that a perfect lens has high frequency filtering
ability. However, the cut-off frequency of a real lens-film combina-
tion may not be sufficiently short to eliminate the undesirable disturb-
ances of the light intensity trace of the moiré fringes. Therefore,
additional modifications of the transfer characteristics of the optical
system are necessary.

The purpose of this section is to establish the practical means
of achieving these modifications in moiré work. It will be seen that
strong disturbances are not always completely eliminated optically but
that the noise level is substantially reduced in all cases.

We should keep in mind during this discussion the structure of
the image of a moiré fringe shown in Figure 9a. The phase variations of
the average light intensity trace indicated in this figure carry the
information regarding the displacements in the body. Our purpose is to
obtain this average by optically erasing the image of the individual
grid lines and the random high frequency variations due to other sources

of noise. Failure to do this will result in an intolerable amount of noise in the analog voltage output of our photo-reader that is to be automatically processed to yield the displacements and strains.

It is necessary to distinguish in our treatment between the coherent and incoherent illumination over the object plane. In practice, conditions of illumination are such that some degree of coherence is always present, but, for simplicity, only the extreme cases mentioned above will be assumed here to exist.

a) Coherent illumination

Coherent light waves add in amplitude and linear relations hold between the amplitudes at different points in the system. Furthermore, these systems possess the property that a Fourier transform relation exists between the front and rear focal plane of a lens.

Under these conditions the amplitude distribution A_o over the output or image plane is given by Figure 10a.

$$A_o(x_3,y_3) = \iint_{-\infty}^{\infty} A_{in}(x_1,y_1) h_A(x_3-x_1,\ y_3-y_1) dx_1\ dy_1 \qquad (2.13)$$

where A_{in} is the amplitude distribution over the input or object plane and h_A is the amplitude response to a point source. In the spatial frequency domain the above equation is equivalent to

$$\overline{A}_o(\omega_x,\omega_y) = \overline{H}_A(\omega_x,\omega_y)\ \overline{A}_{in}(\omega_x,\omega_y) \qquad (2.14)$$

where $\overline{A}_o, \overline{H}_A, \overline{A}_{in}$ are the Fourier transforms of A_o, H_A and A_{in}, respectively.

H_A is therefore the amplitude transfer function of the optical system that operates on the object amplitude spectrum to give the image amplitude spectrum.

Due to the Fourier transform relation that holds between the front and rear focal plane of a lens, Figure 10a, the function H_A is displayed at P_2, thus affording a means of controlling the Fourier components that make up the image by inserting an appropriate mask in this plane.

The mask can in general be a complex transmittance $M = |M|e^{i\varphi}$, thus affording control over the amplitude by varying the optical density of the mask and over the phase by varying the thickness. One such complex filter function has been implemented recently by Vander Lugt [17].

In dynamic and high temperature moiré investigations it is often necessary to produce a fringe pattern between the image of the model's grid and a master grid placed in the back of a photographic camera. The moiré pattern thus recorded on film contains not only the image of the fringes but also the contact copy of the line master. These lines produce an undesired high frequency disturbance in the light intensity trace of the fringes, Figure 9b.

When the master is in the object plane, a well-focused photographic camera will also record the image of the individual lines together with the moiré fringes, if the aperture is not sufficiently reduced to perform a type of filtering that will be discussed in (b). In this case again, the images of the grating lines are a source of noise, Figure 9a.

To remove this disturbance, the negative of the moiré pattern was inserted in plane P_1 of Figure 10a. The spectrum of the image of the grating lines was displayed at P_2 and a completely opaque mask wide enough to interrupt the central order of the Fourier decomposition was placed at P_2. The remaining orders were collected by the lens L_3 to produce an image almost completely free of the grating lines at P_3.

A 50X magnification of the appearance of the microstructure of the image before the bias removal is shown in the upper insert of Figure 11, while the lower insert corresponds to a 50X magnification after filtering.

The strong damping is due to the fact that the film, as the eye, is unable to register negative intensities and records only a pattern proportional to the square of the amplitude of the arriving disturbance.

b) Incoherent illumination

Incoherent light waves add in intensity and linear relations hold between the intensities at different points in the system.

The intensity distribution over the image or output plane $I_o(x_2, y_2)$ is given by Figure 10c.

$$I_o(x_2, y_2) = \int\!\!\int_{-\infty}^{\infty} I_{in}(x_1, y_1) h_I(x_2 - x_1, \, y_2 - y_1) \, dx_1 dy_1 \qquad (2.15)$$

where $I_{in}(x_1, y_1)$ is the intensity distribution over the object or input plane and h_I is the intensity response to a point source. In the spatial frequency domain the above equation is equivalent to

$$\overline{I}_o(\omega_x, \omega_y) = \overline{I}_{in}(\omega_x, \omega_y) \overline{H}_I(\omega_x, \omega_y) \qquad (2.16)$$

where $\bar{I}_o$, $\bar{I}_{in}$, $\bar{H}_I$ are the Fourier transforms of I_o, I_{in} and H_I, respectively.

H_I is then the intensity transfer function that operates on the object intensity spectrum to yield the image intensity spectrum.

It can be shown [18] that

$$H_I(\omega_x, \omega_y) = \left(\frac{C_o}{K}\right)^2 \int\int_{-\infty}^{\infty} f^*(\alpha, \beta) \, f\left(\alpha - \frac{\omega_x}{K}, \ \beta - \frac{\omega_y}{K}\right) d\alpha \, d\beta \qquad (2.17)$$

where $f(\alpha, \beta)$ is the complex amplitude distribution over the surface of the aperture and $f^*(\alpha, \beta)$ its complex conjugate. The angular coordinates α and β are shown in Figure 10b. C_o is a constant and $K = 2\pi/\lambda$, where λ is the wavelength of the radiation.

Therefore, control over the amplitude and phase of $f(\alpha, \beta)$ affords a means of achieving various filtering effects.

For a perfect lens $f(\alpha, \beta)$ is real and equal to one over the entire aperture and zero elsewhere. The application of (2.10) to a perfect lens results in the curve of Figure 1a and indicates that a perfect lens is limited in resolution by its aperture. The limit of resolution being equal to d/λ. This immediately suggests a simple way of damping the high frequencies present in the object by reducing the size of the iris of the optical instrument.

Application of this filter effect to moiré fringes produced the results shown in Figure 12 where the microdensitometer traces of two fringes corresponding to the same traction test are presented. The master grid was in the object plane when the photograph was taken. The upper fringe corresponds to an aperture setting of f/10 and the

lower to an aperture of f/64. The damping of the 300 line per inch of the master is clearly visible.

This method is not always practical in moiré work because exposure times become very long for the small apertures necessary to filter out coarse grids at one to one magnification. However, since smaller apertures will always filter some high frequency noise, though not perhaps the grid lines, they should be used whenever possible.

We next will take advantage of the strong influence of defocussing on the transfer function of a lens which was already evident in the tests of Section 2.5.

When we move the image plane from the focal plane we leave the Frauenhofer diffraction region and enter the Fresnel zone where the diffraction pattern at the output plane will no longer be the Fourier transform of the aperture. However, Cheatham and Kohlenberg [18], using the approximations of geometrical optics, obtain as the unit intensity response of the defocussed system

$$h(x,y) = h(r) = \begin{cases} \left(\dfrac{I}{a}\left|\dfrac{v}{u}\right|\right)^2 & \text{for} \quad r \le \dfrac{|a|}{v} \\ \\ 0 & \text{for} \quad r > \dfrac{|a|}{v} \end{cases} \tag{2.18}$$

where I is the intensity of the point source per solid angle, u the object distance, v the image distance and a the defocal length. Since

$$H(\omega_x, \omega_y) = \int\!\!\int_{-\infty}^{\infty} h(x,y) e^{-i(\omega_{xx} + \omega_{yy})} dx\; dy \tag{2.19}$$

then

$$H(\omega r) = 2\pi \ I\left(\frac{L}{u}\right)^2 \ \frac{J_1\left(\frac{aL\omega r}{v}\right)}{\frac{aL\omega r}{v}} \qquad (2.20)$$

where

$$r = \sqrt{x^2 + y^2} \ , \qquad \omega r = \sqrt{\omega_x^2 + \omega_y^2}$$

According to (2.13) an increase in the defocal distance will close the low-pass filter characteristic of the system. The practical significance of this fact can be seen in Figure 13 where the micro-densitometer traces corresponding to the same fringe of a traction test has been photographed at different focal settings. The upper fringe of the picture was taken at the correct focus, the lower with the image plane removed $a = 0.0625$ in. from the focal plane of the lens.

Further experimentation was conducted to increase the quality of the image of periodic line patterns, whether they were moiré fringes or grid lines, under incoherent illumination and submerged in strong random noise.

In this connection there exists an extensive literature in the field of optics dealing with the calculation of the intensity transfer function $H_I(\omega_x, \omega_y)$ of a lens when aberrations are present. Steel [19] and O'Neill[20] have calculated such functions for an annular aperture and Françon [21] reports work done by Sayanagui on a circular aperture covered by small randomly distributed transparent elements.

The family of modulation transfer functions obtained by the first two authors, for different ratios of interior to exterior diameter

of the annulus, show how the transfer characteristics of a lens can be modified to obtain essentially different filtering effects.

As the ratio of the diameters approaches one, the transfer function develops narrow peaks in the vicinity of $\omega = 0$ and $\omega = 2\beta_o$, where $\beta_o = kd/2r$, $k = 2\pi/\lambda$ and d is the diameter of the aperture.

Since this effect would be useful to eliminate random noise from a periodic line pattern which had a spatial frequency equal to $2\beta_o$, experiments were conducted with annular apertures of the type described above. However, the loss of illumination for ratios of internal to external diameter approaching unity was so severe that photography of the filtered pattern became impossible.

Turning now to the work done by Sayanagui, this investigator produced the random dots of vacuum deposition on a flat piece of glass with parallel faces which he then placed before the lens. By this means he produced a filter that could eliminate in the image plane P_1 of an incoherent light system, Figure 10c, almost all traces of the screen mesh of a half-tone photograph introduced in the plane P_i.

Since we did not have at our disposal the elements to implement exactly Sayanagui's experiment, we introduced in the air space of an apochromatic photographic lens a Dirak "comb" consisting of an array of dark and clear parallel lines and provided the means of rotating this set of lines with respect to the optical axis of the instrument.

Samples of photographic noise were manufactured by exposing Kodak Kodalith film through a paper hand towel in an ordinary photographic contact printer. This artificial noise appeared to be of

a conveniently random nature and could be produced in several densities by varying the exposure time.

A periodic line pattern was superimposed with the noise to form the object and was focussed on the image plane of a lens containing the filter described above. The object and image obtained by this procedure are shown in Figure 14.

The density of lines tested as filters were 50, 100 and 300 lines per inch. A set of two arrays independently rotatable was also used.

The effect of each filter was to make the lens strongly aberrant astigmatically. Astigmatism was maximum in the direction perpendicular to the filter lines and zero in the parallel direction.

A single filter with 300 lines per inch produced the results shown in Figure 14.

The good results obtained by this method led us to a careful search of the available literature on the subject of apodization techniques for an analytical explanation of the observed phenomenon but none seems to have been published to date. We believe that the computational complexities of such a theoretical development fall beyond the scope of this research.

A final method of filtering high spatial frequencies of the image is by averaging the light intensity transmitted through the negative of a fringe pattern in a photo-reading machine. If the scanning slit of the instrument is made large enough, the contribution of the individual lines to the overall intensity is diminished significantly.

We have found that to eliminate completely the influence of the master grid on the photo-reading machine trace of a fringe produced

with the master in the image plane a slit at least ten times the size of the individual lines must be used.

For fringes produced with the master in the object plane, slits three times wider than the lines significantly reduced their influence on the trace. Figure 15 shows a microdensitometric graph of the same fringe scanned with a slit opening of 0.084 mm for the top trace and 0.27 mm for the bottom one.

It is interesting to note how all filtered fringes, while having damped the image of the grid lines, still reproduce faithfully all variations of the average light intensity. This average is precisely what carries the information pertaining to the displacement.

CHAPTER III

NUMERICAL METHODS FOR THE PROCESSING
OF MOIRÉ DATA

3.1 Introduction

Having produced and recorded a moiré fringe pattern with the
photo-optical instrumentation analysed in Chapter II, it remains for us
to obtain the displacements and strains from the continuous light inten-
sity trace of the fringes.

This trace, as we said earlier, contains the useful signal given
by (2.6) plus the spurious variations of amplitude and phase due to
noise.

We will call the intensity trace function before filtering $I^*(x)$
so that

$$I^*(x) = I(x) + N(x) \tag{3.1}$$

where $N(x)$ is the amplitude and phase noise contained in the signal.

This noise content will depend on the amount of optical filter-
ing performed on the pattern, however, for the purpose of this chapter,
no previous filtering will be assumed to have been made.

We are faced then with the necessity of implementing a numerical
band-pass filter to eliminate the unwanted disturbances of the moiré
light intensity trace given by (2.6).

Once this has been achieved, we desire to obtain the displace-
ments given by (1.1) along the direction normal to the master grid lines.

The digitalized version of $I^*(x)$ can be obtained by the modification of a scanning microdensitometer as the Joyce & Loebl Mark III C shown in Figure 16.

If this instrument is provided with a potentiometer arrangement that will yield analog voltages proportional to both the density measured on the pattern and to the coordinate position, these voltages can then be digitalized on a voltmeter and the numerals printed on tape for convenient handling in a high speed computer.

The system, consisting of a microdensitometer and a digital voltmeter, used in the present investigation is shown in Figure 17.

The principle of operation of the microdensitometer was explained in Section 2.7. It is capable of performing linear density measurements from 0 D to 6 D, and of linear magnification from 1 X to 1000 X.

The digital data acquisition system is a Dymec 1020 B, that, at the sampling rate of ten words per minute, has a maximum resolution of 0.0001 V.

With this system, care must be taken in moiré work to use either a non-linear density wedge in the microdensitometer, as was described in Section 2.7, or to include operations (2.7) and (2.8) in the digital program that will handle the numerical operations. Failure to do this will cause the non-linear response of the photographic film, used to record the fringe pattern, to produce undesirable waveform distortion.

The nature of the spurious disturbances in the moiré light intensity trace has been discussed in Section 2.6. In order to eliminate these by digital means, a successful band-pass filter must be implemented numerically.

In previous work [6] an in-phase band-pass electronic filter was used to eliminate spurious variations in the amplitude and phase of the analog output of the photo-reading machine. The inclusion of the electronic filter produced transients of long decay time that lengthened considerably the operating time necessary to process the fringe patterns.

To overcome this difficulty, numerical in-phase and in-quadrature filters were combined in this investigation to separate the amplitude and phase of the light intensity trace and to yield the phase information contained in the signal with minimum error.

The details of these digital filters will be presented in Section 3.3.

Upon obtaining the digitalized and filtered version of our displacement curve (1.1), we still need to implement the process of derivation by which strains are obtained from displacements.

The definition of the derivative, as the limit of a difference quotient, has little value if we possess only a discreet number of experimentally determined values of the function.

The ratio $\Delta y/\Delta x$ becomes excessively sensitive to small errors in the value of y as Δx becomes small [22]. Therefore, we must resort to a least square approximation for a set of values of the function in the neighborhood of the point where we wish to obtain the derivative.

The influence of varying the degree of the polynomial approximation, and the use of these techniques of numerical calculus for the computation of strains, will be seen in Section 3.4.

If the displacement curve is obtained by the use of numerical in-phase and in-quadrature filters the process of derivation can be implemented in an analog electronic circuit. The details of this approach will be presented in Section 3.5.

To evaluate the merit of the different procedures utilized to retrieve the phase information and to derive the curve of displacements, two auxiliary tests were performed. These consisted of a bar under traction and a disk under compression. A brief report on the pertinent features of these tests is given in Section 3.2 and the comparative performance of the different methods is discussed in Section 3.6.

3.2 Auxiliary Tests

A bar under axial tension and a disk under diametral compression were used as auxiliary tests to evaluate the effectiveness of the numerical techniques that will be described in this chapter. Both samples were made of Hysol 8705 and engraved with a grid of 300 lines per inch.

By means of the tension test a series of parallel equidistant moiré fringes were produced that corresponded to the state of homogeneous deformation in the body. The ideal, noiseless, undistorted moiré fringes would therefore give rise to a pure cosine curve of constant amplitude and frequency as their light intensity trace. Our real trace, after filtering, should approximate closely the ideal.

The displacement curve along any line parallel to the longitudinal axis of the sample should be a line of constant slope proportional to the strain in the body.

For control purposes the average strain in the body was calcu-
lated over a distance of 7 in. along the longitudinal axis of the
sample.

A strain of 34.854×10^{-4} in./in. was determined. The combined
relative errors of the microdensitometer location of the first and last
fringe and of the hand plot of linear distances was 0.7%.

Turning now to the moiré test of the same traction sample, the
pattern was processed in the system of Figure 17. The sampling rate
was ten words per second. The taped output of the digital voltmeter
was translated to a punched card format compatible with an IBM 709
computer.

The deck of data cards was then processed by the numerical and
analog methods described in Sections 3.3, 3.4 and 3.5 to produce the
results discussed in Section 3.6.

In a second moiré test a disk 4 in. in diameter was loaded
diametrically, Figure 18, and the fringe pattern was secured by the
system of Figure 17. The density trace of the moiré fringes across the
horizontal axis of the disk is shown in Figure 18.

In this case a strong frequency modulation exists in the light
intensity variation, therefore, a more general state of deformation
than the one existing in the traction sample is obtained.

The pattern was processed along the x-axis in a manner entirely
similar to that described for the traction sample.

The theoretical solution to the disk problem is well known [23]
and it affords additional means of evaluating the accuracy of the numer-
ical techniques proposed here. The large deformations imposed here

cause linear theory and the experiment to disagree somewhat due to the relatively large deformations of the boundaries [24, 25].

However, since it was of great interest to us to determine if the numerical procedures employed could retrieve the form of the displacement and strain curve from the noise in which they were immersed, this test was considered suitable.

The density trace of the fringes along the y-axis of the disk is shown in Figure 19. Under uniform illumination the amplitude of the trace is seen to diminish as the spatial wavelengths become shorter in the neighborhood of the applied load.

Though the light intensity trace in this direction was not processed to yield the strains, it is shown here as another good example of the spatial filtering characteristics of the photo-optical system discussed in Chapter II.

It is clear that when the displacements along the direction normal to the master grid become large enough to cause the distance between fringes to approximate the limit of resolution of the optical system, the contrast in the recorded fringe pattern will be drastically reduced.

In the event that this occurs, initial mismatches of contrary sign to the displacement expected in a given region would increase the final spatial wavelength of the moiré fringes and permit better analysis.

3.3 Displacement Determination by In-Phase and In-Quadrature Filters

Having obtained, by the use of the electro-optical system, the digitalized version of the moiré light intensity trace of the fringes plus noise, we possess the numerical values of an empirical function. We will call this set of numbers I_k^* and the continuous function from which they were obtained $I^*(x)$.

We make the following assumptions regarding $I^*(x)$:

    a) It is a function that defines a generalized function

    b) It is band limited

    c) The spectrum of the desired signal $I(x)$ and that of the noise $N(x)$ are disjoint.

The first assumption holds in all cases. The other two must be taken as only partially representative of the physical facts.

Assumption (a) is satisfied by all light intensity variations of moiré fringes. In fact, $I^*(x)$ satisfied Dirichlet's conditions on its interval of definition, which is the length of the model in the direction of scanning.

Regarding (b) the moiré light intensity trace plus noise has in general a broad band representation in the frequency plane. The harmonic content, however, can always be cut short of infinity without significant loss of information contained in the signal.

Assumption (c) may or may not hold exactly depending on the noise characteristic of the signal. If it does not hold, the analysis that follows will be only approximately valid, but sufficiently accurate for all cases encountered by the writer.

If assumption (c) holds, the frequency composition of the function to be filtered is contained in a frequency interval $f_o \pm \Delta f/2$, where Δf is the band width and f_o the center frequency. All frequencies, of course, are spatial in moiré work.

If we select a sampling frequency f_s in our electro-optical device such that $f_s = 2f_a$, where f_a is the highest frequency present in the data, under assumptions (a) and (b) Shannon's sampling theorem permits us to write

$$\tilde{I}_k^* = \sum_{p=-m}^{m} a_p^* I_{k+p}^* \qquad (3.2)$$

where $\tilde{I}_k^*$ indicates a good approximation of $I^*(x)$ obtained through (3.2).

However, if the coefficients a_p^* are the inverse Fourier transforms of a particular transfer function in the frequency domain, $\tilde{I}_k^*$ given by (3.2) will be a filtered version of $I^*(x)$. We will call the coefficients obtained in this manner a_p and for the resulting filtered version of $\tilde{I}_k^*$ we will reserve the notation $\tilde{I}_k$, thus,

$$\tilde{I}_k = \sum_{p=-m}^{m} a_p I_{k+p}^* \qquad (3.3)$$

The factors a_p become, in this case, spatial invariants that play the role of weight functions of a linear filter. Equation (3.3) can be thought of as a finite moving average process.

The basic relations of linear filter theory are given in Appendix A for convenience of the reader.

Since the information on the displacement field is contained in the phase of the signal $I(x)$, we wish to develop a numerical procedure

capable of separating the phase variations from the amplitude changes
of a signal arriving at a filter.

A simple way of accomplishing this was mentioned by Gabor [26]
and is applied to our problem in what follows.

Let us assume for simplicity that the light intensity trace of
a moiré pattern is a real signal of the form

$$I(x) = a \cos \omega x + b \sin \omega x \tag{3.4}$$

This real signal can be replaced by a complex signal of the
form

$$\Phi(x) = I(x) + i\, I_q(x) \tag{3.5}$$

where $I_q(x)$ is defined as

$$I_q(x) = a \sin \omega x - b \cos \omega x \tag{3.6}$$

hence

$$\Phi(x) = (a - ib)e^{i\omega x} \tag{3.7}$$

and then

$$I(x) = \mathrm{Re}\ \Phi(x) = [I(x)^2 + I_q(x)^2]^{\frac{1}{2}} \cdot e^{i\,\tan^{-1}\frac{I_q(x)}{I(x)}} \tag{3.8}$$

The function $I_q(x)$ is a signal in quadrature with $I(x)$ that
transforms the oscillating vector into a rotating vector.

If $I(x)$ is not a simple harmonic the in-quadrature function is
provided by the Hilbert transform of $I(x)$.

The square brackets in (3.8) represent the amplitude of $I(x)$
while the phase of $I(x)$ is given by

$$\rho(x) = \tan^{-1}\frac{I_q(x)}{I(x)} \tag{3.9}$$

and the amplitude and phase information contained in $I(x)$ has been separated to suit our purpose.

This transformation of an oscillating vector function in a rotating vector function has been widely used in the analysis of narrow-band wave forms [27, 28, 29]. The combination of this transformation with numerical filtering has been used by Ormsby [30] and by Goodman [31].

We will refer in what follows to $I(x)$ as the in-phase signal while $I_q(x)$ will be called the in-quadrature signal. The latter is obtained from the former by a $\pi/2$ phase shift.

Since our analysis involves digital computation with a signal submerged in noise, we will be working with the sampled version of $I^*(x)$ and $I_q^*(x)$ which we have called I_k^* and $(I_q^*)_k$.

The purpose of our numerical procedure will be to

a) obtain the filtered version of I_k^* which we call $\tilde{I}_k$,

b) produce the 90 degrees out of phase and filtered $(\tilde{I}_q)_k$ by the expression

$$(\tilde{I}_q)_k = \sum_{p=-m}^{m} b_p \, I_{k+p}^* \qquad (3.10)$$

where the b_p have the same interpretation as the a_p in (3.3), and are derived from them according to (3.4), and (3.6),

c) find the quotient of $(\tilde{I}_q)_k$ and $\tilde{I}_k$ and introduce it in

$$o(x) = \tan^{-1} \frac{(\tilde{I}_q)_k}{\tilde{I}_k}, \qquad (3.11)$$

d) obtain the displacements given by

$$U(x) = po(x), \text{ and} \qquad\qquad (3.12)$$

e) derive this displacement curve to produce the strains.

We will apply, to fulfill objectives (a), (b) and (c), the techniques proposed by Ormsby and Goodman, and upon obtaining a smooth curve of phases, the change of scale implicit in (3.12) will yield the displacements.

The process of derivation (e) will be considered in Section 3.4.

(1) Goodman's linear combination of Tukey filters.

The ideal transfer function of an in-phase and in-quadrature filter is shown in Figure 20.

Goodman [31] proposed a linear combination of Tukey filters that is centered at f_o, is essentially flat from $f_o - \pi/m$ to $f_o + \pi/m$, and zero outside the interval $f_o - 3\pi/m$ to $f_o + 3\pi/m$. The coefficient m is the number of terms in the trigonometric series of the Tukey filter transfer function.

The filter function that results from the linear combination is shown schematically in Figure 21.

The filtering finite moving in-phase and in-quadrature average processes in the space domain are given by

$$\tilde{I}_k = \left[\frac{4}{m} + \frac{8}{\pi} \sum_{j=1}^{m-1} \frac{(0.54 + 0.46 \cos j \frac{\pi}{m}) \sin j \frac{\pi}{m} \cos j \frac{\pi}{m} \cos^2 j f_o}{j} \right]^{-1}.$$

$$\{ \frac{4}{m} I_k + \frac{8}{m} \sum_{j=1}^{m-1} (0.54 + 0.46 \cos j \frac{\pi}{m}) \cos j \frac{\pi}{m} \cos j f_o (I_{k+j} + I_{k-j})$$

$$+ \frac{4}{m} (0.54 + 0.46 \cos \pi) \cos \pi \cos m f_o (I_{k+m} + I_{k-m}) \}$$

$$(3.13)$$

$$(\tilde{I}_q)_k = \left[\frac{4}{\pi} \sum_{j=1}^{m-1} \frac{(0.54 + 0.46 \cos j \frac{\pi}{m}) \sin 2j \frac{\pi}{m} \sin^2 j\, f_o}{j} \right]^{-1} \cdot$$

$$\left\{ \frac{8}{m} \sum_{j=1}^{m-1} (0.54 + 0.46 \cos j \frac{\pi}{m}) \cos j \frac{\pi}{m} \sin j\, f_o (I_{k+j} + I_{k-j}) \right.$$

$$\left. + \frac{4}{m} (0.54 + 0.46 \cos \pi) \cos \pi \sin m\, f_o (I_{k+m} + I_{k-m}) \right\}.$$

$$(3.14)$$

The values of the filter transfer function in the interval $|f_o + \pi/m|$ to $|f_o - \pi/m|$ is called the filter roll-off. For Goodman's filter the roff-off is a straight line inclined with respect to the vertical axis. In this interval the real and ideal filter differ appreciably. The real filter allows noise of frequency close to that of the signal to pass onto the output.

Real filters vary as to the monotonic function that is selected to connect the horizontal portion of the transfer function with the frequency axis [32]. Tukey, as we said above, selected a straight line.

This produces a sharp discontinuity of the filter function at $f_o \pm 3\pi/m$ which in turn causes any series approximation used to express analytically the function to overshoot the value one, due to Gibbs' effect, at the discontinuity.

Another undesirable feature of this filter transfer function is the dependence of the band width Δf, the roll-off frequency interval, and the number of terms in the finite moving average process on a single parameter m.

The selection of one coefficient to suit these three different purposes restricts the applicability of this particular filter to problems where the signal has a narrow-band frequency composition and the noise and signal spectrum are disjoint.

The only other independent parameter of the filter is the central frequency f_o.

The practical implications of the comments made above will be explored further in Section 3.5 where comparative quantitative results are presented.

(2) Ormsby's filter.

A schematic representation of an Ormsby band-pass filter transfer function is shown in Figure 22.

The roff-off function of this filter is composed of two parabolic shoulders at f_c and f_t connected by a straight line. The length of the interval of definition of the parabolic transition can be modified by varying the value of the parameter k.

The independent parameters of the filter are the number of terms in the trigonometric series approximation of the transfer function N, the center frequency f_o, the cut-off frequency f_c, the largest frequency f_t, and the value of k explained above which is subject to the condition

$$k \leq \frac{f_t - f_c}{2} \qquad (3.15)$$

The parabolic transition increases the rate of convergence of the trigonometric series to the transfer function in the neighborhood of f_c, thus permitting better filtering of noise close to the

signal spectrum. The independence of f_t and f_c insures a narrow roll-off frequency interval.

The transfer function of this filter is

$$
H(f) = \begin{cases}
0 & \text{if } |f_{t_1}| \geq |f| \geq |f_t| \\[2mm]
1 & \text{if } |f_{c_1}| \leq |f| \leq |f_c| \\[2mm]
1 - a(f - f_c)^2 & \text{if } |f_c| < |f| < |f_c + k\Delta f_1| \\[2mm]
1 - a(f - f_{c_1})^2 & \text{if } |f_{c_1} + k\Delta f_1| < |f| < |f_{c_1}| \\[2mm]
bf + c & \text{if } |f_c + k\Delta f_1| < |f| < |f_t - k\Delta f_1| \\[2mm]
bf + c & \text{if } |f_{t_1} + k\Delta f_1| < |f| < |f_{c_1} - k\Delta f_1| \\[2mm]
a(f - f_t) & \text{if } |f_t - k\Delta f_1| \leq |f| < |f_t| \\[2mm]
a(f - f_{t_1}) & \text{if } |f_{t_1}| < |f| \leq |f_{t_1} + k\Delta f_1|
\end{cases}
\tag{3.16}
$$

where the parameters a, b, and c are solved in terms of k to satisfy the condition (3.16).

For the above transfer function the in-phase and in-quadrature finite moving average processes that yield the filtered versions of $\tilde{I}_m$ and $(\tilde{I}_q)_m$ can be found to be

$$
\tilde{I}_m = \sum_{n=-N}^{N} h_n \cos 2\pi n \lambda_o I^*_{n+m}
\tag{3.17}
$$

$$
(\tilde{I}_m)_q = \sum_{n=-N}^{N} h_n \sin 2\pi n \lambda_o I^*_{n+m}
\tag{3.18}
$$

where

$$h_n = \frac{\sin 2\pi n[\lambda_c + (1-k)\lambda_r] + \sin 2\pi n(\lambda_c + k\lambda_r) - \sin 2\pi n(\lambda_c + \lambda_r) - \sin 2\pi n \lambda_c}{4k(1-k)\lambda_r^2(\pi n)^3}$$

$$(3.19)$$

and

$$\lambda_o = \frac{f_o}{f_s}, \qquad \lambda_t = \frac{f_t}{f_s}, \qquad \lambda_c = \frac{f_c}{f_s}, \qquad \lambda_r = \lambda_t - \lambda_c \qquad (3.20)$$

The filters (3.13), (3.14), (3.17) and (3.18) were implemented in an IBM 709 programming code. By several trial runs with different. value of the independent parameters the optimum performances of both filters, acting on the data from the two auxiliary tests described in Section 3.2, were obtained. The quantitative comparison of their performances is presented in Section 3.5.

After optimization (3.11) and (3.12) were implemented to yield the displacements. The corresponding programs are included in Appendix C.

3.4 Strain Determination by Numerical Differentiation

When the displacement curve has been obtained in the manner described above, it remains for us to derive numerically this empirical function to produce the strains.

Previous to this research [37], the use of an in-phase electronic band-pass filter did not produce a displacement curve sufficiently smooth for derivation purposes and a local averaging process

$$\bar{u}_k = \frac{1}{\delta} \sum_{i=k-\frac{\delta}{2}}^{k+\frac{\delta}{2}} u_i \qquad (3.21)$$

had to be applied twice before differentiation. The summation extended over the number of data points in one fringe.

The resulting strains were calculated by a finite difference approximation

$$\epsilon_k = \frac{\bar{u}_{k+1} - \bar{u}_{k-1}}{2\Delta_k} \tag{3.22}$$

where Δ_k was the sampling wavelength.

The strains obtained in this manner were again averaged twice by the formula

$$\bar{\epsilon}_k = \frac{1}{\delta} \sum_{i=k-\frac{\delta}{2}}^{k+\frac{\delta}{2}} \epsilon_i \tag{3.23}$$

The analysis of this procedure reveals several undesirable features which we will now discuss.

The necessity of an amplitude normalization has already been mentioned as a drawback of the method. Furthermore, since no weights are associated with the point values of the function in the neighborhood of where the derivative is sought, and the finite difference approximation is sensitive to small errors in these values, the convergence of the averaging process to the mean is slow.

Though repeated application of (3.21) and (3.23) does smooth out the displacement and strain curve, it causes us to lose information at the beginning and end of the moiré light intensity trace. In fact, each average shifts the first point at which the smoothed curve can be defined a distance $\delta/2$ along the direction of scanning.

A series of two averaging processes for the displacements and
two for the strains would erase all information on the strain curve
contained in the two moiré fringes closest to every boundary.

In the thermal tests of Chapter IV, the strain determination at
the boundaries of the model was critical since the largest circumfer-
ential stresses occurred at these points. To overcome this difficulty
and to obtain increased accuracy in the derivation procedure, we em-
ployed a method suggested by Lanczos [22]. It provides for the approx-
imation, in the least square sense, of a polynomial of arbitrary degree
n, to a set of experimentally obtained values of a function in the
neighborhood of the point where we wish to define the derivative. This
polynomial is then derived.

The expression for this derivative is

$$\frac{d\rho(x)}{dx} = \frac{\sum_{\alpha=-s}^{s} \alpha\rho(x+\alpha h)}{2\sum_{\alpha=1}^{s} \alpha^2 h} \tag{3.24}$$

where h is the sampling wavelength of the data and s the degree of
the polynomial.

Since the least square approximation is performed in the small,
no significant error is committed. The variation of the degree of the
polynomial can be conveniently performed by the inclusion of s as an
independent parameter in the programming code.

To obtain the derivative at the beginning and end of the dis-
placement curve, (3.24) can be modified [22], or a reflection of the
experimental curve can be performed with respect to the first and last

data point. Both methods have been used in the numerical examples
of Section 3.5.

The fitting of a polynomial to the entire displacement point
function by the method of least squares did not offer a satisfactory
solution because it implied making a decision on the degree of the poly-
nomial approximation that endangered the objectivity of the procedure.

The techniques of differentiation that rely on integration were
considered [22, 33, 34]. The one proposed by Lanczos, as the limit of
(3.24) when the sampling wavelength becomes very short, yielded the
best results with less computing time.

At the limit (3.24) becomes

$$\frac{d\circ(x)}{dx} = \frac{3}{2\eta^3} \int_{-\eta}^{+\eta} t \ f(x+t) \ dt \qquad (3.25)$$

where dx is the sampling wavelength and η defines the limits of the
integration interval.

The strain curve obtained by (3.24) or (3.25) may or may not
be smooth enough for our purposes depending on the amount and the kind
of noise present in our signal. Since the derivative process tends to
magnify small errors in the displacement function that is being derived,
we may wish to apply a final smoothing process to the strain curve
obtained. For this purpose we select a filter of the form [35]

$$\epsilon_n' = \sum_{r=-i}^{i} w_r \ \epsilon(n+r) \qquad (3.26)$$

where ϵ_n are the raw values of the derivative, w_r the weights of the
filter and ϵ_n' the smooth derivative values.

If $w_r = \frac{1}{2i}$ for all r, (3.26) reduces to a local average process identical to (3.23), however, (3.26) affords the possibility of selecting the w_r's to produce a more rapid convergence of the noise ridden function to the smooth for smaller values of i. The choice of the best w_r for a given filtering application depends on the type of noise in the curve of derivative. As will be seen in Section 3.6, several trials are often necessary to obtain the optimum filter weights.

The programming codes corresponding to this section are presented in Appendix C.

3.5 Strain Determination by a Hybrid Computer System

The previous two sections were concerned with purely numerical methods of displacement and strain determination. We will now describe a process that combines the digital procedure of in-phase and in-quadrature filtering that produces the displacement curve with a filtering and derivative circuit obtained on an analog computer. For this purpose we combine a Ramo Wooldridge RW 300 digital computer with an Applied Dynamics AD2 digital system to produce a hybrid computer.

Operations (3.3), (3.10), (3.11) and (3.12) are implemented and performed on the digital section of the hybrid while the equivalent of Equations (3.24) or (3.25) are done on the analog section of the system.

The displacement curve produced by digital methods is smoothed by an analog exponential filter circuit. This filtered version of the displacement curve is derived by another circuit to produce the strain distribution. The details of these circuits are given in Section 3.6.

The advantage of this alternate process of differentiation is the speed with which the curve of strains can be obtained from the analog and the ease with which the parameters that control the amount of filtering on the displacement and strain curve can be varied.

We see that, though the digital methods of Sections 3.3 and 3.4 permit us to take advantage of the continuous law (1.1), reduce the real time of pattern analysis and increase the objectivity of moiré data processing, the versatility of the procedure is somewhat less than ideal since several runs must be made to optimize the independent parameters involved. This can make the method costly in computer time.

As far as we have been able to determine, there exists to date no electronic system that can perform the orthogonalizations (3.6) or (3.10), so we have had to settle for the combination of numerical and analog data processing described above.

3.6 Comparative Performance of the Proposed Techniques

In this section we will present the results obtained by the use of the numerical and analog techniques discussed in Sections 3.3, 3.4 and 3.5 acting on the digitalized version of the light intensity trace corresponding to the tests of Section 3.2.

For the sake of brevity we will agree to call this section Filter 1 to Goodman's linear combination of Tukey filters, and Filter 2 to Ormsby's filter.

a) Displacement determination

As was said in Section 3.3, (3.13) and (3.14) that correspond to Filter 1 were implemented in an IBM 709 programming code.

The independent parameters of this filter are the number of terms in the trigonometric approximation of the transfer function m, and the central frequency of the signal f_o.

In another program (3.17), (3.18) and (3.19) were implemented for Filter 2. This filter has as independent parameters the number of terms in the trigonometric expansion N, the center frequency f_o, the cut-off frequency f_c, the termination frequency f_t and k a factor that defines the extent of the parabolic transition of the roll-off. Both programs contained (3.11) and (3.12) to produce the displacements.

Traction test results

The homogeneous state of deformation of the model affords the possibility of determining quite accurately the band width of the numerical filter. In fact, the transfer function of the filter reduces to

$$H(f) = \begin{cases} 1 & \text{for} \quad f = f_o \\ \\ 0 & \text{for} \quad f \neq f_o \end{cases}$$

However, the actual intensity trace of the moiré fringes of the traction sample showed that at a constant sampling speed the number of data points per fringe varied somewhat due to noise. Therefore, to determine the parameter f_o the average value of the wavelengths was chosen. This f_o was the same for both Filter 1 and Filter 2.

The criterion for the selection of the number of terms in the trigonometric expansion, m and N for Filters 1 and 2, is different for each filter.

Since for Filter 1, m defines also the band width of the transfer function, it is necessary for it to be large enough so that the quotient π/m be very small. This increases the number of terms in (3.13) and (3.14), making the use of the filter costly in computer time to retrieve constant phase cosine waves immersed in noise.

For Filter 2 the situation is entirely different. The existence of independent parameters to define the number of terms in (3.17) and (3.18) and the extent of the band width make it very practical for the purposes of this test.

The roll-off frequency interval can also be narrowed conveniently by the use of the parameters f_c, f_t and k.

The displacement curve obtained with Filter 2 is shown in Figure 23. The computer values appear as discrete points while the theoretical curve is drawn in full line.

The displacements were obtained over base lengths of measurement of δ, $\delta/4$, $\delta/5$, $\delta/8$, $\delta/10$ and $\delta/400$. The standard deviations at the different levels of fractional fringe interpolation varied between an upper bound of $\pm$ 0.001 p or 21' 36" of arc and a lower bound of $\pm$ 0.0003 p or 6' 29" of arc. The maximum variance between two means at different levels of interpolation was found to be 0.00025 p.

The consistency of these results, and the fact that no cyclic variation in the errors of the displacement determination present in earlier work [6] was found to exist in this method, demonstrate that a substantial improvement has been achieved.

The results reported above indicate that the minimum instantaneous angle that can be meaningfully measured by this procedure is 1°.

This implies that we have effectively divided the grid pitch into 360 equal parts, that is, a five-fold increase over previous methods of fractional moiré fringe interpolation.

Disk under compression test results

In this case the light intensity trace along the x-axis of the ring presents strong spatial frequency modulation, Figure 18. This indicates that the frequency composition of the signal is contained in an interval $f_o + \Delta f/2$, where Δf is not negligibly small as in the case of the traction sample. This fact allows Filter 1 to perform more effectively here than in the previous test and we will report the comparative performance of both filters.

The central frequency f_o was determined in terms of data point numbers by inspection of a standard IBM 80 x 80 listing of the data. For Filter 1 several trial runs had to be made to obtain the best combination of the only two parameters available, m and f_o.

Turning now to Filter 2, it again proved to be easier to tune in this test than Filter 1. The reasons for this were explained earlier. The displacement curve obtained is shown in Figure 24. Both filters proved to be able to retrieve the form of the displacement curve precisely. The good approximation between the numerical values of the strains derived below and those obtained by independent means, confirms quantitatively this accuracy.

b) Strain determination

To compute the strains from the displacement curve produced by the filters, (3.24), (3.25) and (3.26) were programmed and the comparative performance of (3.24) and (3.25) analysed. Due to the wealth of data points in our possession, (3.25) could be used with some advantage over (3.24).

To obtain the derivatives at the beginning and end of the sample it was found useful to reflect the displacement curve of the disk under compression with respect to the first and last data point locations. However, for the displacement curve of the traction sample the reflection technique produced a sharp discontinuity with no gain in the accuracy of the derivative. In this case the weights of the polynomial approximation implicit in (3.24) were varied at the ends of the trace as recommended by Lanczos [22].

For the strain curve obtained from the traction test no smoothing with (3.25) was performed, so the values reported below correspond to the straightforward application of (3.24).

For the ring under compression test (3.25) was applied since some scatter of values was noticeable after derivation.

Traction test

The strains obtained in the manner described above between two successive fringes are shown in Figure 25a. The small scale of the plot is intended to indicate the variations about the mean and the average strain determined in Section 3.2.

A histogram was prepared to show the relative frequency of occurrence of the random variable. This variable was subdivided into discrete intervals spanning 10×10^{-6} in./in. The resulting graph is shown in Figure 25b.

The characteristics of this distribution are of interest. A saddle-shaped function replaces the more familiar bell-shaped Gausian distribution we might have expected to obtain. However, the saddle shape insures that 98% of the values of the random variable fall within the interval $\mu \pm 50 \times 10^{-6}$ which is quite sufficient for most engineering applications.

The individual strains plotted in Figure 25a and included in the listing, correspond to a base length of measurement of $\delta/400$. If the 98% certainty that any individual measurement is contained in the interval $\mu \pm 50 \times 10^{-6}$ in./in. is taken as a figure of merit of the proposed techniques, we obtain an accuracy of 50×10^{-6} in./in. in the strain determination. This is well in excess of previous results in moiré work.

Disk under compression test

The numerical differentiation of the displacement curve of Filters 1 and 2 were performed with (3.24) and subsequently filtered with (3.26). Several trial runs were necessary to obtain the best values of the parameters s, i and w_r. The resulting curve of strains can be seen in Figure 26, where one-half of the strain curve corresponds to Filter 1 and the other to Filter 2, for the same values of s, i and w_r.

The full line curve corresponds to the moiré hand analysis of
the problem done by Sciammarella [1], while the dashed curve represents
the results obtained by Durelli and Mulzet [24].

The latter investigators reported natural strains defined as

$$\overline{\epsilon} = \ln(1 + \frac{\ell_f - \ell_o}{\ell_o})$$

where ℓ_o and ℓ_f are the initial and final lengths, respectively.

Since moiré yields Eulerian strains defined as

$$\epsilon = \frac{\ell_f - \ell_o}{\ell_f}$$

the results of [24] were transformed accordingly to permit comparison.

The value of Poisson's ratio for both [1] and our tests was
0.465 while in [24] this value was between 0.47 and 0.48. Since the
strain distribution is a function of this ratio some small inaccuracy
has occurred [24].

The modulus of elasticity in [1] and here is Eulerian while in
[24] it is natural; however, for strains less than 0.03 in./in. both
almost coincide [24].

The percentage of errors committed by Filters 1 and 2 with respect
to the strains obtained in [1] and [24] is presented in the following
table.

As can be seen from the table and Figure 26, Filter 2 produces
a smoother curve that more nearly approximates those of [1] and [24].
Both filters do not perform well near the edges of the disk where the
strains are approaching zero. This is believed to be due to the fact
that long wavelengths have not been properly filtered in the quadrature
process.

TABLE 1

RELATIVE ERRORS IN THE STRAINS OF THE DISK
UNDER COMPRESSION

Filter 1			Filter 2		
Location	Relative to		Location	Relative to	
x/r	[1]	[24]	x/r	[1]	[24]
	%	%		%	%
-1.0	0	0	0.0	4.3	5.5
-0.9	44.5	44.5	0.1	0.0	2.7
-0.8	20.8	20.8	0.2	1.6	1.1
-0.7	22.0	17.0	0.3	7.5	0.0
-0.6	0.0	0.0	0.4	9.3	0.0
-0.5	10.7	4.0	0.5	5.8	3.4
-0.4	9.4	0.1	0.6	16.0	16.0
-0.3	16.4	9.1	0.7	11.0	16.0
-0.2	3.7	0.0	0.8	21.0	21.0
-0.1	1.1	3.8	0.9	60.0	60.0
0.0	3.2	4.2	1.0	0.0	0.0

Now we wish to present the results obtained with the hybrid system of Section 3.5.

The phases obtained with Filter 2 were smoothed with the circuit of Figure 27a; the resulting displacement curve is shown in Figure 27b. These displacements were derived by the circuit of Figure 27c to yield the strains of Figure 27d. The disymmetry in the strain curve is due to the fact that the digital and analog sections of the hybrid system are time locked; thus, there is a progressive delay in the rate at which the data stored in the RW 300 is relayed to the AD2.

The resulting strain curve compares with that obtained in [1] as shown in Figure 28. Again the maximum strain at the center of the ring is 3.6% lower than that of [1]. Several sections of the curve coincide to within ± 0.5%. Other errors calculated are 8.3% at $x/r = 0.3$, and 8.6% at $x/r = 0.50$.

From the consideration of Figures 26 and 28 we conclude that the hybrid system yields a strain curve with less error than that produced by purely numerical techniques for the amount of filtering used in the comparison. However, further numerical filtering could conceivably diminish the errors.

The strains produced by analog means also present larger errors at the edges of the disk for the same reasons explained above.

It might appear paradoxical that at this final stage of the development of a completely computerized system of strain analysis we should check our results against those produced by hand analysis. However, it must be remembered that the ability of the human eye to detect trends in a curve submerged in noise and to select the proper tangent is often difficult to replace by another system.

In a case such as this of a ring under compression where an intelligent analyst has a good idea of what results to expect, the fact that any piece of myopic hardware can compete with him is quite gratifying since total objectivity and tremendous savings in labor and time are welcome bonuses.

CHAPTER IV

THE THERMAL TEST

4.1 The Experimental Set-Up

A general view of the experimental set-up can be seen in Figure 29. Basically it consists of four units: the model, the photographic equipment, the heating and cooling system and the temperature control.

a) The models

The models were disks made of AISI 304 stainless steel of nominal composition 0.06% C, 16% Cr, and 8% Ni. The disks were stress relieved by heat treating. The outer diameter of all models were 5.5 in., the interior diameter varied from 0.5 to 2.5 in. in steps of 0.5 in. The thickness of all rings was 1 in.

We will report here only the results corresponding to what we will call Ring No. 1 with OD = 5.5 in. at 1120°F and ID = 2.5 in. at 920°F, and Ring No. 2 with OD = 5.5 in. at 1580°F and ID = 0.5 in. at 900°F.

The models were engraved with a chemically etched cross-grid of 300 lines per inch on one face. A description of the engravure technique, together with other information regarding the preparation of models for high temperature testing can be found in Appendix A.

b) The photographic equipment

The photographic equipment consisted of a Saltzman enlarger converted to a photographic camera. The details of the transformation were reported earlier by Ross [36]. The interesting features of this camera are its rigidity, the precision gearing that permits accurate positioning of its back and front, and the microinch counters that allow faithful reproduction of relative positions.

Perfect parallelism of the image and object planes can be obtained and preserved for a wide range of object and image distances. The back of the camera can be rotated 360°.

The film was placed against the emulsion side of a high resolution photographic plate which served as the master. Through this plate the film was exposed. The moiré fringe pattern was formed therefore in the image plane of the camera between the image of the model's lines and the master plate.

To make adjustments of focus and to obtain the desired mismatches, the image on the focal plane of the camera could be inspected with the aid of a removable ground glass. Once the adjustments were made the ground glass would be removed, the film loaded in its place, and the camera closed.

The convenient mismatches could be obtained by simply changing the distance between the front and back of the camera, while the object was kept focussed. The rotation of the back of the camers permitted the elimination of all rotation mismatch by minimizing the number of fringes in the image. A further verification of the absence of rotation mismatch

could be performed by varying the size of the image. If the number of fringes increased or diminished without changing direction no such mis-match was present.

The apochromatic photographic lens with a time shutter tested in Chapter II was used to form the image.

A variety of films were evaluated prior to running the test. The films found to record better the fringes at different temperatures are given below.

TABLE 2

FILM PERFORMANCE AS A FUNCTION OF TEMPERATURE

Maximum Temperature (^{o}F)	Film	ASA Speed	Developer
200	Super Panchro Press	250	DK 50
300	Royal Pan	400	DK 50
500	Contrast Process Ortho	50	DK 11
800	Super Speed Ortho	125	DK 50
1600	Royal Ortho	400	DK 50

As we can see, for low temperatures, panchromatic films record well the moiré patterns. As temperatures increase, the fringe contrast is lost with this type of films and orthochromatic films should be used. The reason for this was given in [37].

An important factor in the successful photography of fringes at high temperatures has been found to be the type of light sources used [37]. For all our photography an actinic cold light source with predominant radiation in the wavelength $\lambda = 0.5 \times 10^{-4}$ cm was used.

Good contrast was obtained in the temperature range between 300°F and 1600°F with several orthochromatic films of varying speeds. However, the fastest should be preferred due to the convective air currents that may exist in the space between the model and the lens. These changes in the air density caused by the heat gradient may seriously hinder photography by producing what appears to be a movement of the object.

To keep them at a minimum, the model was surrounded by a chamber and evacuated by a vacuum pump. A polished plate of fused silica separated about 1/4 in. from the model surface closed the chamber towards the camera providing an excellent window. Finally, about 5 in. above the model surface, a polished glass plate was placed parallel to the fused silica.

With these precautions and fast photographic films the convection current problem was overcome completely.

c) The heating and cooling system

The induction heating technique was selected because it allowed an accurate control of the heat input and a perfect simulation of the boundary conditions of the problem.

The induction heating coils were wrapped around the outer circumference of the rings. The diameter of the coils exceeded that of the

rings. The diameter of the coils exceeded that of the ring by 1/8 in. which permitted the thermal insulation of the coil with a uniform layer of a fibrous potassium titanate produced by Dupont under the trade name of Typersul.

The coils functioned as the primary of a transformer and the model as a loaded secondary. This heated the outer perimeter of the rings to a depth of 0.030 in. The power source was a 5 KW radio frequency generator with an operating frequency of 0.375 MC.

The cooling fixture consisted of a hollow aluminum hub, internally cooled by water, to which the interior circumference of the rings were attached. The flow of water through the hub could be controlled. Preliminary tests, with volumes of water that varied between 0.2 and 2.0 gal/min, showed that the amount of flow had little influence on the temperature gradient that could be maintained. This we believe was due to the fact that the hub together with its stand were made of aluminum, thus providing a large area for effective heat dissipation to the air. Figure 30 is a close-up view of the model, induction heating coils, insulator and cooling system.

d) The control system

Iron-constantan thermocouples were fixed by crimping to the lower face of the rings. The cold joint was kept at $32^{\circ}F$. All thermocouple wires were connected through a radio frequency filter and a selection switch to a Leeds and Northroup bridge balance.

In every ring five thermocouples were attached along a radius. One was placed at the outer radius, one at the interior radius, and the remaining three at regular intervals between the first two.

Errors involved in the determination of the temperature distribution were less than 1%. The steady state temperature distribution of Ring No. 1 and Ring No. 2 were compared with the theoretical distribution, under the assumption that the coefficient of thermal conductivity is independent of the temperature. Good correlations were obtained as is shown in Figures 31 and 32.

To control the uniformity of the heat input around the outer circumference and the output around the interior circumference, some rings were prepared with thermocouples fixed on the external and internal perimeter separated ninety degrees of arc one from the other. After steady state heat conduction had been achieved the thermocouple readings indicated that the temperature at the outer circumference was uniform to within $\pm$ 3.5% and the interior circumference to within $\pm$ 4.0%.

4.2 The Operation of the Test

For each ring, the radio frequency generator was set at 2 KW to begin heating. The temperatures were read off the thermocouples and sufficient time was given for the gradient to stabilize. Once the temperatures remained stationary over a period of fifteen minutes, steady state conditions were assumed to have been obtained. A picture of the fringe pattern was then taken and the temperatures recorded.

The plate voltage of the generator was then increased by 0.5 KW. Again time was given for the thermal circuit to reach a steady state condition and another picture was taken, recording the corresponding temperatures.

4.3 Theoretical Solutions to the
Thermal Stress Problem

The interest of theoreticians in finding a solution to this
thermal boundary value problem, considering the material nonhomogeneous
due to the temperature and therefore radial dependence of E, ν and α,
has been considerable. However, experimental data to judge the relative
merit of the necessary simplifying assumptions has been lacking.

Hilton [38] has obtained a closed form solution for a hollow
cylinder subjected to a steady state temperature difference between the
interior and exterior wall under the assumption that E and α are arbi-
trary functions of the temperature and $\nu = 0.5$. He also presented
a series solution for the corresponding plane stress problem.

Chang and Chu [39] studied independently essentially the same
problem with both mechanical as well as thermal loading. They did not
restrict Poisson's ratio to any particular value. However, the tempera-
ture distribution they assumed across the thickness of the cylinder wall
does not appear to be physically meaningful if steady state heat trans-
fer is supposed to exist.

Trostel [40] solved the problem of thermal stresses in a thick-
walled pipe for which $\nu = 0.5$, the coefficient of thermal conductivity
and thermal expansion are linear functions of the temperature, and
Young's modulus is a quadratic function of the temperature.

Nowacki [41] gives further references in the Polish and Russian
literature.

Our temperature measurements, Figures 31 and 32, agree reason-
ably well with the solution to the heat conduction equation under the

assumption that the coefficient of thermal conductivity is independent of the temperature in the range considered. This physical fact was assumed correctly by Hilton and therefore our experimental values were compared with those predicted by his theory.

This comparison however is of a qualitative nature, since Hilton's assumption that the material is incompressible does not permit a quantitative comparison between the theoretical values of the stresses and those measured in a real material.

All investigators agree that the effect of a temperature dependent G and α is to produce different values of the stresses across the ring than those the elastic homogeneous theory with constant G and α would predict.

Whether the stresses increase or decrease will depend on the relative variations of G and α with temperature. No definite statement can be made, one way or the other, unless particular numerical values are considered.

For both rings Hilton's plain-strain solution was computed, assuming a linear variation for G and α, and $\nu = 0.5$. Although in this case the plane-strain solution and the plane-stress solution will give different results, numerical computation of the plane-stress solution was not attempted in view of the lengthy calculations involved and the poor rate of convergence that Hilton has disclosed in his paper.

These values were compared with the elastic solution [42] assuming $G = G_{avr}$ equal to a constant. G_{avr} is taken as the shear modulus corresponding to the average temperature in the cylinder.

The coefficient of thermal expansion was also taken as $\alpha = \alpha_{avr}$ using for the average value the same definition as for the shear modulus. ν was taken equal to 0.5.

For Ring No. 1 both approaches yielded almost identical results with a maximum departure of 4.3%. The results corresponding to Ring No. 2 have been plotted in Figure 40.

The value of the yield stress as a function of temperature, for 304 stainless steel, is as follows:

TABLE 3

YIELD STRESS OF 304 STAINLESS STEEL AS A
FUNCTION OF TEMPERATURE

T (^{O}F)	σ_s (psi)
75	33,000
500	31,500
700	30,000
900	24,000
1100	13,000
1300	11,500
1500	10,000

The values in this table must be kept in mind when considering Figures 38, 39, and 40. Wherever the thermal stresses exceed the value of the yield stress at that temperature, the numerical value of the stress has no significance beyond showing the comparative effect of the temperature dependence of E, ν and α [38].

We must also realize that the values reported in Table 3 have been obtained under physical conditions which are different from those

prevailing in the ring, since the stresses were produced by mechanical loads. Furthermore, the reported yield stresses correspond to an arbitrary definition which does not reflect a real discontinuous transition in the behavior of the material.

4.4 Experimental Determination of Thermal Strains and Stresses

The moiré patterns at the corresponding temperatures can be seen in Figures 33 and 34. Degradation of the image due to the process of reproduction is evident.

From the moiré fringe patterns, the strains shown in Figures 35 and 36 were computed, using the continuous light intensity-displacement law presented in [3] and [4]. The details of the automatic processing of the information were presented in [6].

For Ring No. 1 the strains measured experimentally, Figure 35, show very small departures from the corresponding elastic strains. This is interesting in view of the fact that the value of the stresses would indicate that plasticity has occurred in the vicinity of the inner and outer circumference. Thus, no such elastic theory is rigorously applicable.

For Ring No. 2 the measured strains, Figure 36, show a more definite departure from those predicted by the elastic theory with constant coefficients. However, the elastic theory, while clearly not applicable, would again seem to yield similar values for the strains.

The variation of the mechanical properties of the stainless steel AISI type 304 (18Cr - 8 Ni) used in our tests, are shown in Figure 37. These values were obtained from references [43] and [44].

Figures 38 and 39 show the comparison of theoretical elastic stresses with constant coefficients with stresses determined from experimentally measured strains by the Duhamel-Neumann law with variables E, ν and α.

For Ring No. 1 the differences are small. This coincides with Hilton's theory. For Ring No. 2, the experimental circumferential stresses σ_θ are larger than those of the homogeneous elastic theory as predicted by Hilton's theory. The radial stresses however do not agree. Hilton's solution shows an increase in σ_r while our experiment indicates a decrease in this stress.

In interpreting the above results, the reservations made in Section 5.3 concerning the meaning of the stresses when the yield limit has been exceeded, should be kept in mind. In Hilton's numerical examples the stresses are also of such magnitude as to exceed locally the yield stress of the material.

The tests reported in this chapter seem to indicate that for 304 stainless steel up to 1600°F of maximum temperature and for gradients of 680°F or less the value of the thermal strains do not differ greatly from those calculated by the elastic theory using E_{avr}, ν_{avr} and α_{avr}.

4.5 Residual Strain and Stress Determination

Due to the large circumferential stresses present at both the interior and exterior perimeter of Ring No. 2, the final moiré pattern at room temperature after heating was analysed.

The resulting strains have been plotted in Figure 41. The values of these total residual circumferential and radial strains in the vicinity of the hole and the outer boundary are different from zero and coincide in sign with the strains produced by the thermal load.

The strains measured in this manner, due to the geometrical character of the moiré phenomenon, are the final resulting strains in the body that was initially strain free before the loading. As such, they are the sum of both plastic and residual elastic strains in the body.

In order to separate both components of strain the retrieval of the elastic strain was undertaken by means of a destructive test proposed by Sachs [45].

This test consists of boring out the central portion of the ring around the hole and measuring the variation of the exterior diameter for a given bore size.

To accomplish this, the ring was placed on a vertical milling machine, Figure 42, and secured at the outer perimeter. The boring was made with sharp carbide tool bits with slow machine feeds and abundant cooling. Two jets of water mixed with compressed air were directed towards the interior circumference of the ring for heat removal.

After each cut the sample was allowed to cool to room temperature before performing a measurement. The ambient temperature was recorded to withint 1/2°F and the measured values corrected accordingly.

The variations in the external diameter were measured by means of a Brown and Sharpe transistorized electronic gage capable of reading

0.000010 in. The instrument was connected so that the measurements would not be affected by rigid body motions of the test sample as a whole.

The diametral readings were taken every 30° around the outer circumference of the ring and averaged. The stresses were then calculated in a straight forward manner [45]. The plot of circumferential and radial stresses is shown in Figure 43. The experimental values of the circumferential stress satisfied well the equilibrium condition. From the stresses the residual elastic strains were computed, Figure 44.

Having obtained the total and the elastic residual strains, the residual plastic strains were computed according to the expression

$$\epsilon^T = \epsilon^E + \epsilon^P$$

The residual plastic strains are shown in Figure 45.

The analysis of Figures 41, 43, 44 and 45 show that the total and plastic strains, where they are different from zero, are of the same sign as those produced by the thermal gradient applied. The elastic strains and stresses are of opposite sign to the ones produced by the thermal load.

The ratio of plastic circumferential to plastic radial strain at the edges of the disk, where a state of uniaxial loading can be assumed to exist, is 0.450 inside and 0.475 outside. These ratios differ from the value 0.500 we would have expected to obtain under the assumption of incompressible plastic flow.

The reasons for this, we suspect, are the accumulation of experimental errors in the rather indirect process by which the plastic strains are found and, the extrapolation necessary to obtain the residual, total and elastic circumferential strains at the outer edge of the ring [46].

CHAPTER V

CONCLUSIONS AND RECOMMENDATIONS

5.1 Conclusions

In this research the analysis, based on the MTF of the photo-
optical system used to produce and record the moiré fringe pattern,
has been introduced as a first step in the application of moiré to
experimental stress analysis.

It has resulted in a better understanding of the optical filter-
ing capabilities inherent to the process, and it provides a quantitative
measure of the limit of resolution of the lens, the film and the lens-
film combination. Furthermore, it permits a priori information on the
amount of contrast that can be expected in the image of grids or fringes
of a given spatial wavelength.

The strong dependence of the MTF on the proper focus, the paral-
lelism of object and image plane, the rigidity of the system and the
aperture, were demonstrated numerically.

The comparison of the performances of the ideal and real lens-
film combinations reveals large differences that amply justify the extra
effort of optical testing prior to a moiré application.

This is particularly important in problems of stress concentra-
tion where the displacement gradient around notches or cracks can become
large. Under these conditions, the distance between moiré fringes may

be so small that their contrast in the image plane can be drastically reduced.

Though initial mismatches of adequate sign could correct this problem, it is clear that for a given pitch and no mismatch, there exists for every photo-optical system a limit to the displacement that can be measured dependent on the MTF.

In this work the first steps towards effective optical filtering of a moiré signal have been taken. Again the MTF appears to be the logical tool for the evaluation and comparison of different techniques.

The remarkable properties of a lens in a coherent light field, as an analog device that performs a Fourier transform and displays the Fourier spectrum of a signal, has been brought to the attention of experimental stress analysts.

This idea has been applied with success to the filtering of the grid lines in a moiré fringe pattern.

An incoherent light apodization filter has been implemented empirically to retrieve periodic line patterns immersed in strong random noise. The potential of this filtering technique was thus brought to bear on a problem of particular interest in moiré work.

Methods of numerical in-phase and in-quadrature filtering were applied to overcome certain shortcomings of previously used electronic in-phase filters. With them the phase information contained in the moiré light intensity trace has been obtained without regard to amplitude.

As a result, the minimum phase angle that can be meaningfully measured has been reduced from 5° in previous work [6] to 1°. This implies that we have effectively divided the grid pitch into 360 equal parts.

The accuracy of the displacement determined at this level of interpolation for a carefully tuned filter, has been found to be no more than 30×10^{-5} p and no less than 100×10^{-5} p.

The process of differentiation by which strains are obtained from the experimental curve of displacements, was critically reviewed. The solutions presented offer a degree of accuracy and reproducibility in excess of previous results in moiré work. An average error of 50×10^{-6} in./in. was determined for the strains in an accurately tuned filter.

The thermal strain problem of a ring under axisymmetrical steady state temperature gradient was solved completely by the moiré method. Interesting results on the similarity in the magnitude of the strains predicted by the linear, homogeneous and isotropic theory of elasticity and their experimentally determined values, have been reported.

Since the stresses in the ring during the application of the thermal load exceeded at some points the value of the yield stress at the corresponding temperature, the total residual strains were obtained from the final moiré pattern. The residual elastic strains were obtained by the boring-out method and the residual plastic strains were then obtained by superposition.

This experiment shows that when elastic and plastic components of deformation coexist in a body, moiré, due to its geometrical character, will yield the algebraic sum of the strains. The separation into their respective components can be accomplished only after one of the two is measured by means other than the nondestructive analysis of the final moiré pattern.

The techniques of model grid engravure able to withstand high temperatures, have been presented in detail. The photoengraving techniques, the composition of etchant baths, the engravure times and the current densities reported have produced consistently good results. We hope they will provide useful guidelines for workers in this field.

5.2 Recommendations

The ability of moiré to measure displacements is well known [47, 48, 49], however, its application to strain analysis implies a process of differentiation which is prone to error.

The methods of hand and numerical derivation are costly in real and computer time, respectively, therefore, efforts should be made to implement optically this procedure.

One such technique was proposed by Dantu [50] and another by Parks and Durelli [51]. Both, however, involve a rigid body motion of the moiré pattern or the deformed grid with respect to itself to produce fringes that are the loci of points of equal strain. This shift results in a slight indetermination as to what point in the body is subjected to a given strain.

An optical method of derivation that does not require this displacement would be ideal. In this connection, the optical properties of coherent light systems may yield the basis for an alternate solution.

The minimum photographic, optical, electronic and digital instrumentation necessary to produce, record and analyse moiré patterns along the lines proposed in this research should be determined. The apparatus used here is considered to exceed in many cases what is necessary to obtain results of engineering accuracy.

In the numerical retrieval of phases from the moiré light intensity trace it is conceivable that the decomposition of the signal in other than a trigonometric series could yield faster convergence and more accurate results. This matter would merit further analysis.

Electronic in-phase and in-quadrature filters should be applied for the processing of moiré data in order to increase the versatility and speed of the analysis.

If the statistical properties of the noise in the moiré light intensity trace were known, the requirement that the noise and signal spectrum should be disjoint could be relaxed. This would permit the implementation of a filtering technique more powerful than the ones presented here. However, the task of characterizing the noise content of moiré fringe patterns obtained under diverse conditions of practical interest has not been done to date.

Based on the complete strain determination made for the stainless steel ring, a thermoplastic analysis in terms of stresses can be attempted. This will require the knowledge of the stress-strain relation in the elastic and plastic region of behavior of the metal.

Some of these ideas are being pursued in the continuing research
effort of which this dissertation is a part; others remain as avenues
possibly worth exploring by anyone attracted to this matter of large
field strain analysis by a method of such direct visual appeal as moiré.

APPENDIX A

ON LINEAR FILTER THEORY

A.1 Linear Systems

For the purpose of this appendix a linear system is a linear operator L, such that for all functions $\varphi(x)$ and $\psi(x)$ in the space domain and all scalars a, b, the following relation holds

$$L[a\,\varphi(x) + b\psi(x)] = aL[\varphi(x)] = + bL[\psi(t)] \qquad (A.1)$$

and that, if

$$L[\psi(x)] = \varphi(x) \qquad (A.2)$$

and x_o is a real constant, then

$$L[\psi(x - x_o)] = \varphi(x - x_o) \qquad (A.3)$$

that is, L is invariant under a space transformation.

Then, if

$$L[\delta(x)] = h(x) \qquad (A.4)$$

$$L[\delta(x - x_o)] = h(x - x_o) \qquad (A.5)$$

it follows that

$$\varphi(x) = \int_{-\infty}^{\infty} \psi(\epsilon)h(x - \epsilon)\,d\epsilon \qquad (A.6)$$

If we call $\varphi(x)$ the output of the linear system L and $\psi(x)$ the input, (A.6) indicates that the output of L is given in terms of the input and a unique function $h(x)$ called the weight function or impulse response of L.

The Fourier transform of h(x) is called the transfer function of L and is given by

$$H(f) = \int_{-\infty}^{\infty} h(x)e^{-2\pi i f x} \, dx \qquad (A.7)$$

If we recognize (A.6) as the convolution product we can write

$$\varphi(x) = \psi(x) * h(x) \qquad (A.8)$$

and

$$\Phi(f) = \Psi(f) \cdot H(f) \qquad (A.9)$$

where $\Phi(f)$, $\Psi(f)$ and $H(f)$ are the Fourier transforms of $\varphi(x)$, $\psi(x)$ and $h(x)$ in that order.

From (A.9) we obtain immediately the transfer function that will produce a desired output whose transform is $\Phi(f)$ from an input $\psi(f)$ is

$$H(f) = \frac{\Phi(f)}{\Psi(f)} \qquad (A.10)$$

The expression for $H(f)$ is in general complex and of the form

$$H(f) = A(f)e^{i\theta(f)} \qquad (A.11)$$

We will restrict our attention to linear transformations involving no phase shift, thus

$$\theta(f) = 0 \qquad (A.12)$$

We define a low-pass filter as a filter for which $A(f)$ is small in some sense for $|f| > f_c$, where f_c is called the cut-off frequency. A band-pass filter is a filter where $A(f)$ is small outside an interval $|f \pm \frac{\Delta f}{2}|$, Figure 18.

The ideal band-pass filter would have the following transfer function, Figure 3-1a

$$H(f) = A(f) = \begin{cases} 1 & |f_o - \frac{\Delta f}{2}| \leq |f| \leq |f_o + \frac{\Delta f}{2}| \\ \\ 0 & |f_o - \frac{\Delta f}{2}| > |f| > |f_o + \frac{\Delta f}{2}| \end{cases} \quad (A.13)$$

A.2 Definition of a Digital Filter

If the function $\psi(x)$ defines a generalized function, is band limited and we possess its sampled values obtained at a sampling frequency f_s which is at least twice as large as the largest frequency f_α present in the function, Shannon's sampling theorem guarantees that $\psi(x)$ can be uniquely determined from its sampled values

$$\psi_n = \psi(\frac{n}{2f_\alpha}) = \psi(\frac{n}{f_s})$$

by the infinite series

$$\psi(x) = \sum_{n=-\infty}^{\infty} a_n \psi_n \quad (A.14)$$

If $H(f)$ is such that $\overline{H}(f)$ can be written as a trigonometric series, then

$$\overline{H}(f) = \sum_{n=-\infty}^{\infty} a_n e^{2n\pi i \frac{f}{f_s}} \quad (A.15)$$

The transform of (A.15) will be

$$\overline{h}(x) = \sum_{n=-\infty}^{\infty} a_n \delta(x + \frac{n}{f_s}) \quad (A.16)$$

If we define the convolution $\bar{h}(x) * \psi_n$, where ψ_n is the space sampled version of $\psi(x)$, then the sampled version of the desired output $\varphi_n = \varphi(\frac{n}{f_s})$ will be given by

$$\varphi(\frac{n}{f_s}) = \sum_{n=-\infty}^{\infty} a_n \; \psi(\frac{m+n}{f_s}) \tag{A.17}$$

For computational purposes the infinite series (A.15), (A.16) and (A.17) have to be replaced by finite summations, then (A.15) becomes

$$\bar{H}_N(f) = \sum_{n=-N}^{N} a_n \; e^{2n\pi i \frac{f}{f_s}} \tag{A.18}$$

and (A.17)

$$\bar{\varphi}_n = \sum_{n=-N}^{N} a_n \; \psi_{m+n} \tag{A.19}$$

where $\bar{\varphi}_n$ is a good approximation of $\varphi(\frac{n}{f_s})$ through (A.19).

Equation (A.19) is the fundamental formula of digital filtering [33] and is sometimes referred to as a finite moving average process [32].

APPENDIX B

ON THE PREPARATION OF METAL MODELS
FOR HIGH TEMPERATURE MOIRÉ TESTS

B.1 Introduction

Whatever means we have for analyzing the moiré data, we are interested in obtaining the fringe patterns as free as possible of noise. This noise obscures the meaningful signal and makes the processing of the information more difficult and less accurate.

If, as is customary, a photograph is used as a means of memorizing the moiré pattern, this noise will appear as spots, blemishes or variations of background intensity in the negative.

High temperature tests are especially prone to this inconveniency due to the fact that organic and inorganic substances used to print lines on the model change color with temperature.

The non-uniformity of the temperature fields investigated will cause a variation of the model's color that will show as low spatial frequency variations of the background intensity on the photograph. Dust, scratches or pits on the model surface will appear as high frequency disturbances on the recorded pattern of fringes.

To obtain the best moiré, over a wide range of temperatures, a heat resistant grid of excellent quality must be engraved on the model. This involves the careful completion of the following three steps:

Surface finishing of the model

Photo-engravure of the grid

Chemical etching of the grid

B.2 Surface Finishing of the Model

In general it can be said that the surface of the model that is
to be engraved with lines should be polished until free from pits and
scratches. The amount of remaining unevenness that can be tolerated
will depend on how this shows on the picture of the moiré pattern. Also,
if the surface roughness hinders the printing of the lines, or if it
permits under etching of the photo-resist, finer polishing will be
called for.

A decrease in the grid pitch will necessitate an increase in
the surface polish. We can appreciate, here again, the advantage of
being able to work with fewer lines per inch for a given sensitivity.

Softer metals, like copper and aluminum, can be finished by
hand on a lapping table if the model is not too large. The usual pro-
cedure is to polish them with progressively finer emery paper until we
obtain a suitable finish. For 300 lines per inch this was found to be
grit No. 400 A.

Harder metals and samples of larger size cannot be easily
polished by hand. The stainless steel models prepared for the tests
in the main text were ground and polished mechanically to a 15 micro
inch finish which proved sufficient for engraving 300 lines per inch.

It was found necessary to nickel plate electrically or chem-
ically all mild steel test pieces for thermal testing. This prevented

the oxidation of their surface that reduced the contrast between the grid lines. The thin plated layer was then polished and engraved.

For more critical engraving work, such as 750 lines per inch in metal samples, it was necessary to increase the mechanical grinding and polishing to obtain a 6 micro inch finish for good engravings. A typical example of insufficient surface polishing in an aluminum sample engraved with a cross grid of 750 lines per inch can be seen in Figure 46.

A very satisfactory surface finish can be obtained by electro-polishing the surface to be engraved. Almost without exception etching baths will serve as good polishers if conveniently diluted, or if the current densities used for etching are reduced to an adequate level to permit polishing.

Such is the case of the sodium hydroxide bath for aluminum and the orthophosphoric bath for stainless steel described below.

Aluminum polishing:

      2 oz sodium hydroxide pellets

      1 gal water

      30 amp per sq ft current density

Stainless steel polishing:

      1 vol orthophosphoric acid (85% conc)

      6 vol water

      72 amp per sq ft current density

If the polishing times are found to be too long for some applications, the bath can be activated either electrically or by increasing the acid or alkali concentration.

The work to be polished should present a uniform surface finishing, with no deep scratches or pits, before immersion in the bath, since the action of the electropolishing will not eliminate, but rather accentuate, any large crevice in the surface.

By careful electropolishing surfaces can be finished to receive photo-engraved or chemically milled 750 to 1000 lines per inch by the processes that will now be described.

B.3 Photo-Engravure of the Grid

Photo-resists have two properties that make them useful for moiré work. One is their ability to reproduce photographically by contact a grid printed on a negative which we call film master. Another is their resistance to acid and alkali that permits us to etch chemically the areas of the metal surface between the lines protected by resist.

Two commercially available photo-resists have been employed extensively by us. These are the Kodak Photo Resist manufactured by the Eastman Kodak Company of Rochester, New York, and the Dynachem Photo Resist, distributed by Lithoplate, Inc., of Covina, California, for the Dynachem Corporation.

Both require handling in subdued tungsten illumination. A 15W bulb not less than 2 ft away proved to be satisfactory.

A listing of operations and times that consistently yielded very good photo-engravures follows.

Photo-engravure with Kodak Photo Resist (KPR):

a) Spray or whirl on a fine even coat of KPR and let dry.

b) Expose master grid and model in vacuum frame to 20 amp carbon arc lamp at 1 ft distance for 4 min.

c) Develop with KPR developer for at least 4 min. Longer developing times have no effect on the image quality.

d) Flow with KPR dye for 1 min.

e) Wash with water.

f) Blast with air to dry.

g) Heat in oven for 30 min at 470°F. Then allow to cool to room temperature before further handling.

Photo-engravure with Dynachem Corporation Resist (DCR):

a) Spray the surface placed vertically with a slow horizontal sweeping motion, advancing from bottom to top.

b) Lay sample flat for 2 min to allow the dry-wet coating to settle to a uniform thickness.

c) Place specimen in an oven or on an open electric hot plate for 8 to 10 min at 140°F. Then allow to cool.

d) Expose in vacuum frame with master for 7 min.

e) Develop in DCR developer for 30 to 60 sec. The developing time is critical.

f) Spray on DCR dye. Leave dye on surface for 5 sec.

g) Wash in water.

h) Blast with air to dry.

i) Place in an oven or on a hot plate and heat for 30 min at 240°F. Then allow to cool to room temperature before further handling.

For both the KPR and DCR processes the optimum exposure and developing time will depend on the thickness of the coating applied. Since the thickness of this thin film is difficult to monitor by elementary means, some experimentation will always be necessary to obtain the best results.

Figure 47 is a 40X magnification of a dyed photo-engraved crossed grid of 300 lines per inch. The rounding of the corners is due to light diffusion in the photo-sensitive coating thickness.

Some manufacturers of photo-resists recommend that the resist should not be dyed if maximum resistance to the etchant is desired. This precaution was taken in the engravure of the stainless steel rings of the main text. The evaluation of the quality of the photo-engraved grid was performed by inspection of the moiré pattern produced by the engravure with the master. The usual inspection by microscope proved to be very difficult since the resist is colorless and transparent.

In an earlier paper [52], where a thermal problem of the same geometry as the one presented in this dissertation was studied, 1000 lines per inch were photo-engraved with dyed KPR as explained above. This printing process produced moiré patterns up to 400°F. However, the changes in color of the organic coating did produce some undesirable background intensity variations.

Since most photo-resists clear at about 600°F. and turn to white ash at 750°F, 500°F seems to be the limit of applicability for this method of engraving thermal test pieces.

B.4 Chemical Etching of the Grid

Having completed all the steps described in Section B.3, the sample can be immersed in an acid or alkali etch bath.

The following solutions have been found to be effective etchants [53]:

For aluminum, a 3% concentration caustic soda solution, made by dissolving 4 oz sodium hydroxide pellets in 1 gal water. For a more active bath the concentration can be increased to 9% by dissolving 12 oz sodium hydroxide per 1 gal water.

For copper, an 8% concentration hydrochloric acid, prepared by adding 10 oz 38% hydrochloric acid to 1 gal water.

For nickel and copper, 1 gal photoengravers iron chloride (40° Be) added to 6 oz 38% hydrochloric acid. Keep the temperature of the bath below $110^{\circ}F$ by suitable cooling.

For mild steel [54], a 5% concentration nitric acid solution.

For stainless steel, a solution of 33% orthophosphoric acid, 57% of specific gravity 1.26, and 10% water. A current density of 72 amp per sq ft is applied to the sample made anodic.

The time the model can be left in the bath will depend on

      a) the depth of etching required

      b) the resistance of the photo resist

      c) the amount of under-etching that develops.

a) The bath, according to its concentration and the current density applied to the sample, removes material at a constant rate, e.g., a bath of 1 volume of 38% hydrochloric acid and 4 volumes of water, at 4 amps per sq in. and 2 volts, removes material from a stainless steel plate at 0.001 inch per minute. By periodic inspection of the etched surface under the microscope, the frequency of the inspections will depend on the activity of the bath, we are able to control the process and remove the sample when the lines are etched to sufficient depth.

If this time is recorded, similar samples will take approximately equal times to be etched the same amount as long as the bath does not become exhausted. Aging of the bath will result in longer etching times if the current densities are kept constant.

b) What was said above implied a resist which would withstand the action of the bath as long as we desired. This will not be true if the cleanliness prior to application of the photo-resist were not perfect, the thickness of the protective layer were not enough, the exposure incorrect, the baking insufficient or abrasion had destroyed the continuity of the engraved grid.

It is important to note that underexposure of the photo-resist causes the developer to wash away protective coating, while overexposure will cause stripping of the coating in the wash after developing.

All the above mentioned causes will diminish the resistance of the photo-resist and may cause it to strip off the surface it is protecting before the necessary depth of etching has been achieved.

When grids are being etched the stripping of the resist in some localized areas will force us to interrupt the etching entirely. Failure to do this will cause indiscriminate etching of the unprotected metal, thus erasing whatever line pattern had been etched already. Longer periods of etching will eventually cause pitting in the unprotected areas and more stripping due to underetching as will be explained.

c) We have called underetching, for lack of a better name, the attack on the sides of the partially etched trough by the etchant, that causes metal adhered to the resist on the model surface to be removed from below, Figure 48a and 48b.

The photo-resist can then strip off by the removal of metal to which it was adhered.

We have found in repeated testing that the maximum depth of etching without significant underetching for Ronchi type rulings varies between 0.5 p for KPR to 0.75 p for DCR.

Failure to extract the sample from the etch bath when underetching has begun will produce an increase of the width of the etched lines making the grid lose its Ronchi characteristic, Figure 48c. Further underetching will produce rounding off of the line edges by gradual stripping of the underetched resist. This will diminish the contrast between lines of the engraved grid and upon superposition with the master, a less well-defined moiré will result.

As we have seen, the depth of etching depends on various factors all of which must be carefully controlled. The main difficulty in the production of a good, deeply etched model is the stripping of the resist in the etch bath before sufficient etching has occurred.

As we said before, even if the stripping is local, the uniformity of the grid will be affected if the model is not removed immediately from the solution.

If etching has not begun before the resist strips off, we will be able to remove the remainder completely, and, after cleaning thoroughly the metal surface, proceed to repeat the photo-engravure correcting whatever caused the resist to fail.

However, if the etching had begun before the masking failed, but had not progressed to enough depth for our purpose, we are left

with a shallow etched surface. Since this etching has destroyed our surface finish, we are obliged to return our sample to the very first stage of its preparation. This not uncommon occurrence is disheartening and time consuming.

There is a method used by engravers that increases the resistance of the resist during the etching process that corrects small deficiencies that might develop in the continuity of the coating. It involves the use of a substance known in the trade as Dragon's Blood. This is a very fine organic red powder that can be applied on the wet surface that is being etched with a soft camel's hair brush. The motion of the brush should be perpendicular to the direction of the grid lines allowing the powder to dissolve and be swept against the sides of the lines and into any small pit in the resist.

If the model's surface is then dried with hot air, the dissolved powder will adhere to the resist and build up on the etched corners, as can be seen in Figure 48d. This added protection will permit deeper etching.

Though this treatment has been proven effective for etching coarse grids of 50 to 150 lines per inch, its use has not yielded significant improvement for denser grids. It seems obvious that when the interline spacing is reduced it becomes increasingly difficult for the dissolved powder to get between the lines.

We would wish to be able to take a shallow etched surface and photo-engrave a new resist grid, identical to the one that stripped off, and continue etching. This implies the necessity of placing our

master exactly in the same position with respect to the model's surface as it was when we exposed the now destroyed grid.

Because the master is made of straight parallel lines of constant pitch, free of any significant periodic error, the above correspondence requires only the exact superposition of one line of the master with one line of the semi-etched model. It is conceivable that such superposition could be accomplished with the aid of a microscope and a great deal of patience.

A macroscopic method of superposition has been employed with success for this same purpose. It consists of superimposing the partially etched model, sensitized with unexposed photo-resist, with a photographic glass copy of the master grid. By eliminating all moiré fringes due to rotation, absolute parallelism of both sets of grids can be insured. By displacing without rotation the master with respect to the model, a change in the light intensity reflected from the model is produced. The maximum reflected intensity over the entire model surface will indicate the position in which the correspondence between the partially etched lines of the model and the dark lines of the master is perfect. Upon obtaining this correspondence the model can be exposed in intimate contact with the master in a vacuum device. The only requirement for this method to be applicable is that the partial etching be sufficient to produce at least a faint moiré pattern.

When only shallow etching is possible in a metal due to the grid pitch or other circumstances, an alternative method to the standard procedure described above can be used. This consists of selecting the

reducing or oxidizing atmosphere and temperature that will cause the metal surface to change color. This transformation can be made to take place only to a very shallow depth from the sample surface and not destroy the surface finish.

Based on this principle polished stainless steel samples were introduced in a hydrogen furnace. The machine used was a Sargeant and Wilbur oven manufactured by Sargeant and Wilbur, Inc., of Pantucket, Rhode Island. The furnace was operated at $1000^{\circ}C$ with a 15 cu ft per min flow of wet hydrogen. The samples were left in the oven for 30 min.

This treatment left the surface of the stainless steel colored dark green. The depth of the color layer depends on the extent of the chrome reduction and can be regulated by the time the sample is left in the oven.

On removal from the oven, and after cooling, the samples were photo-engraved and placed in the etching bath. A very shallow etch cut through the thin green layer exposing the bright polished metal below.

The final step in the preparation of samples for thermal tests, after the etching of the model has been completed, is the removal of all traces of resist from the surface prior to heating. Failure to do this will result in the organic coating first changing color and then burning off while the test is in progress. To accomplish this cleaning KPR "Strip-Ur" SK 4 and SK 5 distributed by Etchomatic, Inc., for Spar Kleen Products, Inc., was found to be effective.

Figure 49 is a 40X magnification of an etched cross grid of 300 lines per inch in stainless steel with all traces of resist removed. Some underetching has caused the lines to narrow between crossings. The rounded appearance of the etched holes is due to the diffraction of light during photographic printing as was explained above.

APPENDIX C

PROGRAMMING CODES

```
C         GOODMAN S COMBINATION OF TUKEY IN PHASE AND IN
C         QUADRATURE FILTERS
C
          DIMENSION BX(500),BY(500),DATA(4000),TAN(4000)
          DIMENSION FMT (12), TITLE (7),RAN(4000),DUM(100)
          PI=3.1416
          P8=8./PI
          P4=4./PI
          RRD=IHT
C
C         FMT=FORMAT OF DATA
C         TITLE=TITLE OF DATA
C         NDATA=NUMBER OF DATA
C         DATA=DATA POINT
C
          READ INPUT TAPE 5,25,(FMT(I),I=1,12)
       25 FORMAT (12A6)
          READ INPUT TAPE 5,26,(TITLE(I),I=1,7)
       26 FORMAT (7A6)
          READ INPUT TAPE 5,3,NDATA
        3 FORMAT(I4)
          READ INPUT TAPE 5,FMT,(DATA(I),I=1,NDATA)
C
C         RID=LETTER T IN COLUMN 1 TO IDENTIFY TUKEY S PARAMETER
C         CARD
C         TERMS= NUMBER OF TERMS IN TRIGONOMETRIC EXPANSION OF
C         TRANSFER FUNCTION
C         CW=CENTER WAVELENGTH IN DATA POINTS
C         NST=DEFINES STARTING DATA POINT NUMBER FOR ABOVE
C         PARAMETERS
C         NFN=DEFINES END DATA POINT NUMBER FOR ABOVE PARAMETERS
C
        7 READ INPUT TAPE 5,1,RID,TERMS,OW,NST,NFN
        1 FORMAT(A1,F9.0,F10.0,2I10)
          IF(RID-RRD) 13,14,13
       13 WRITE OUTPUT TAPE 6,15
       15 FORMAT(10X,15H ERROR IN NDATA)
          CALL EXIT
       14 IF(NST+NFN) 11,12,11
       12 NST=1
          NFN=NDATA
       11 IF(TERMS) 9,9,10
       10 M=TERMS-1.
          WRITE OUTPUT TAPE 6,27,(TITLE(I),I=1,7)
       27 FORMAT (1H17A6,6X12HTUKEY FILTER//)
          WRITE OUTPUT TAPE 6,28,TERMS,OW,NST,NFN
       28 FORMAT (9H TERMS = F10.6,6H OW = F10.6,7H NST = I6,
         $7H NFN = I6///)
          WRITE OUTPUT TAPE 6,29
       29 FORMAT (X6HNUMBER6X10HINPUT DATA13X7HVALUE X15X
         $7HVALUE Y14X
         $ 9HRESULTANT15X5HTHETA//)
          WO=2.0*PI/OW
          PM=PI/TERMS
```

```
      T8=8./TERMS
      PM2=PM*2.
      T4=4./TERMS
      CAST=-(0.54-0.46)*T4
      TW=TERMS*WO
      CASTY=CAST*SINF(TW)
      CASTX=CAST*COSF(TW)
      AY=0.
      AX=0.
      DO 2 J=1,M
      R=J
      DD=R*PM
      D=COSF(DD)
      C=0.54+0.46*D
      E=R*WO
      EY=SINF(E)
      EX=COSF(E)
      CD=C*D
      AY=AY+C*EY*EY*SINF(PM2*R)/R
      AX=AX+CD*EX*EX*SINF(DD)/R
      BY(J)=CD*EY
    2 BX(J)=CD*EX
      AY=AY*P4
      AY=1./AY
      AX=(P8*AX)+T4
      AX=1./AX
  100 FORMAT(10X,E20.8)
      TOTAL=0.
      RDATA=NDATA
      DO 20 I=1,NDATA
   20 TOTAL=TOTAL+DATA(I)
      TOTAL = TOTAL/RDATA
      DO 21 I=1,NDATA
   21 DATA(I)=DATA(I)-TOTAL
      DO 4 K=NST,NFN
      VALY=0.
      VALX=0.
      NAN=M+K+1
      NNN=K-M-1
      TAX=CASTX*(DATA(NAN)+DATA(NNN))
      TAY=CASTY*(DATA(NAN)+DATA(NNN))
      DO 5 J=1,M
      NAN=K+J
      NNN=K-J
      VALY=VALY+BY(J)*(DATA(NAN)+DATA(NNN))
    5 VALX=VALX+BX(J)*(DATA(NAN)+DATA(NNN))
      VALY=(T8*VALY+TAY)*AY
      VALX=T8*VALX+T4*DATA(K)
      VALX=(VALX+TAX)*AX
      AXT=(VALY/VALX)
      OTAN=ATANF(AXT)
      RAN(K)=SQRTF( VALX*VALX+VALY*VALY)
      TAN(K)=SIGNF(OTAN,AXT)
```

```
      4 WRITE OUTPUT TAPE 6,6,K,DATA(K),VALX,VALY,RAN(K),TAN(K
                                   )
      6 FORMAT(X,I5,(5(2X,E20.8)))
        GO TO 7
C
C       RAN=PHASER LENGTH
C       TAN=PHASES PRODUCED BY THE FILTER
C       DUM=DUMMY VARIABLE FOR PLOT DIMENSION 100
C
      9 CALL RPLT(TAN,NDATA,DUM)
        CALL RPLT(RAN,NDATA,DUM)
        WRITE OUTPUT TAPE 6,30,(TITLE(I),I=1,7)
     30 FORMAT(1HP,7A6,6X12HTUKEY FILTER)
        WRITE OUTPUT TAPE 6,31,NDATA
     31 FORMAT(1HP,I4)
        CALL POUT (TAN,NDATA)
        CALL DIFTN(TAN,NDATA,DATA,RAN,BX,DUM,BY)
        CALL EXIT
        END
```

```
C         ORMSBY BAND PASS IN PHASE AND IN QUADRATURE FILTERS
C
          DIMENSION A(10),H(100),Z(4000),DUM(100),OUT(4000)
          DIMENSION HQ(100),BOUT(4000)
          DIMENSION FMT (12), TITLE (7)
          RRD=1HO
          P=3.14159
C
C         FMT=FORMAT OF DATA
C         TITLE=TITLE OF DATA
C         NDATA=NUMBER OF DATA
C         Z=DATA POINT
C
          READ INPUT TAPE 5,25,(FMT(I),I=1,12)
       25 FORMAT (12A6)
          READ INPUT TAPE 5,26,(TITLE(I),I=1,7)
       26 FORMAT (7A6)
          READ INPUT TAPE 5,100,NDATA
      100 FORMAT(I4)
          READ INPUT TAPE 5,FMT,(Z(I),I=1,NDATA)
          TOTAL=0.
          RDATA=NDATA
          DO 20 I=1,NDATA
       20 TOTAL=TOTAL+Z(I)
          TOTAL=TOTAL/RDATA
          DO 21 I=1,NDATA
       21 Z(I)=Z(I)-TOTAL
C
C         RID=LETTER O IN COLUMN 1 TO IDENTIFY ORMSBY'S
C         PARAMETER CARD
C         XN1=NUMBER OF TERMS IN TRIGONOMETRIC EXPANSION OF
C         TRANSFER FUNCTION
C         TD=MAXIMUM WAVELENGTH IN DATA POINTS TO PASS THE
C         FILTER
C         TC=UPPER CUTTOFF WAVELENGTH IN DATA POINTS
C         TO=CENTER WAVELENGTH IN DATA POINTS
C         RK=DECIMAL EXTENT OF THE PARABOLIC TRANSITION
C         NST=DEFINES STARTING DATA POINT NUMBER FOR ABOVE
C         PARAMETERS
C         NFN=DEFINES END DATA POINT NUMBER FOR ABOVE PARAMETERS
C
        7 READ INPUT TAPE 5,1,RID,XN1,TD,TC,TO,RK,NST,NFN
        1 FORMAT(A1,F9.0,4F10.0,2I10)
          IF(RID-RRD) 43,44,43
       43 WRITE OUTPUT TAPE 6,45
       45 FORMAT(10X,15H ERROR IN NDATA)
          CALL EXIT
       44 IF(NST+NFN) 41,42,41
       42 NST=1
          NFN=NDATA
       41 IF(XN1) 49,49,40
       40 WRITE OUTPUT TAPE 6,27,(TITLE(I),I=1,7)
       27 FORMAT (1H17A6,6X13HORMSBY FILTER//)
          WRITE OUTPUT TAPE 6,28,XN1,TD,TC,TO,RK,NST,NFN
```

```
    28 FORMAT (7H XN1 = F10.6,6H TO = F10.6,6H TC = F10.6,
      $6H TD = F10.6,
      $ 6H RK = F10.6 / 7H NST = I6,7H NFN = I6///)
       WRITE OUTPUT TAPE 6,29
    29 FORMAT (X6HNUMBER6X10HINPUT DATA13X7HVALUE X15X
      $7HVALUE Y14X
      $ 9HRESULTANT15X5HTHETA//)
       NTO=TO/(XN1+XN1)
    10 TO=1.0/TO
    11 TC=1.0/TC
    12 TD=1.0/TD
    13 TC=TO-TC
    14 TD=TO-TD
    15 TD=TC-TC
    16 P2=P+P
    17 N1=XN1+1.0
    18 N2=N1+N1-1
    19 TR=TC
       DO 2 K=1,N2
       N=K-N1
       IF(N) 3,4,3
     3 R=N*NTO
       PN2=P2*R
       RM1=1.0-RK
       A1=SINF(PN2*(TC+RM1*TR))
       A2=SINF(PN2*(TC+RK*TR))
       A3=SINF(PN2*(TC+TR))
       A4=SINF(PN2*TC)
       A5=RK*RM1*TR*TR*P*R*PN2*PN2
       H(K)=(A1+A2-A3-A4)/A5
       P2NTO=PN2*TO
       H(K)=H(K)+H(K)
       HQ(K)=H(K)*SINF(P2NTO)
       H(K)=H(K)*COSF(P2NTO)
       GO TO 2
     4 H(K)=TC+TC+TR
       HQ(K)=0.
     2 CONTINUE
       DO 6 K=NST,NFN
       T=K
       RI=0.
       RQ=0.0
       DO 5 I=1,N2
       L=K+(I-N1)*NTO
       IF(L) 5,5,8
     8 IF(NDATA-L) 5,5,9
     9 RI=RI+H(I)*Z(L)
       RQ=RQ+HQ(I)*Z(L)
     5 CONTINUE
       OUT(K)=SQRTF(RI*RI+RQ*RQ)
       BOUT(K)=ATANF(RQ/RI)
       WRITE OUTPUT TAPE 6,22,K,Z(K),RI,RQ,OUT(K),BOUT(K)
    22 FORMAT(X,I5,(5(2X,E20.8)))
     6 CONTINUE
```

```
      GO TO 7
C
C     OUT=PHASER LENGTH
C     BOUT=PHASES PRODUCED BY FILTER
C     DUM=DUMMY VARIABLE FOR PLOT DIMENSION 100
C
   49 CALL RPLT(OUT,NDATA,DUM)
      CALL RPLT(BOUT,NDATA,DUM)
      WRITE OUTPUT TAPE 6,30,(TITLE(I),I=1,7)
   30 FORMAT (1HP7A6,6X13HORMSBY FILTER)
      WRITE OUTPUT TAPE 6,31,NDATA
   31 FORMAT (1HPI4)
      CALL POUT(BOUT,NDATA)
      CALL DIFTN(BOUT,NDATA,Z,OUT,H,DUM,HQ)
      CALL EXIT
      END
```

```
C       PROGRAM DIFTN USING LANCZOS FORMULA FOR
C       DIFFERENTIATION WITH WEIGHTS CHANGED TC ZERU  BEYONC
C       ENC POINTS
C       PROGRAM CORRECTS FOR CYCLIC DISCONTINUITY OF THE ARC
C       TANGENT FUNCTION
C
    1 FORMAT(I4)
    2 FORMAT(6E12.0)
    3 FORMAT(5E20.5)
    6 FORMAT(2F10.0)
   41 FORMAT(1H1,//,10X,26H RDATA,FRING,WICTH,DX,CGF=,5E18.5
                                    )
   42 FORMAT(12A6)
   43 FORMAT(/,10X,12A6)
   40 FORMAT(///,18X,2H X,16X,4H TAN,15X,5F TAN2,15X,5H DTAN
                                    ,
     $12X,8H STRAINS)
      DIMENSION DTAN(4000),DTR(100)
      CIMENSION TAN(4000),TAN2(4C0C),A(100),TR(100)
C
C       KR=NUMBER OF POINTS IN PCLYNOMIAL APPRCXIMATION IN THE
C       NEIGHBORHCOD OF THE POINT WHERE THE CERIVATIVE IS
C       SOUGHT
C       FRING=NUMBER CF LINES PER INCH OF THE MASTER
C       WICTH=LENGTH OF THE MODEL IN THE DIRECTICN OF SCAN
C       A=TITLE OF THE DATA
C       NCATA=RDATA=NUMBER UF DATA PCINTS
C       TAN=PHASES GENERATED BY FILTER
C
      REAC INPUT TAPE 5,1,KR
      REAC INPUT TAPE 5,6,FRING,WICTH
      READ INPUT TAPE 5,42,(A(I),I=1,12)
      REAC INPUT TAPE 5,1,NDATA
      REAC INPUT TAPE 5,2,(TAN(I),I=1,NDATA)
      PI=3.1416
      NT=NCATA/100
      RDATA=NCATA
      CX=WIDTH/RDATA
      COF=1.0/(2.C*FRING*PI*DX)
      WRITE CUTPUT TAPE 6,41,RCATA,FRING,WIDTH,DX,COF
      WRITE OUTPUT TAPE 6,43,(A(I),I=1,12)
      WRITE OUTPUT TAPE 6,40
      AMUL=0.
      DO 5 K=1,NDATA
      A1=TAN(K)-TAN(K-1)
      A1=SIGNF(2.,A1)
      A2=TAN(K-1)-TAN(K-2)
      A2=SIGNF(1.,A2)
      A3=SIGNF(4.,TAN(K))
      A4=SIGNF(3.,TAN(K-1))
      AA=(A1+A2+A3+A4)
      AA2=ABSF(AA)
      IF(AA2-3.0) 10,11,11
   10 IF(AA) 12,11,13
```

```
   12 AMUL=AMUL+PI
      GO TO 11
   13 AMUL=AMUL-PI
   11 TAN2(K)=TAN(K)+AMUL
    5 CONTINUE
      TERM=0.
      DO 20 I=1,KR
      ALPHA=I
   20 TERM=TERM+ALPHA*ALPHA
      TERM=TERM*2.0
      K=0
      X=0.
      DO 21 I=1,NDATA
      R=0.
      DO 22 J=1,KR
      ALPHA=J
      IPJ=I+J
      IMJ=I-J
      IF(IMJ) 22,33,33
   33 ITEM=NDATA-IPJ
      IF(ITEM) 22,32,32
   32 R=R+ALPHA*TAN2(IPJ)-ALPHA*TAN2(IMJ)
   22 CONTINUE
      X=X+DX
      STAN=R/TERM
      DTAN(I)=STAN*COF
C
C     TAN2=PHASES CORRECTED FOR DISCONTINUITIES
C     STAN=UNCORRECTED STRAINS
C     DTAN=STRAINS
C
   21 WRITE OUTPUT TAPE 6,3,X,TAN(I),TAN2(I),STAN,DTAN(I)
C
C     DTR=DTAN REDUCED IN NUMBER FOR PLOTTING, ALWAYS 100
C     VALUES
C     TR=TAN2 REDUCED AS ABOVE
C     A=DUMMY VARIABLE FOR PLOTTING DIMENSION 100
C
      J=0
      DO 4 I=1,100
      J=J+NT
      DTR(I)=DTAN(J)
    4 TR(I)=TAN2(J)
      CALL RPLT(TR,100,A)
      CALL RPLT(DTR,100,A)
      RETURN
      END
```

```
C       SUBROUTINE DIFTN USING LANCZOS FORMULA FOR
C       DIFFERENTIATION WITH FUNCTION REFLECTED W.R.T. END
C       POINTS
C       PROGRAM CORRECTS FOR CYCLIC DISCONTINUITY OF THE ARC
C       TANGENT FUNCTION
C
C       TAN=PHASES GENERATED BY FILTER
C       NDATA=RDATA=NUMBER OF DATA POINTS
C       DTAN=STRAINS
C       TAN2=PHASES CORRECTED FOR DISCONTINUITIES
C       DTR=DTAN REDUCED IN NUMBER FOR PLOTTING, ALWAYS 100
C       VALUES
C       TR=TAN2 REDUCED AS ABOVE
C       A=DUMMY VARIABLE FOR PLOTTING DIMENSION 100
C
        SUBROUTINE DIFTN(TAN,NDATA,DTAN,TAN2,DTR,A,TR)
      1 FORMAT(I4)
      2 FORMAT(6E12.0)
      3 FORMAT(5E20.5)
      6 FORMAT(2F10.0)
     41 FORMAT(1H1,//,10X,26H RDATA,FRING,WIDTH,DX,COF=,5E18.5
                                          )
     42 FORMAT(12A6)
     43 FORMAT(/,10X,12A6)
     40 FORMAT(///,18X,2H X,16X,4H TAN,15X,5H TAN2,15X,5H DTAN
                                          ,
       $12X,8H STRAINS)
        DIMENSION DTAN(4000),DTR(100)
        DIMENSION TAN(4000),TAN2(4000),A(100),TR(100)
C
C       KR=NUMBER OF POINTS IN POLYNOMIAL APPROXIMATION IN THE
C       NEIGHBORHOOD OF THE POINT WHERE THE DERIVATIVE IS
C       SOUGHT
C       FRING=NUMBER OF LINES PER INCH OF THE MASTER
C       WIDTH=LENGTH OF THE MODEL IN THE DIRECTION OF SCAN
C
        READ INPUT TAPE 5,1,KR
        READ INPUT TAPE 5,6,FRING,WIDTH
        PI=3.1416
        NT=NDATA/100
        RDATA=NDATA
        DX=WIDTH/RDATA
        COF=1.0/(2.0*FRING*PI*DX)
        WRITE OUTPUT TAPE 6,41,RDATA,FRING,WIDTH,DX,COF
        WRITE OUTPUT TAPE 6,40
        AMUL=0.
        DO 5 K=1,NDATA
        A1=TAN(K)-TAN(K-1)
        A1=SIGNF(2.,A1)
        A2=TAN(K-1)-TAN(K-2)
        A2=SIGNF(1.,A2)
        A3=SIGNF(4.,TAN(K))
        A4=SIGNF(3.,TAN(K-1))
        AA=(A1+A2+A3+A4)
```

```
      AA2=ABSF(AA)
      IF(AA2-3.0) 10,11,11
   10 IF(AA) 12,11,13
   12 AMUL=AMUL+PI
      GO TO 11
   13 AMUL=AMUL-PI
   11 TAN2(K)=TAN(K)+AMUL
    5 CONTINUE
      TERM=0.
      DO 20 I=1,KR
      ALPHA=I
   20 TERM=TERM+ALPHA*ALPHA
      TERM=TERM*2.0
      X=0.
      DO 21 I=1,NDATA
      R=0.
      DO 22 J=1,KR
      ALPHA=J
      IPJ=I+J
      IMJ=I-J
      IF(IMJ) 31,33,33
   31 IMJ=-IMJ
   33 ITEM=NDATA-IPJ
      IF(ITEM) 32,22,22
   32 IPJ=NDATA+ITEM
   22 R=R+ALPHA*TAN2(IPJ)-ALPHA*TAN2(IMJ)
      X=X+DX
      STAN=R/TERM
      DTAN(I)=STAN*COF
C
C     STAN=UNCORRECTED STRAINS
C
   21 WRITE OUTPUT TAPE 6,3,X,TAN(I),TAN2(I),STAN,DTAN(I)
      J=0
      DO 4 I=1,100
      J=J+NT
      DTR(I)=DTAN(J)
    4 TR(I)=TAN2(J)
      CALL RPLT(TR,100,A)
      CALL RPLT(DTR,100,A)
      CALL EXIT
      RETURN
      END
```

107

```
C         SUBROUTINE DIFTN USING LANCZOS FORMULA FOR
C         DIFFERENTIATION WITH WEIGHTS CHANGED TO ZERO BEYOND
C         END POINTS
C         PROGRAM CORRECTS FOR CYCLIC DISCONTINUITY OF THE ARC
C         TANGENT FUNCTION
C
C         TAN=PHASES GENERATED BY FILTER
C         NDATA=RDATA=NUMBER OF DATA POINTS
C         DTAN=STRAINS
C         TAN2=PHASES CORRECTED FOR DISCONTINUITIES
C         DTR=DTAN REDUCED IN NUMBER FOR PLOTTING, ALWAYS 100
C         VALUES
C         TR=TAN2 REDUCED AS ABOVE
C         A=DUMMY VARIABLE FOR PLOTTING DIMENSION 100
C
          SUBROUTINE DIFTN(TAN,NDATA,DTAN,TAN2,DTR,A,TR)
        1 FORMAT(I4)
        2 FORMAT(6E12.0)
        3 FORMAT(5E20.5)
        6 FORMAT(2F10.0)
       41 FORMAT(1H1,//,10X,26H RDATA,FRING,WIDTH,DX,COF=,5E18.5
                                           )
       42 FORMAT(12A6)
       43 FORMAT(/,10X,12A6)
       40 FORMAT(///,18X,2H X,16X,4H TAN,15X,5H TAN2,15X,5H DTAN
                                           ,
         $12X,8H STRAINS)
          DIMENSION DTAN(4000),DTR(100)
          DIMENSION TAN(4000),TAN2(4000),A(100),TR(100)
C
C         KR=NUMBER OF POINTS IN POLYNOMIAL APPROXIMATION IN THE
C         NEIGHBORHOOD OF THE POINT WHERE THE DERIVATIVE IS
C         SOUGHT
C         FRING=NUMBER OF LINES PER INCH OF THE MASTER
C         WIDTH=LENGTH OF THE MODEL IN THE DIRECTION OF SCAN
C
          READ INPUT TAPE 5,1,KR
          READ INPUT TAPE 5,6,FRING,WIDTH
          PI=3.1416
          NT=NDATA/100
          RDATA=NDATA
          DX=WIDTH/RDATA
          COF=1.0/(2.0*FRING*PI*DX)
          WRITE OUTPUT TAPE 6,41,RDATA,FRING,WIDTH,DX,COF
          WRITE OUTPUT TAPE 6,40
          AMUL=0.
          DO 5 K=1,NDATA
          A1=TAN(K)-TAN(K-1)
          A1=SIGNF(2.,A1)
          A2=TAN(K-1)-TAN(K-2)
          A2=SIGNF(1.,A2)
          A3=SIGNF(4.,TAN(K))
          A4=SIGNF(3.,TAN(K-1))
          AA=(A1+A2+A3+A4)
```

```
      AA2=ABSF(AA)
      IF(AA2-3.0) 10,11,11
   10 IF(AA) 12,11,13
   12 AMUL=AMUL+PI
      GO TO 11
   13 AMUL=AMUL-PI
   11 TAN2(K)=TAN(K)+AMUL
    5 CONTINUE
      TERM=0.
      DO 20 I=1,KR
      ALPHA=I
   20 TERM=TERM+ALPHA*ALPHA
      TERM=TERM*2.0
      X=0.
      DO 21 I=1,NDATA
      R=0.
      DO 22 J=1,KR
      ALPHA=J
      IPJ=I+J
      IMJ=I-J
      IF(IMJ) 22,33,33
   33 ITEM=NDATA-IPJ
      IF(ITEM) 22,32,32
   32 R=R+ALPHA*TAN2(IPJ)-ALPHA*TAN2(IMJ)
   22 CONTINUE
      X=X+DX
      STAN=R/TERM
      DTAN(I)=STAN*COF
C
C     STAN=UNCORRECTED STRAINS
C
   21 WRITE OUTPUT TAPE 6,3,X,TAN(I),TAN2(I),STAN,DTAN(I)
      J=0
      DO 4 I=1,100
      J=J+NT
      DTR(I)=DTAN(J)
    4 TR(I)=TAN2(J)
      CALL RPLT(TR,100,A)
      CALL RPLT(DTR,100,A)
      RETURN
      END
```

```
C        SUBROUTINE POUT PUNCHES DATA GENERATED BY PROGRAMS
C-       POINT=DATA TO BE PLOTTED
C        N=NUMBER OF DATA POINTS TO BE PLOTTED
C
         SUBROUTINE POUT(POINT,N)
         DIMENSION POINT(1)
         J=N/6
         JO=1
         DO 1 I=1,J
         JE=JO+5
         WRITE OUTPUT TAPE 6,2,(POINT(JT),JT=JO,JE)
       1 JO=JE+1
         WRITE OUTPUT TAPE 6,2,(POINT(JT),JT=JO,N)
       2 FORMAT(1HP,6E12.5)
         RETURN
         END
```

```
C       SUBROUTINE RPLT PLOTS DATA GENERATED BY PROGRAMS
C       POINT=DATA TO BE PLOTTED
C       N=NUMBER OF DATA POINTS TO BE PLOTTED
C       A=DUMMY VARIABLE FOR PLOT DIMENSION 100
C
        SUBROUTINE RPLT(POINT,N,A)
        DIMENSION POINT(1),A(1)
        B=1H
        X=1HX
        DO 6 I=1,100
      6 A(I)=B
        GP=POINT(1)
        GN=POINT(1)
        DO 2 I=1,N
        IF(POINT(I)-GP) 3,2,4
      4 GP=POINT(I)
        GO TO 2
      3 IF(POINT(I)-GN) 5,2,2
      5 GN=POINT(I)
      2 CONTINUE
        R=998./(GP-GN)
        NS=-GN*R+1.
        WRITE OUTPUT TAPE 6,8,R,GP,GN,NS
      8 FORMAT(10H1RATIO IS,E14.7,13H  MAXIMUM IS,E14.7,
       $13H   MINIMUM IS
       1E14.7,17H  SCALED ZERO IS,I4,//)
        DO 9 I=1,N
        IOT=(POINT(I)-GN)*R+1.0
        J=(IOT/10)+1
        A(J)=X
        WRITE OUTPUT TAPE 6,11,IOT,(A(K),K=1,100)
     11 FORMAT(1X,I4,5X,100A1)
      9 A(J)=B
        RETURN
        END
```

APPENDIX D

FIGURES
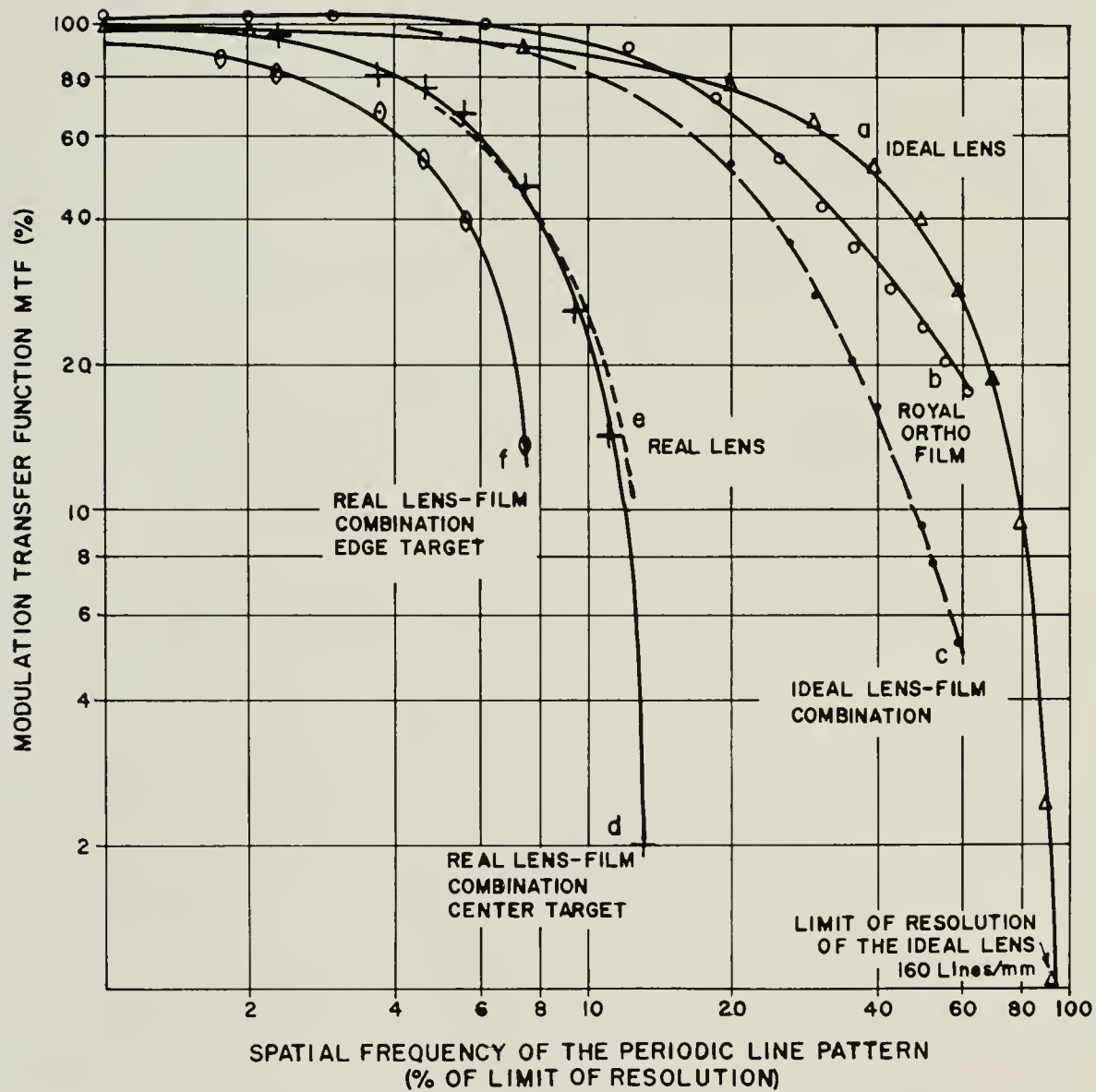
Fig. 1 Modulation Transfer Function Measurement

Fig. 2 H & D Characteristic Curve of a Film

SENSITOMETRIC
CHARACTERISTIC CURVE
OF A NEGATIVE ASSUMING
D=LOG E

TRANSMITTANCE VARIATION OF THE
FILM RECORD OF A MOIRE FRINGE
EXPOSURE WITHIN THE STRAIGHT
LINE PORTION OF THE H & D CURVE

TRANSMITTANCE

EXPOSURE

TRANSMITTANCE

POSITION COORDINATE X

POSITION COORDINATE X

SINUSOIDAL EXPOSURE

LIGHT INTENSITY
VARIATION OF A
MOIRE FRINGE
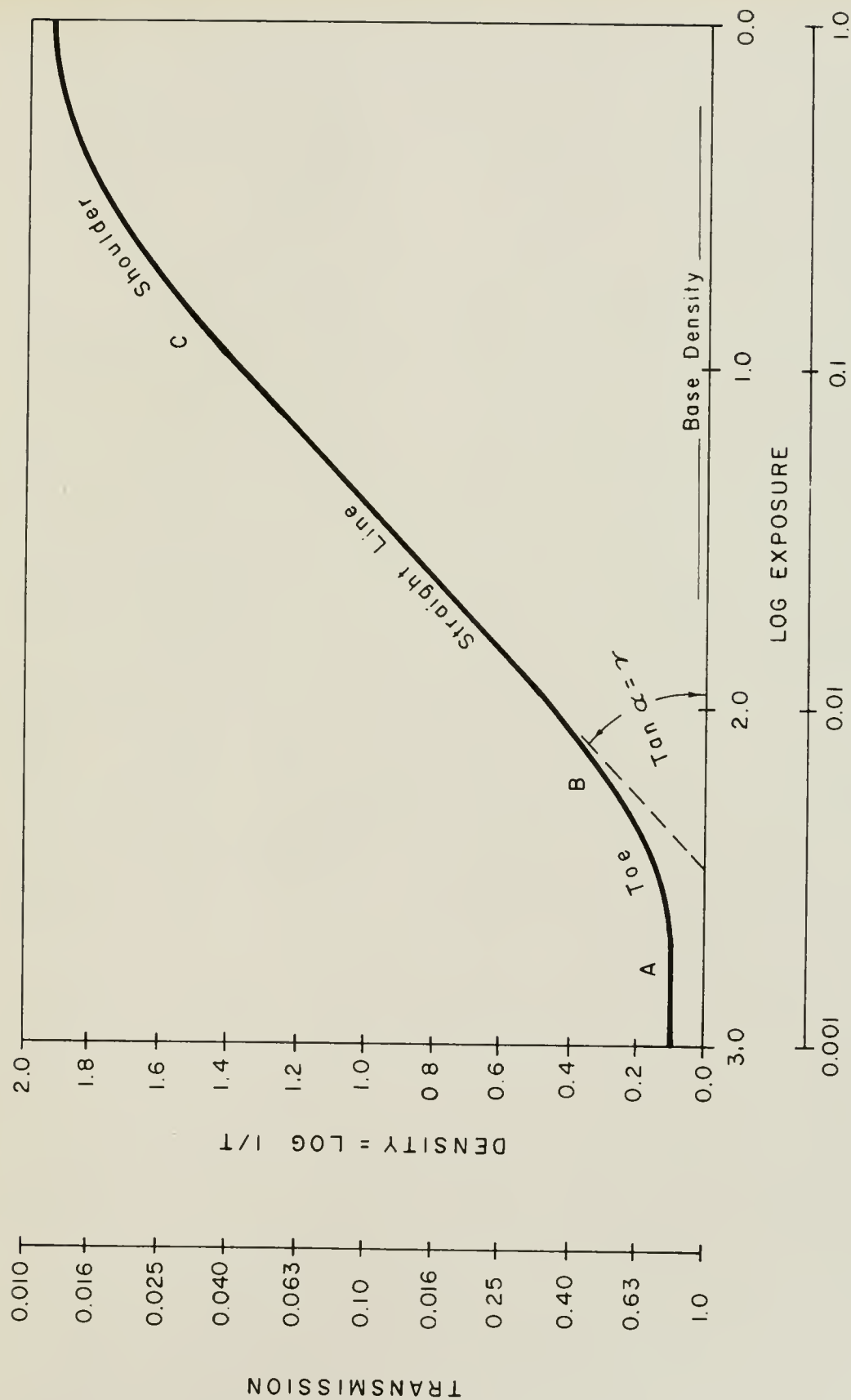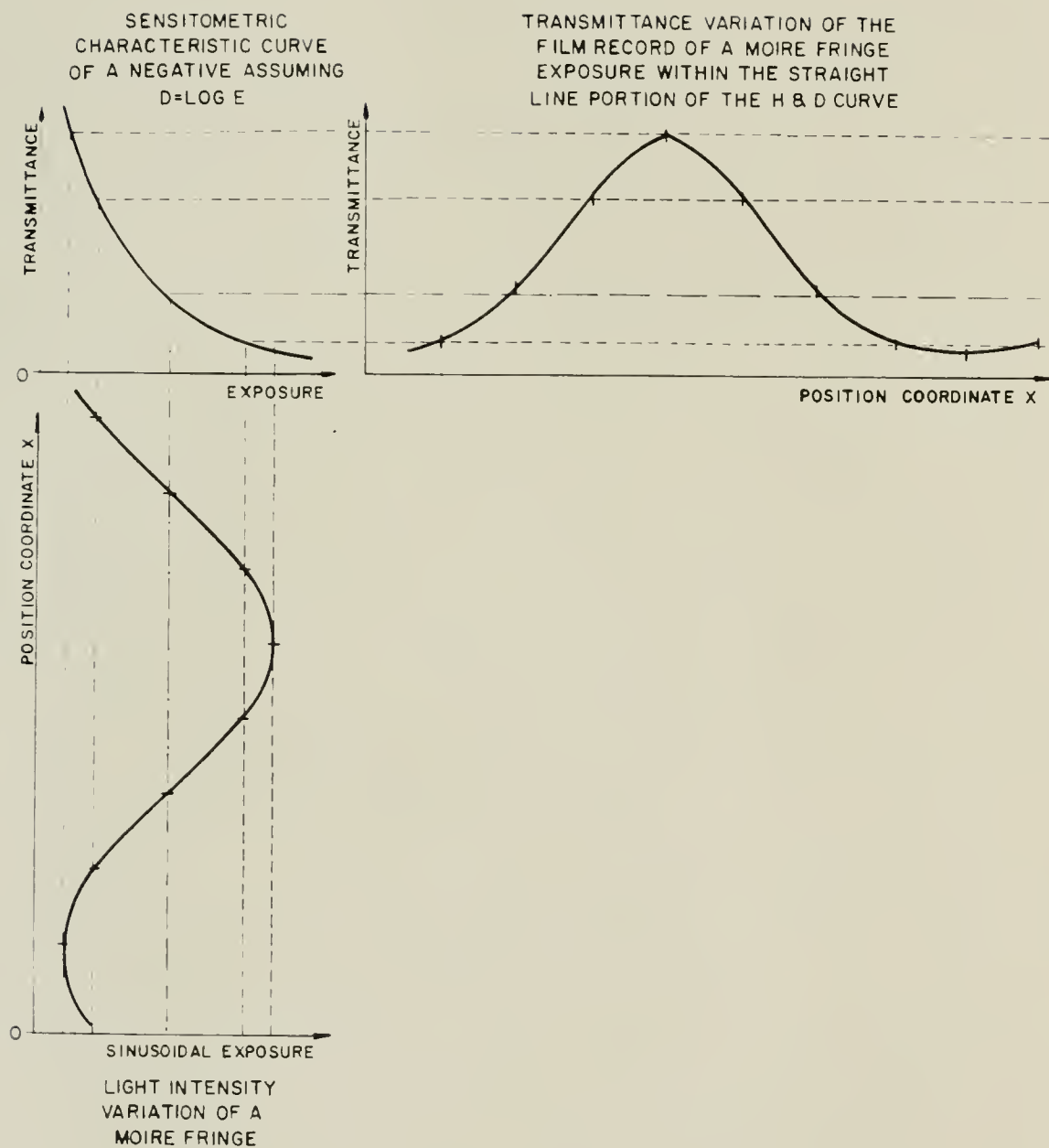
Fig. 3 Spatial Waveform Distortion Due to the Film
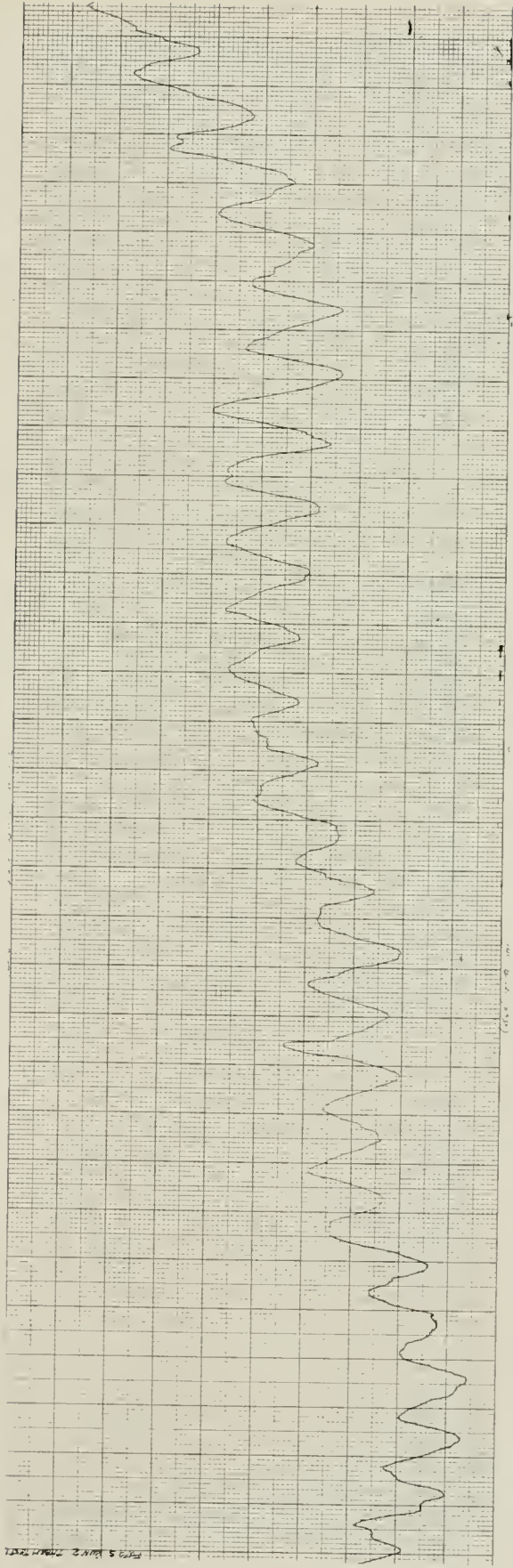
Fig. 4 Unfiltered Transmission Trace of a Sinusoidal Exposure
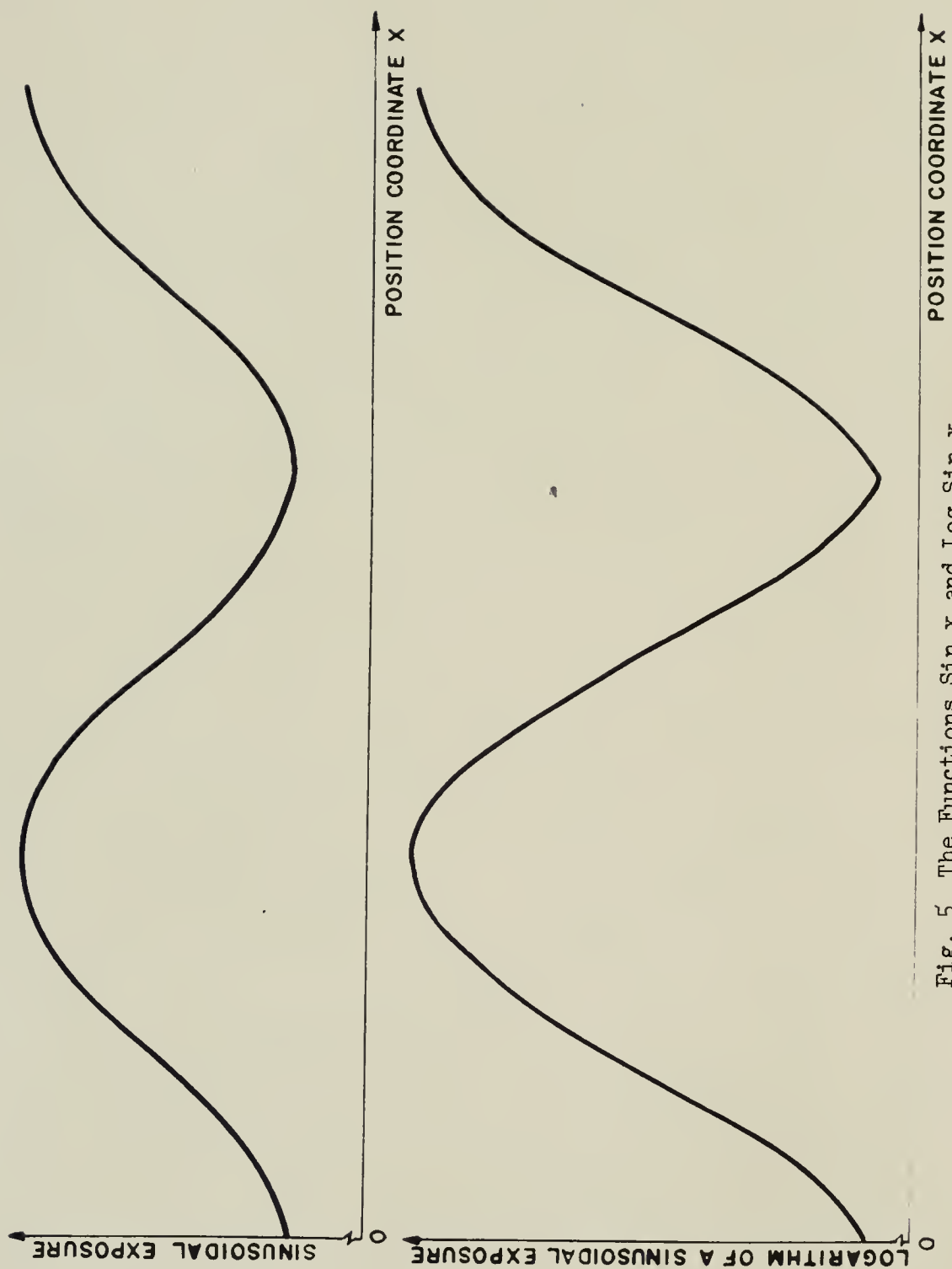
Fig. 5 The Functions Sin x and Log Sin x

117
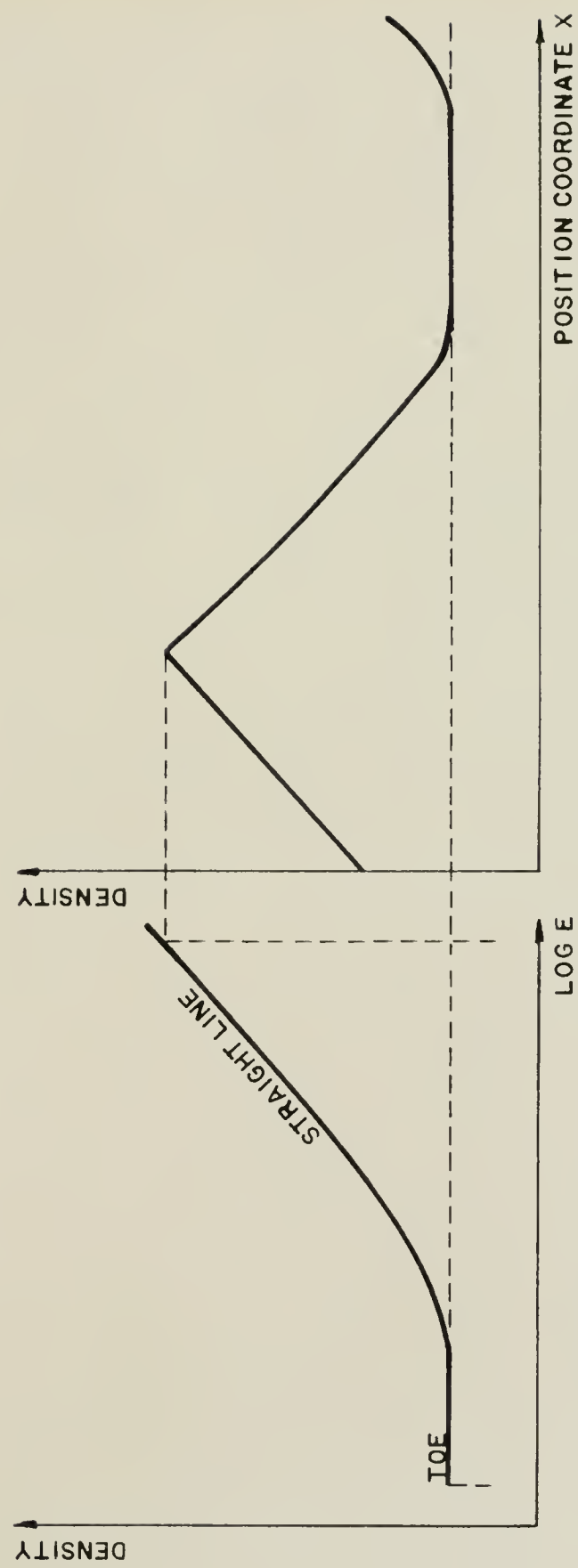
Fig. 6 Density Trace of a Sinusoidal Exposure in the Toe and
Straight Line Portion of the H & D Curve
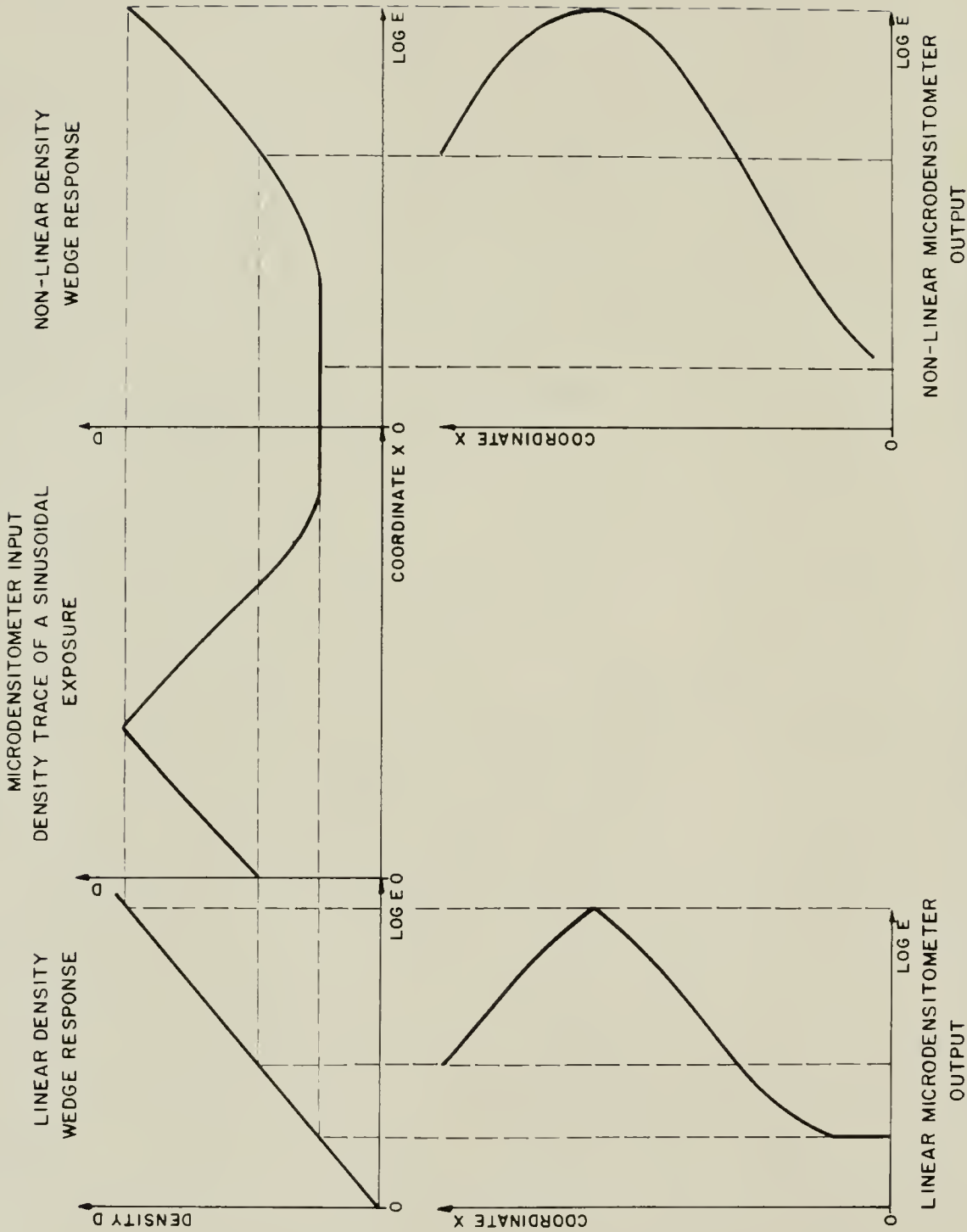
Fig. 7 Correction of Waveform Distortion by the Non-Linear Wedge Method
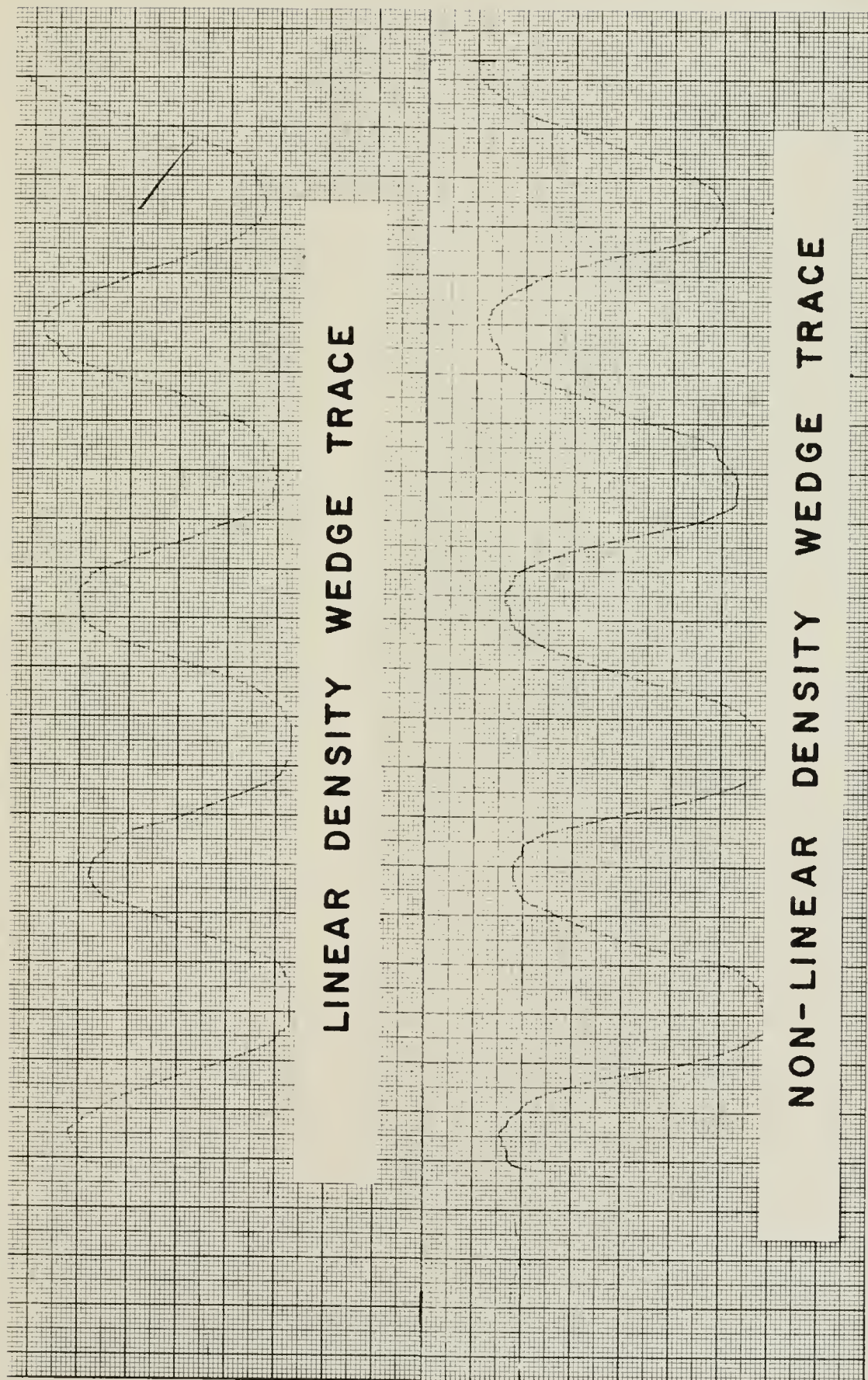
Fig. 8 Non-Linear Density Wedge Experiment

120
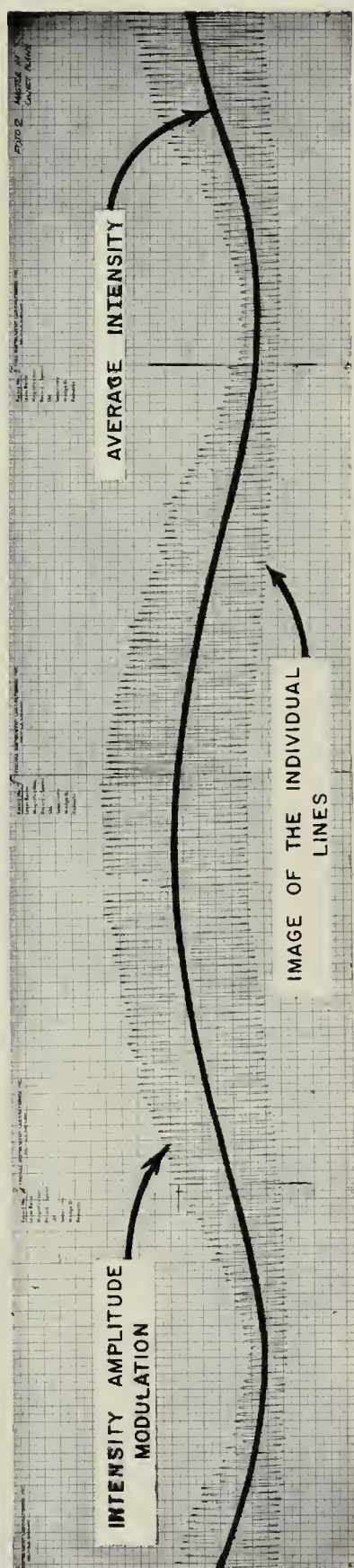
MASTER IN OBJECT PLANE
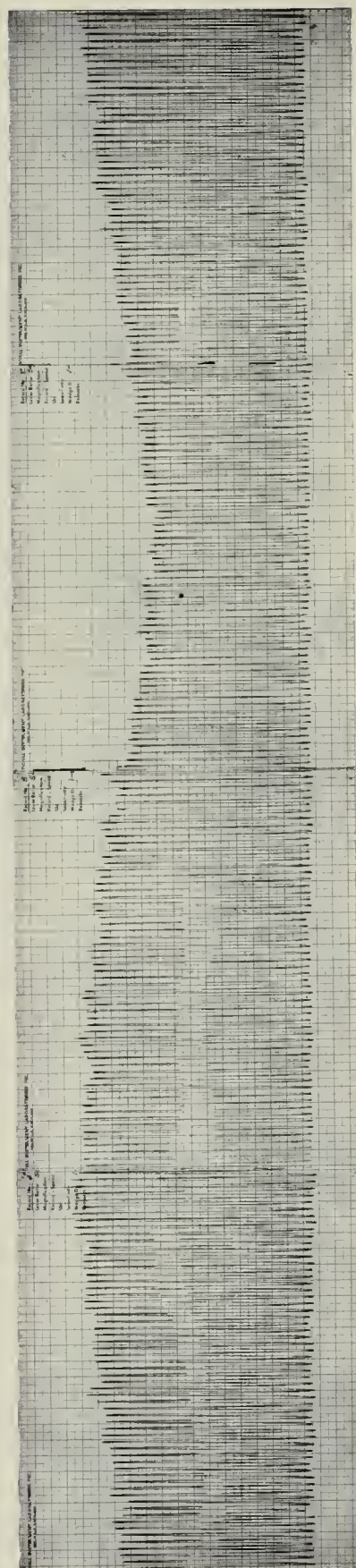
MASTER IN IMAGE PLANE

Fig. 9 Fine Structure of Moiré Fringes
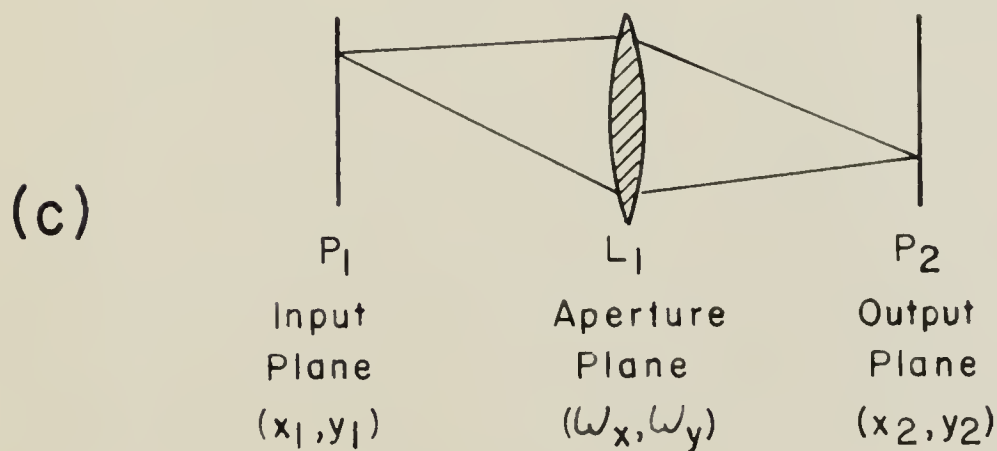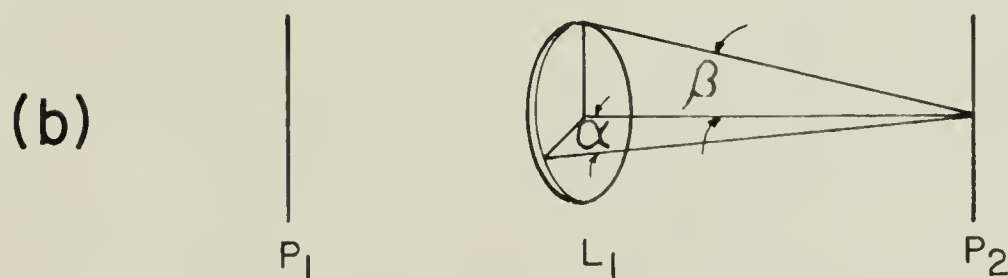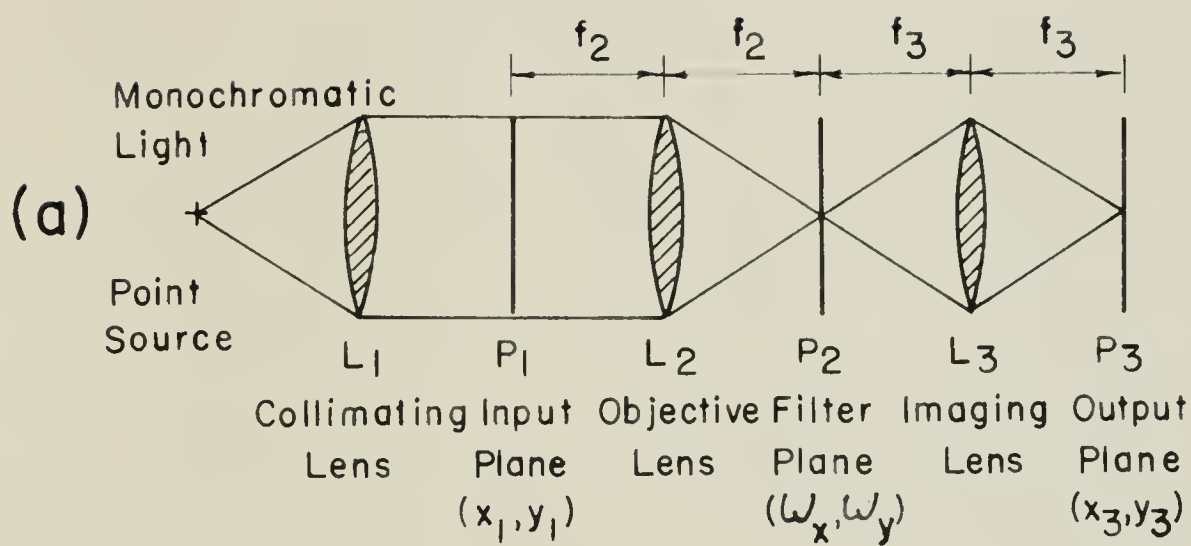
Fig. 10 Coherent and Incoherent Light Systems
a) Coherent, b) Coordinates, c) Incoherent
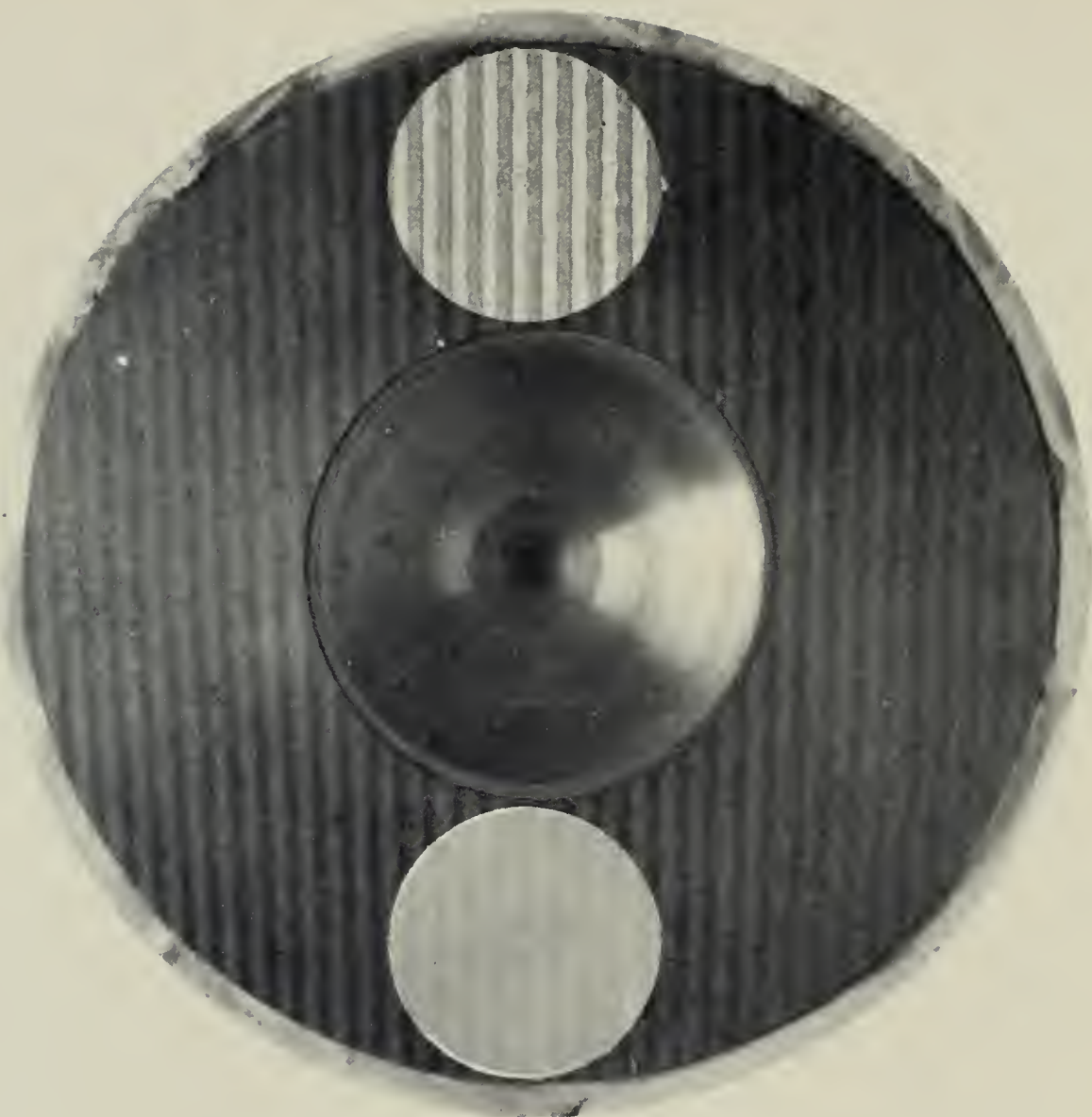
Fig. 11 Coherent Optical Filtering by Removal of the Bias Term
of the Grid. (Insert above: 50X magnification of the
master grid lines before filtering. Insert below:
50X magnification of the master grid lines after
filtering.)
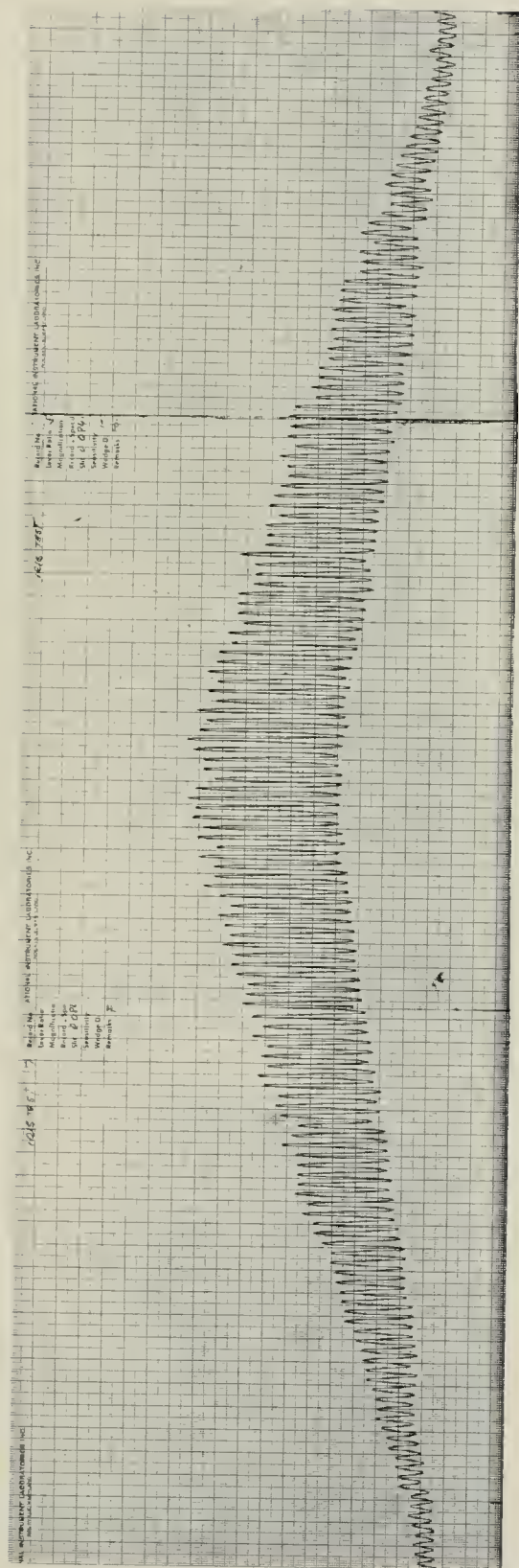
(a) Before Filtering
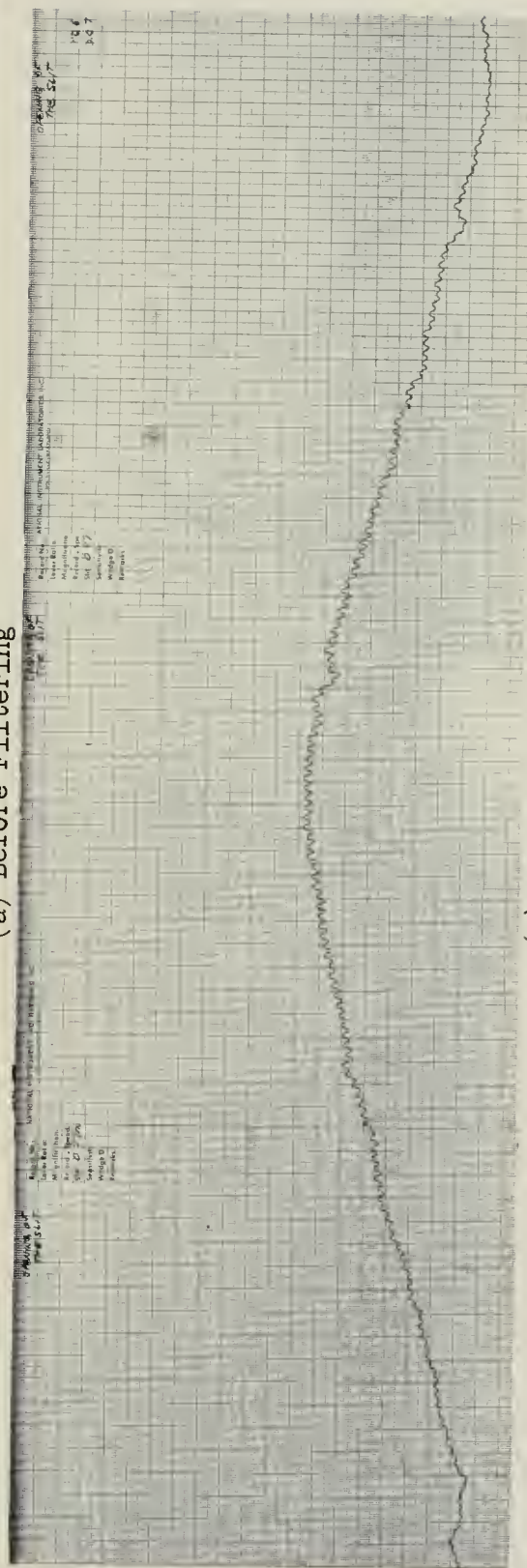
(b) After Filtering

Fig. 12 Incoherent Optical Filtering by Decreasing the Aperture of the Iris
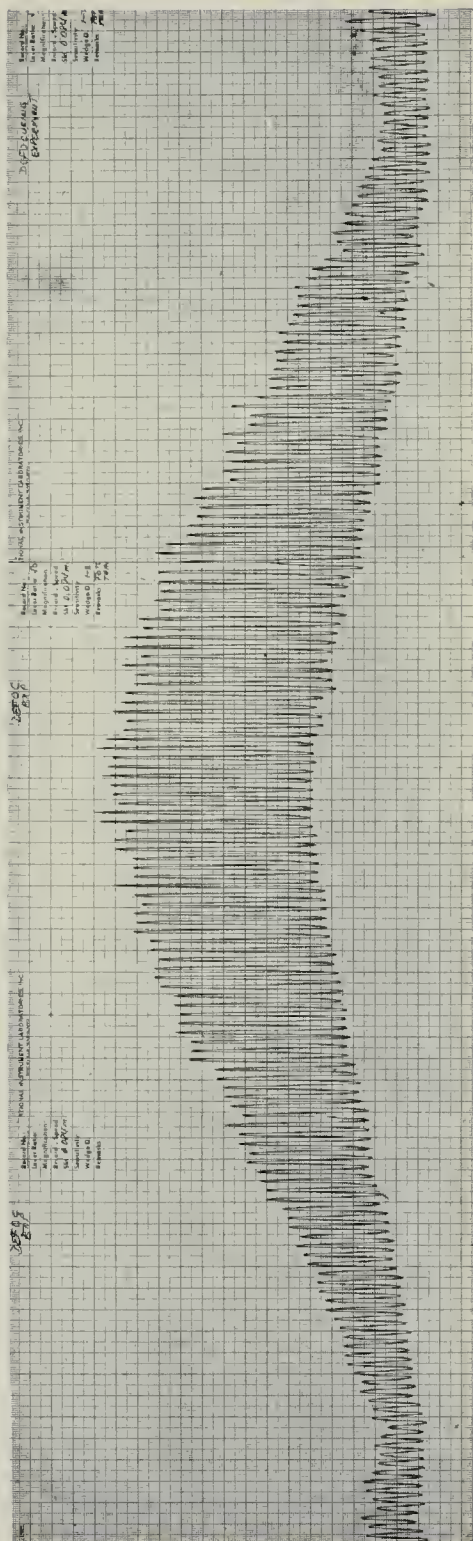
(a) Before Filtering
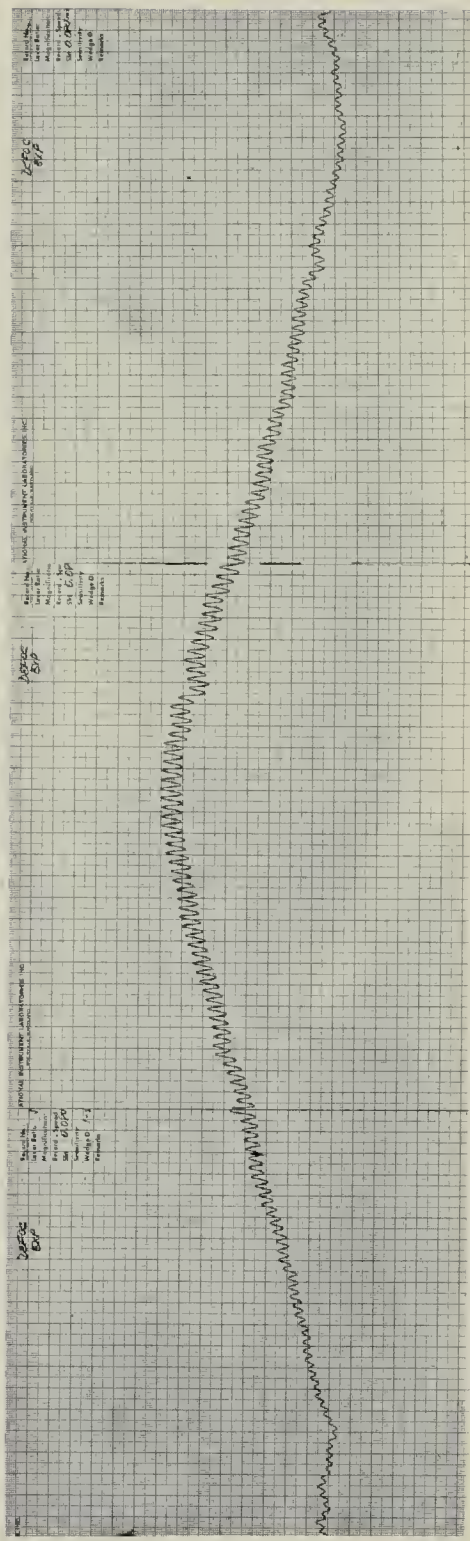
(b) After Filtering

Fig. 13 Incoherent Optical Filtering by Defocusing
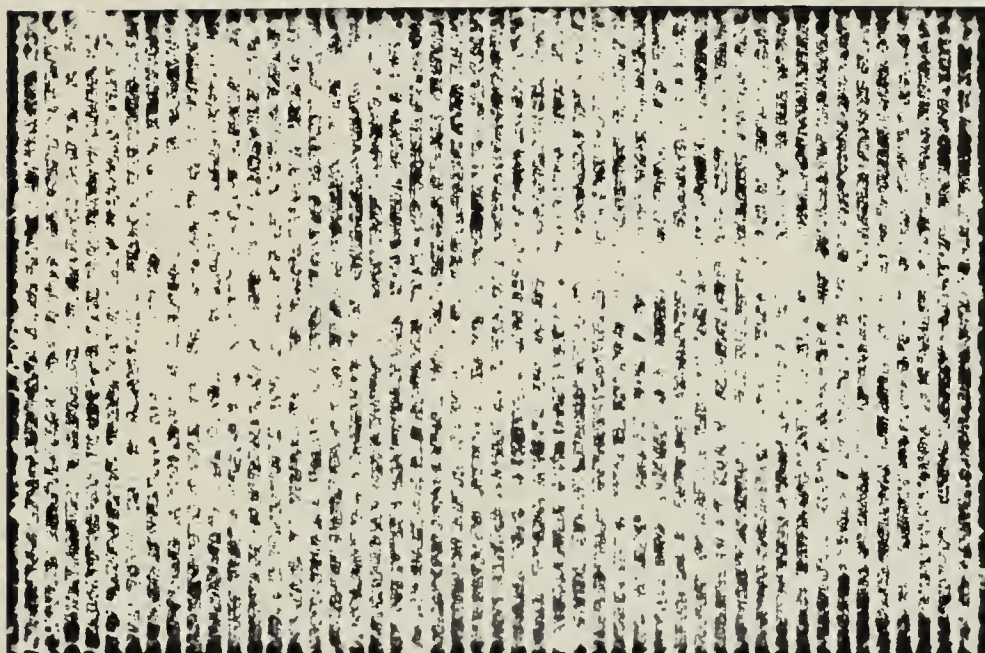
(a) Before Filtering

(b) After Filtering

Fig. 14   Incoherent Optical Filtering by Modification
of the Pupil Function with a Dirac Comb
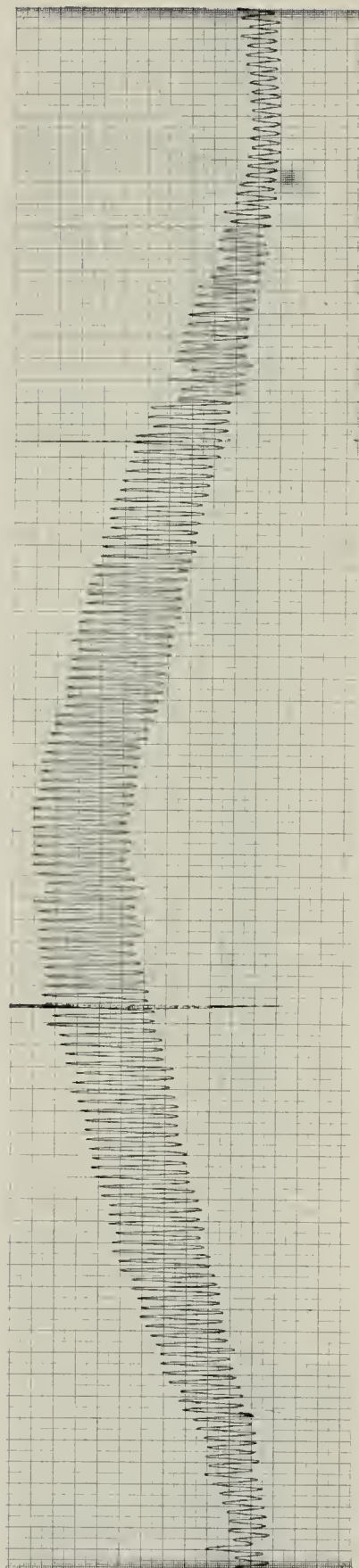
(a) Before Filtering
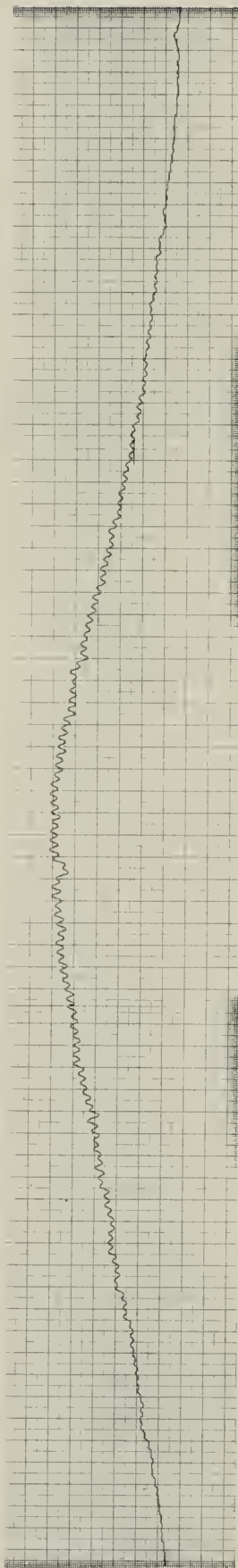
(b) After Filtering

Fig. 15 Incoherent Optical Filtering by Increasing
the Aperture of the Scanning Slit

127

Fig. 16 The Scanning Microdensitometer

Fig. 17   The Electro-Optical System
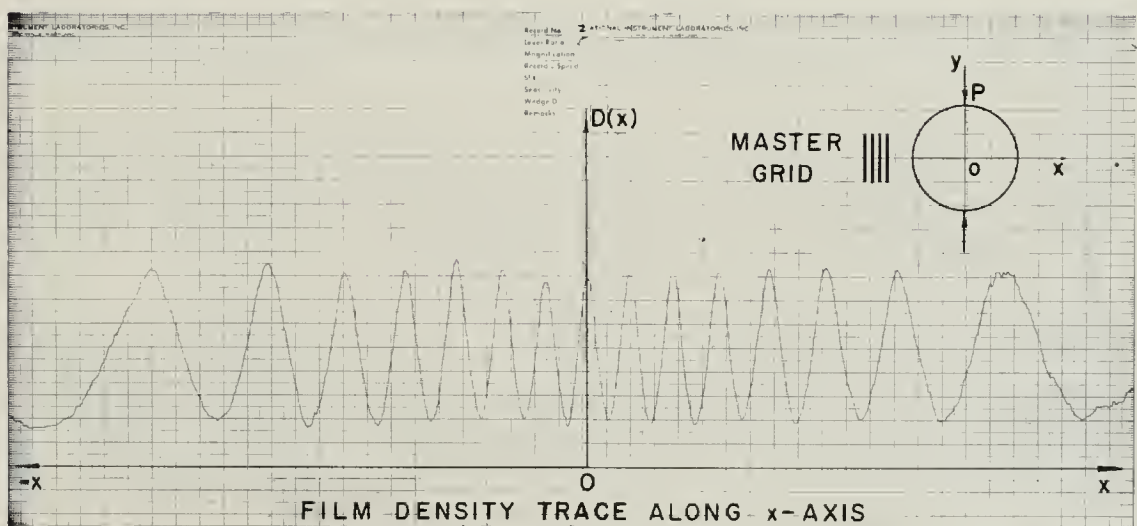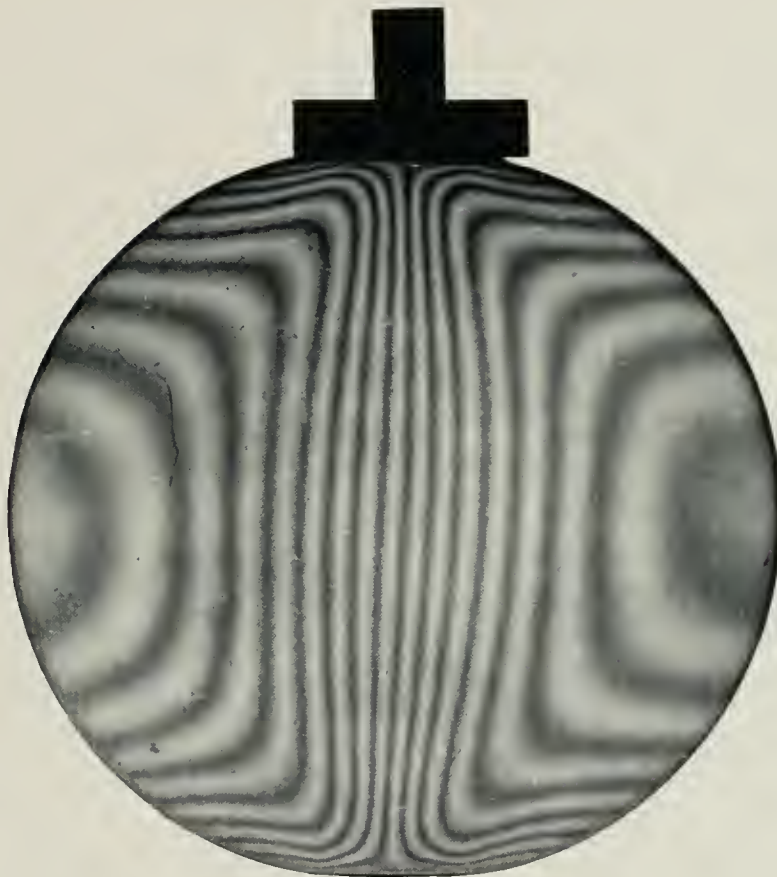
Fig. 18 Ring Under Diametral Compression
(Moiré of U)
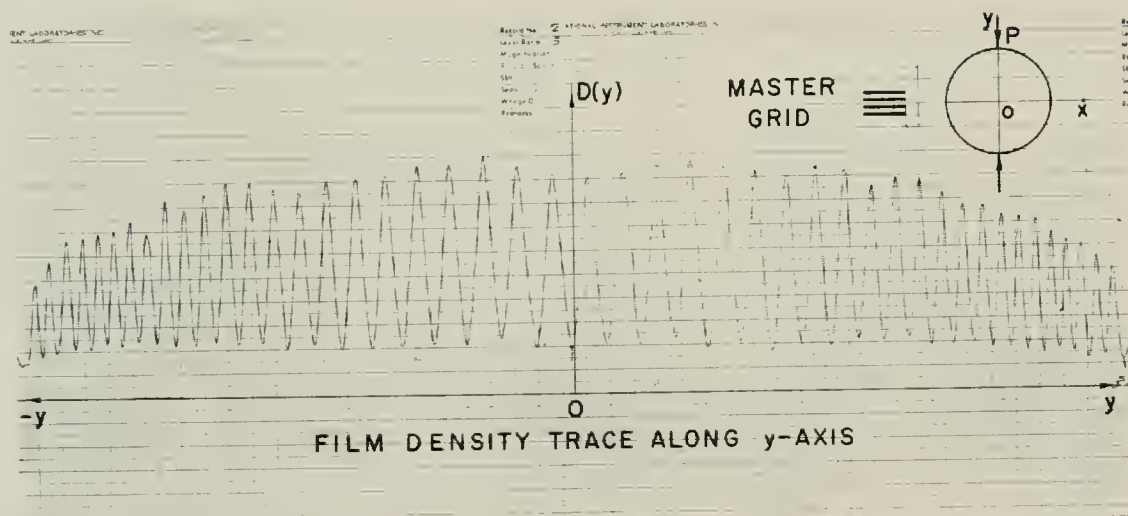
Fig. 19 Ring Under Diametral Compression
(Moiré of V)
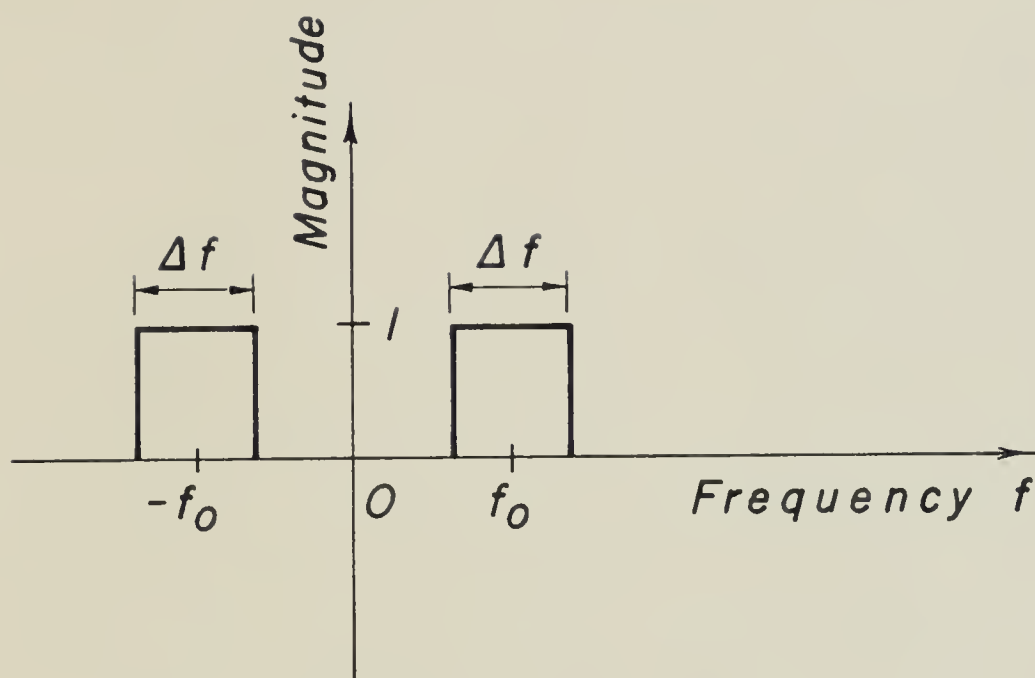
Transfer Function of In-Phase Filter
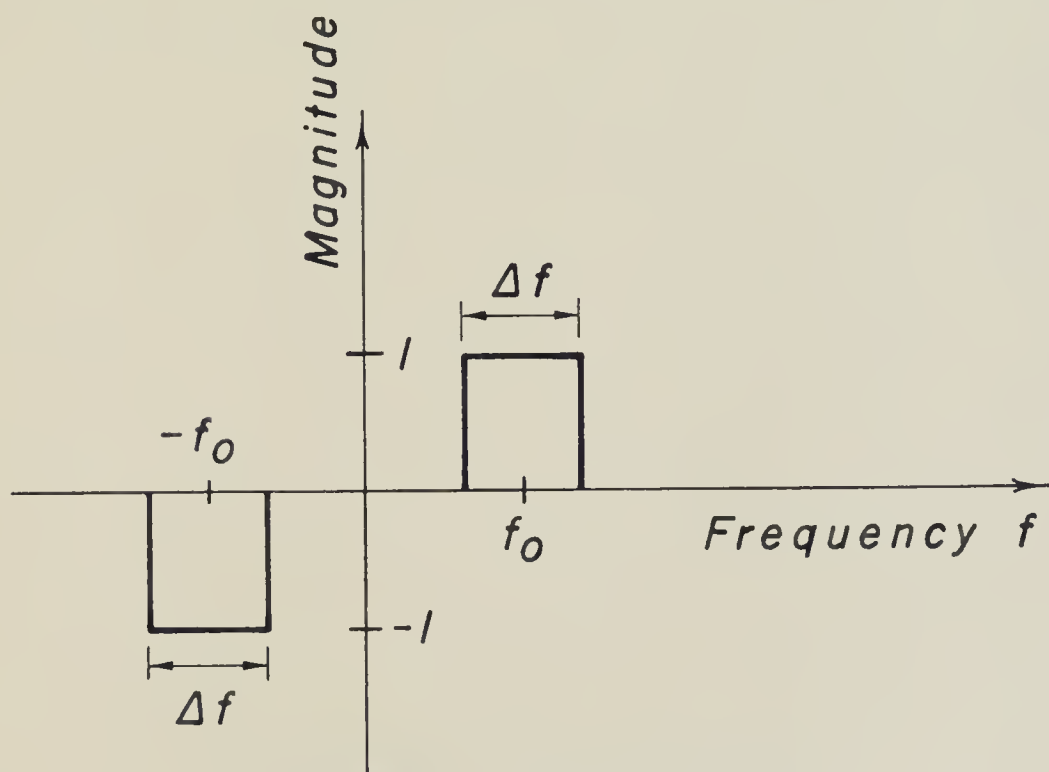
Transfer Function of In-Quadrature Filter

Fig. 20 Transfer Functions of Ideal Filters

132
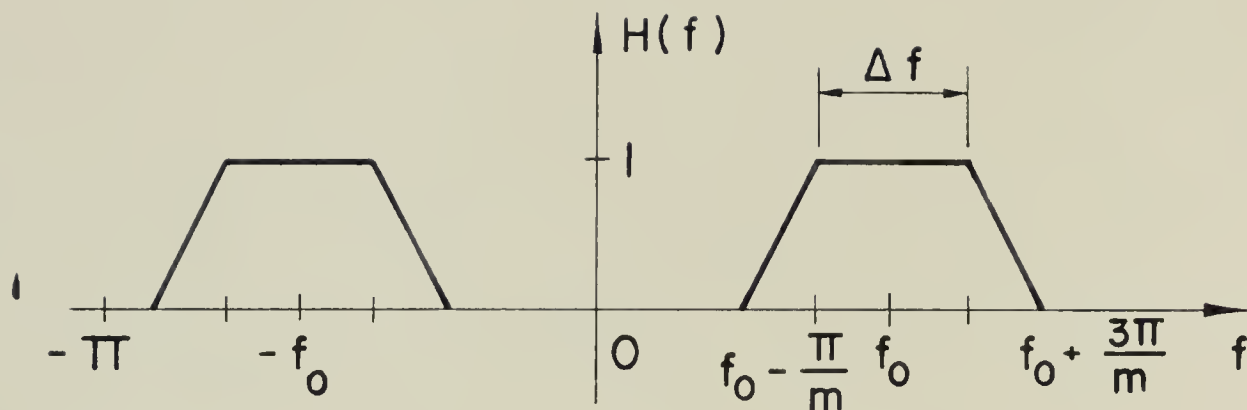
TRANSFER FUNCTION OF IN-PHASE FILTER

TRANFER FUNCTION OF IN-QUADRATURE FILTER

Fig. 21 Transfer Functions of a Combination of Tukey Filters
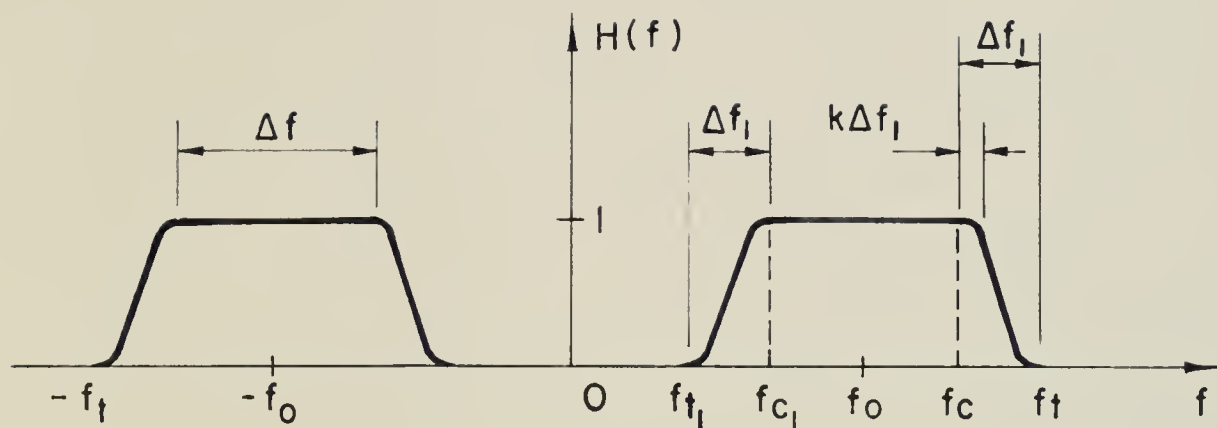
TRANSFER FUNCTION OF IN-PHASE FILTER
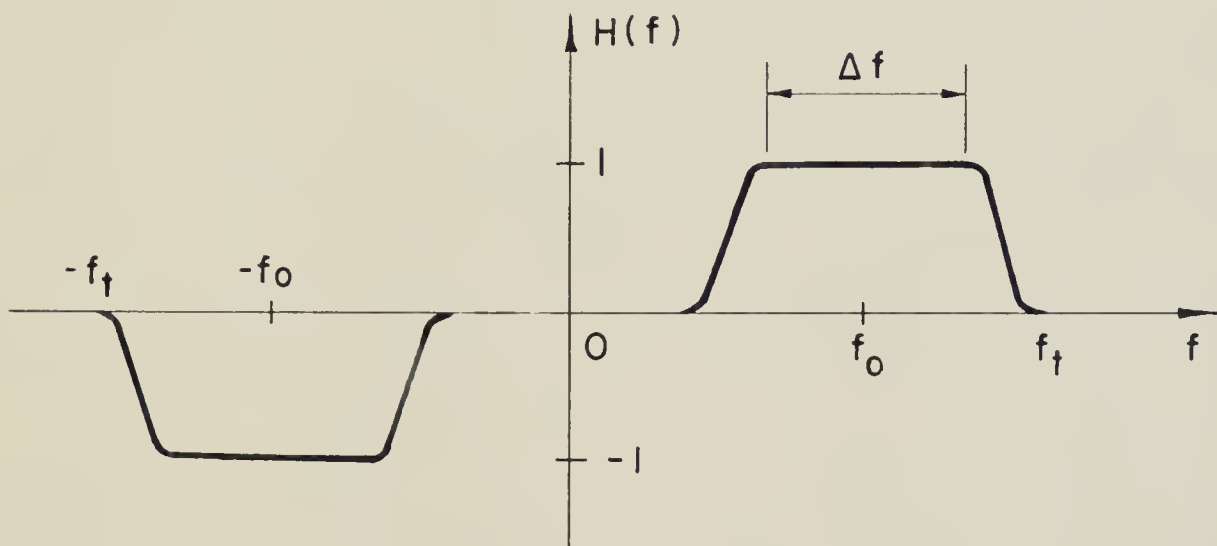
TRANSFER FUNCTION OF IN-QUADRATURE FILTER

Fig. 22 Transfer Functions of an Ormsby Filter
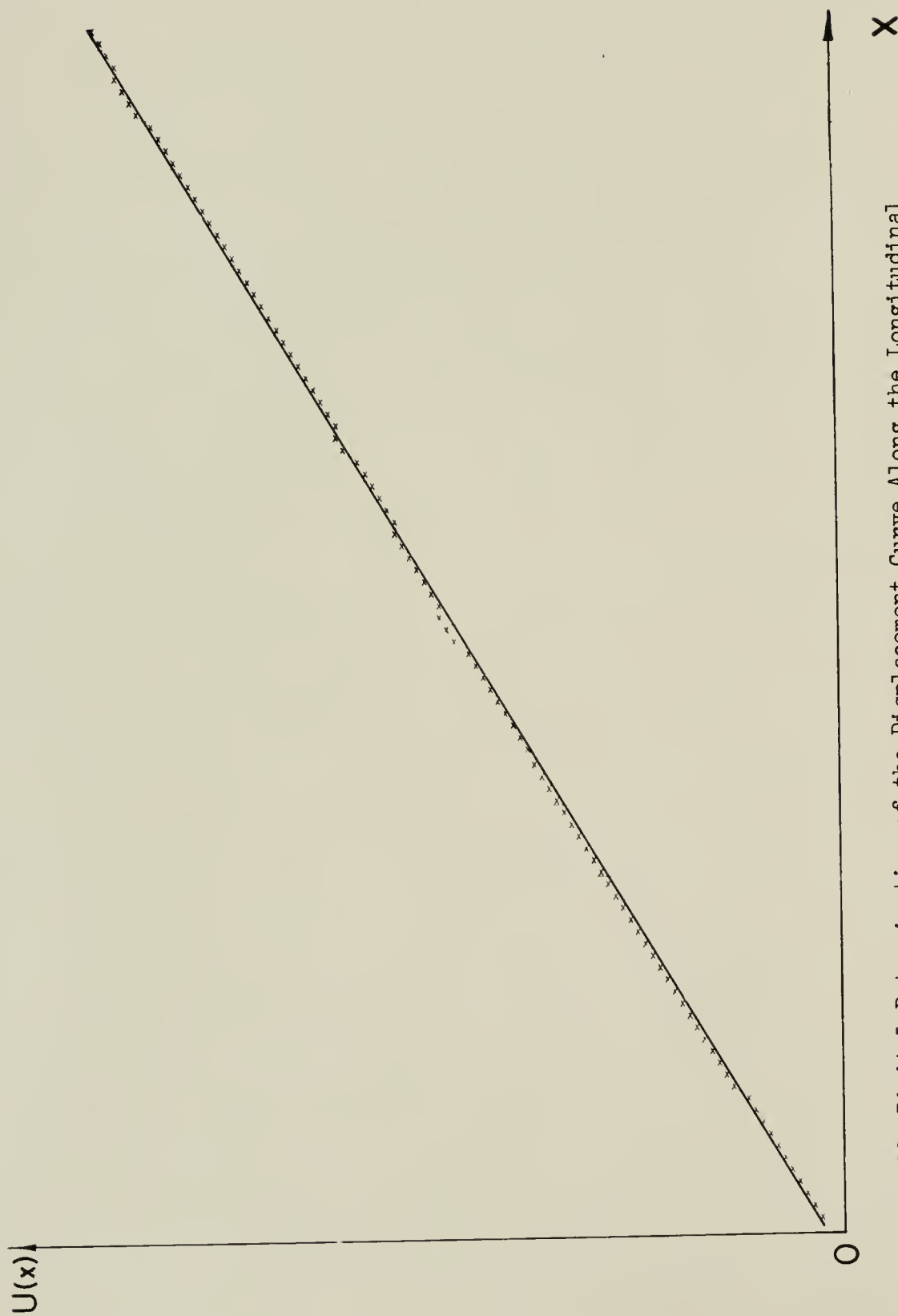
Fig. 23 Digital Determination of the Displacement Curve Along the Longitudinal Axis of a Traction Sample

135
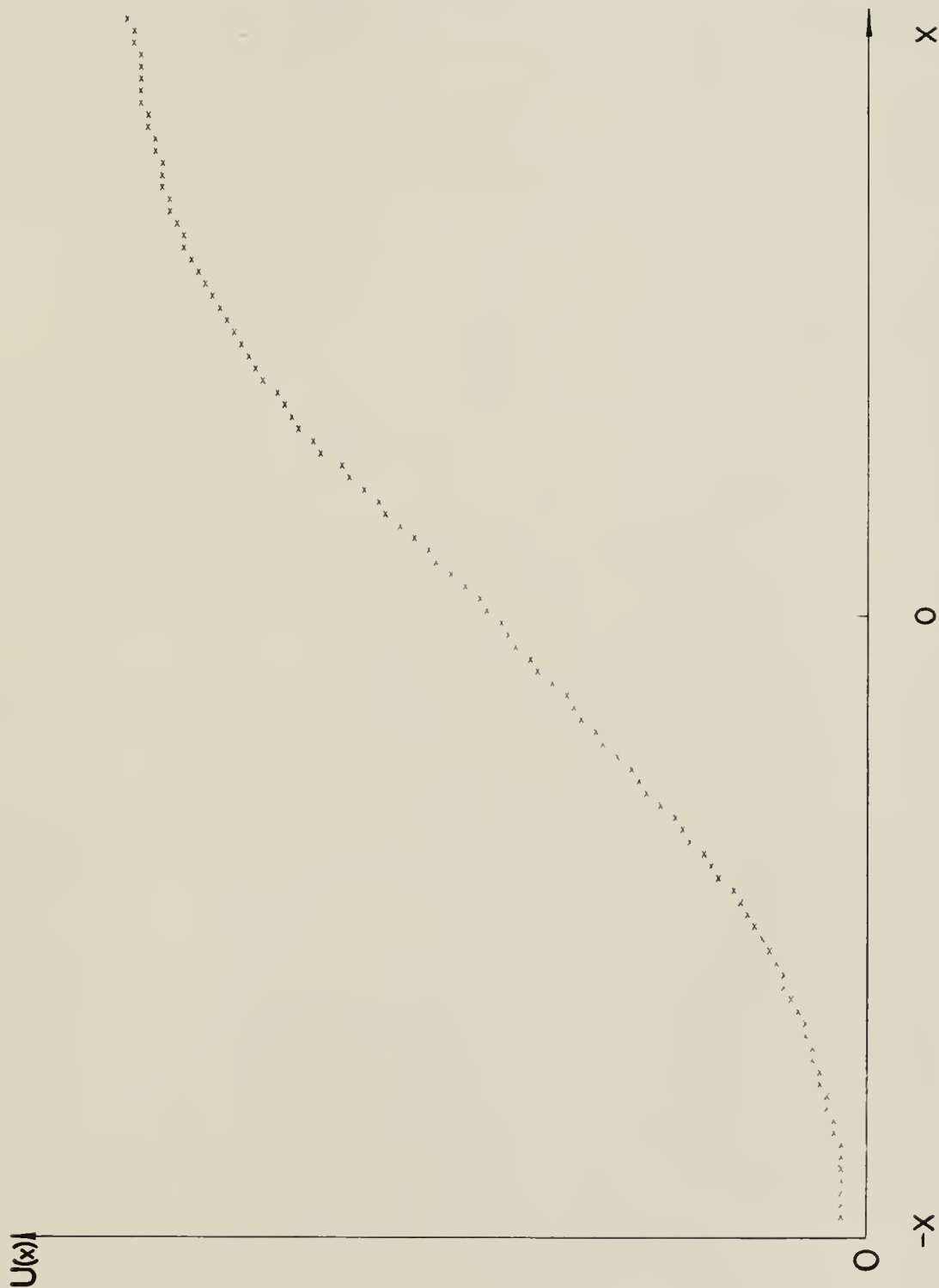
Fig. 24 Digital Determination of the Displacement Curve Along the
Horizontal Axis of the Disk
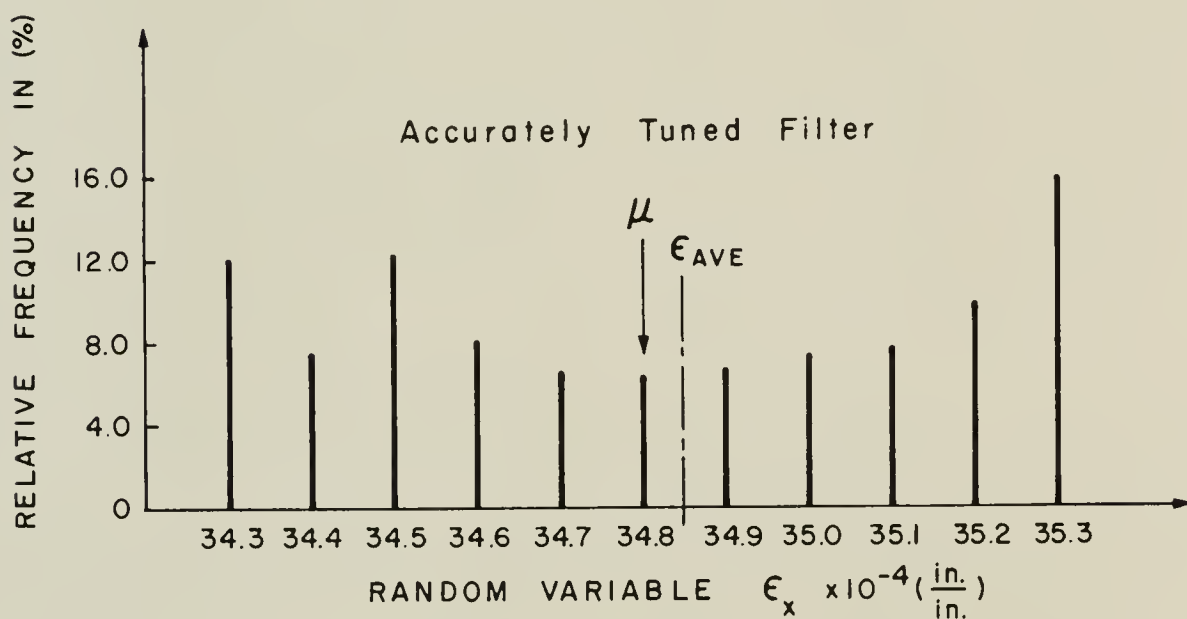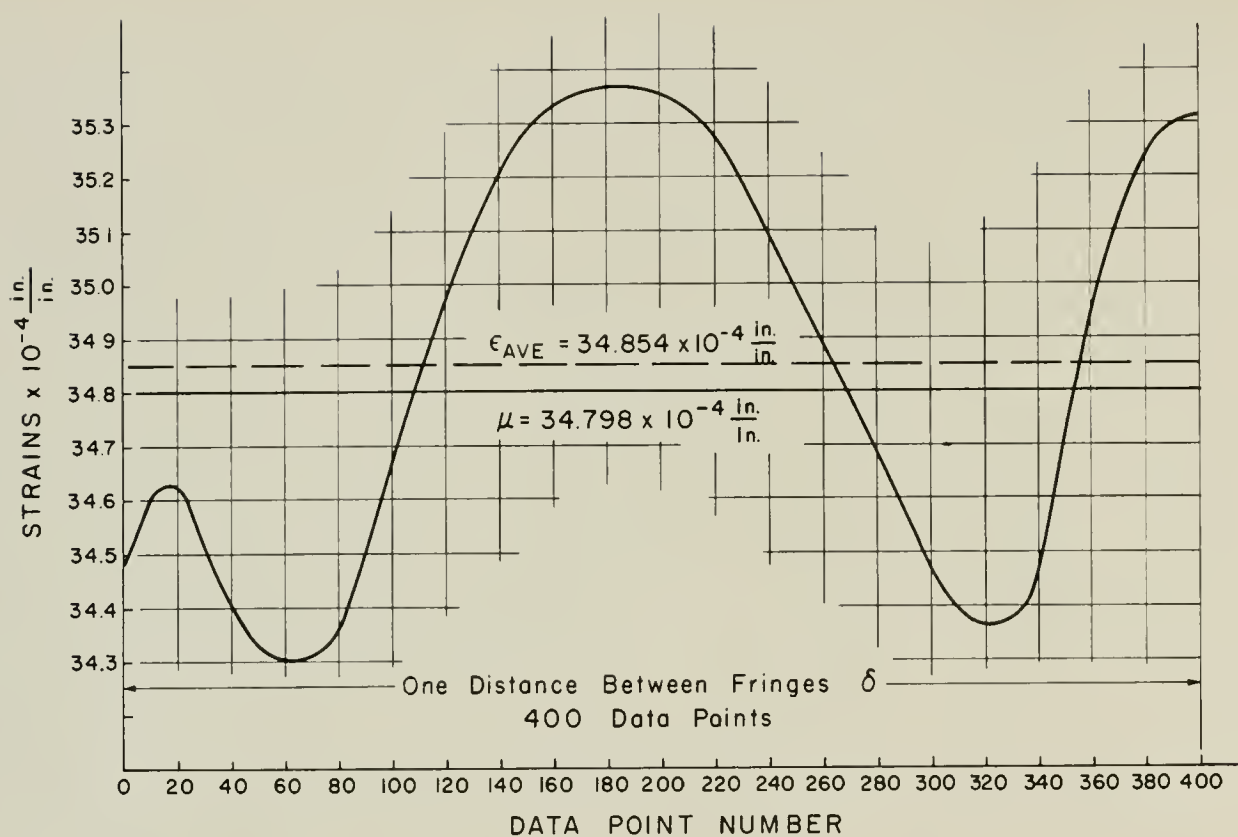
Fig. 25 Digital Determination of the Strains Between
Two Fringes in a Traction Sample
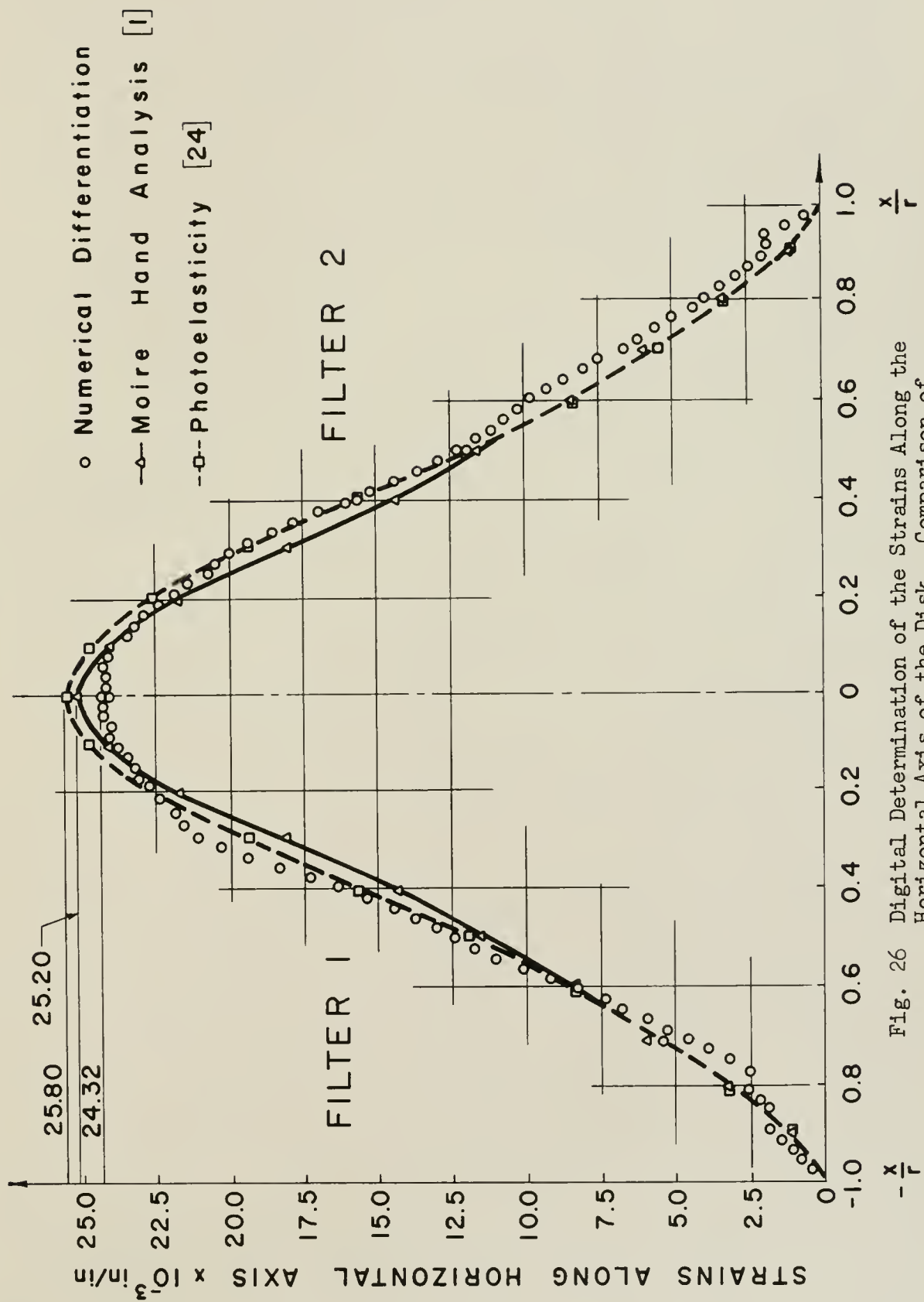
Fig. 26 Digital Determination of the Strains Along the Horizontal Axis of the Disk. Comparison of Results
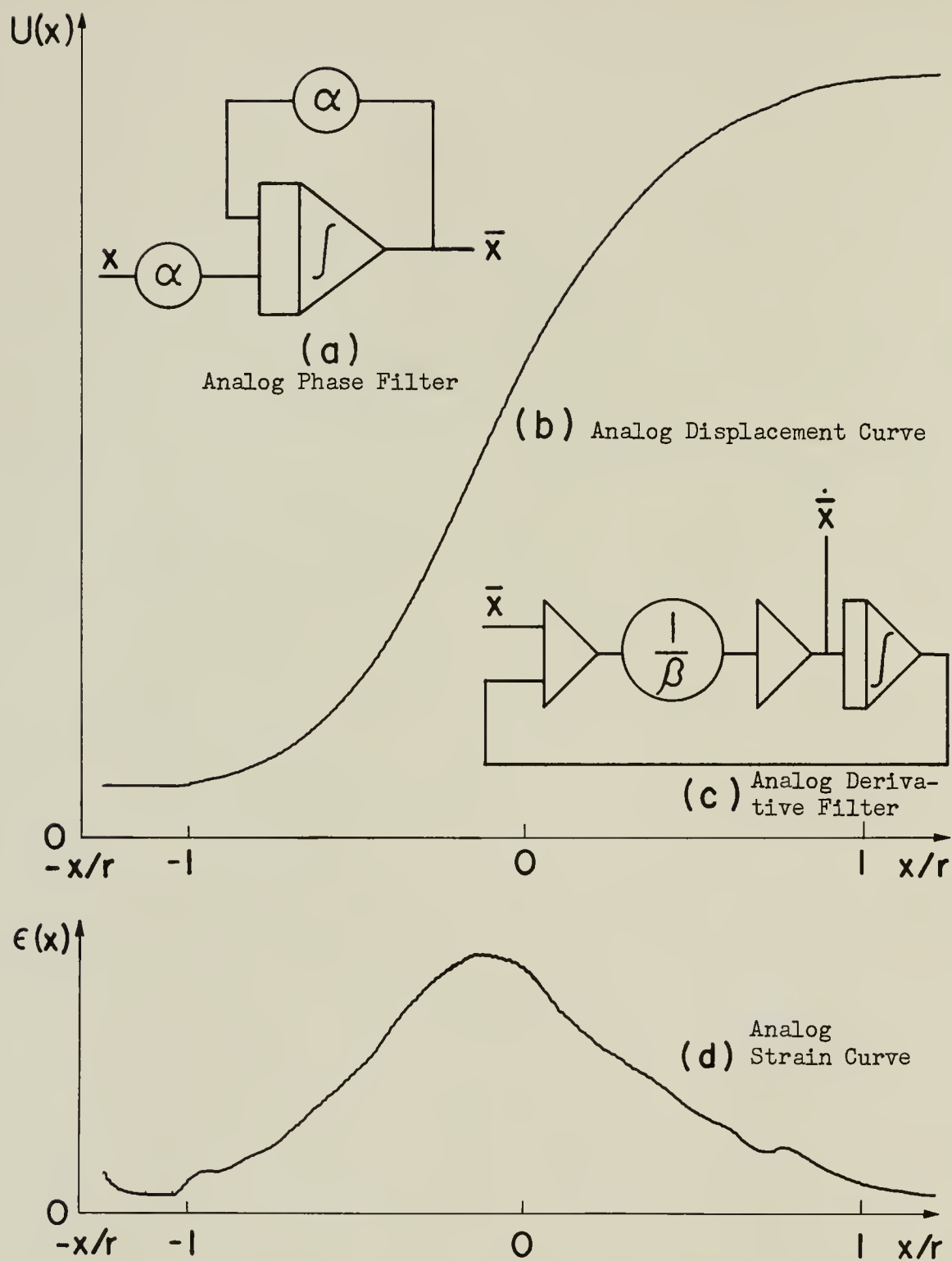
Fig. 27 Analog Filtering and Differentiating Circuits with
Their Corresponding Outputs

139
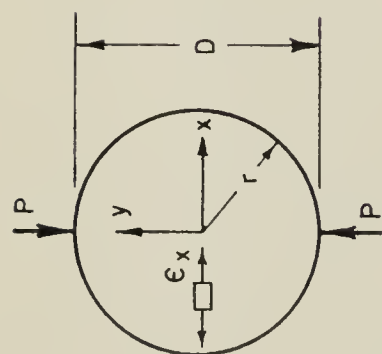
STRAINS ALONG HORIZONTAL AXIS
OF THE RING

— ○ — Sciammarella Hand Analysis [1]

— — — Automatic Hybrid System Results
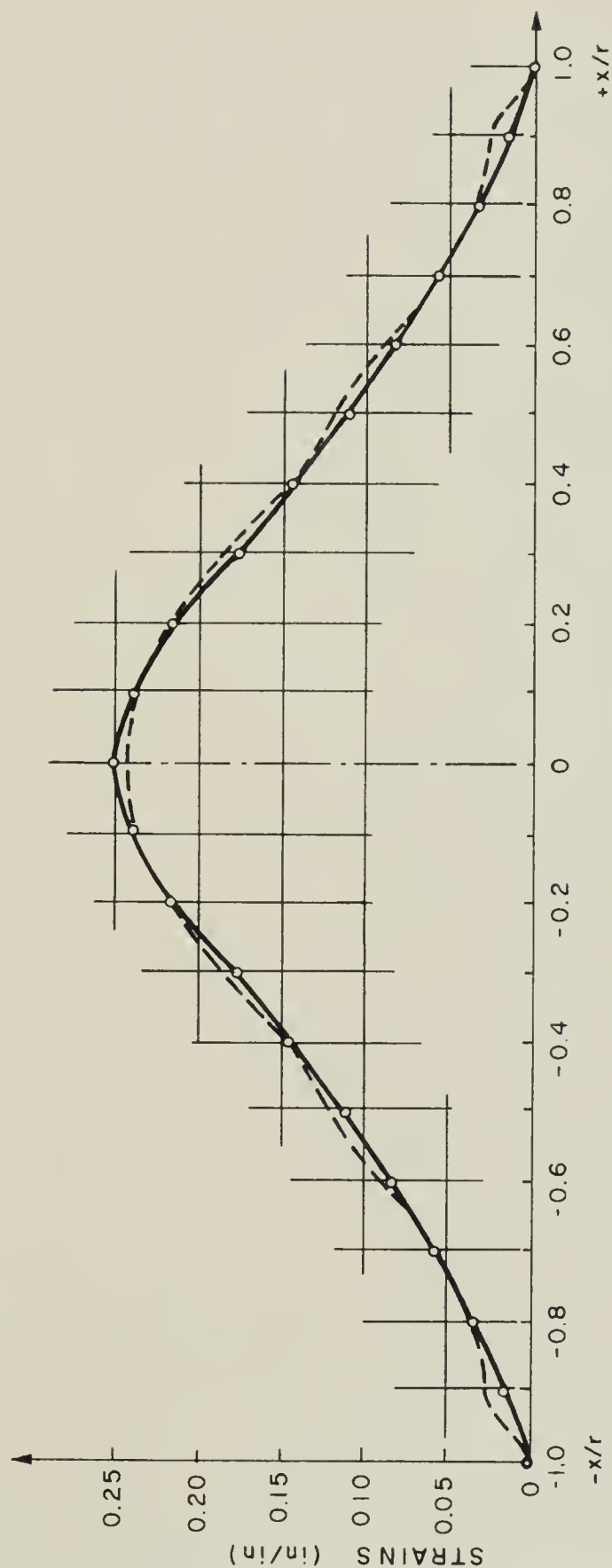
Fig. 28 Analog Determination of Strains. Comparison of Results
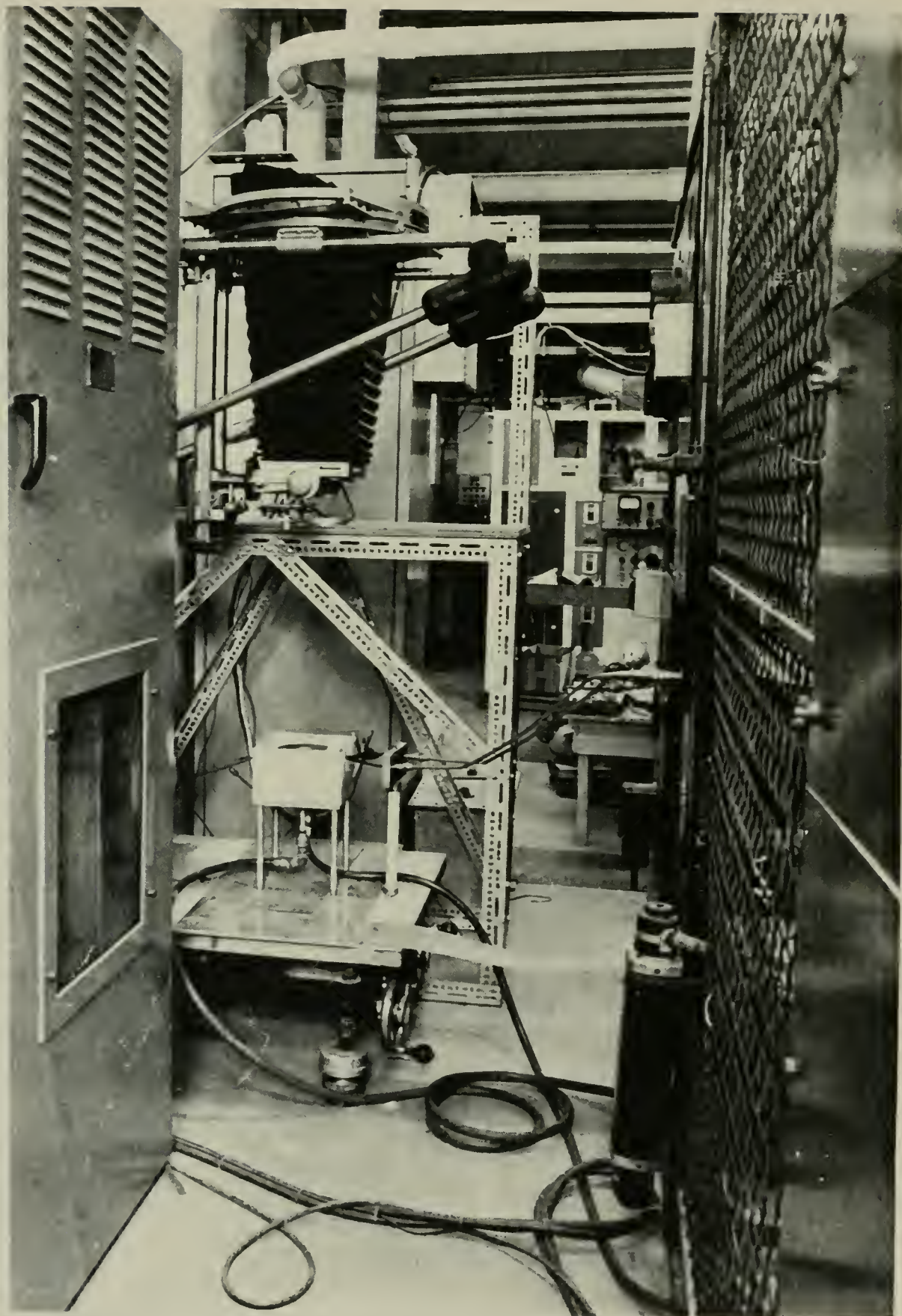
Fig. 29 General View of the Experimental Set-Up
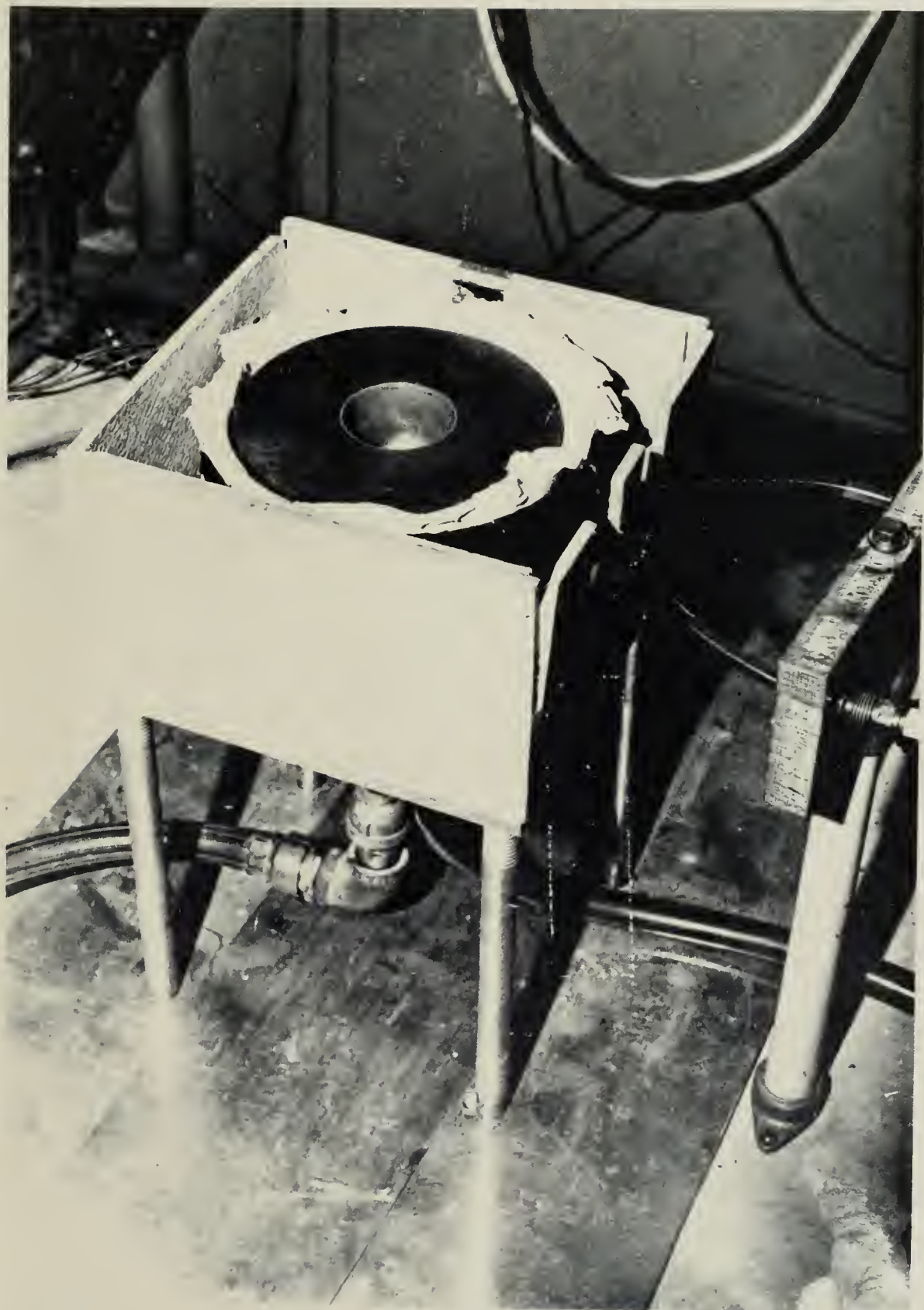
Fig. 30 Close View of the Model, Induction Coils, Insulator and Cooling
System

142
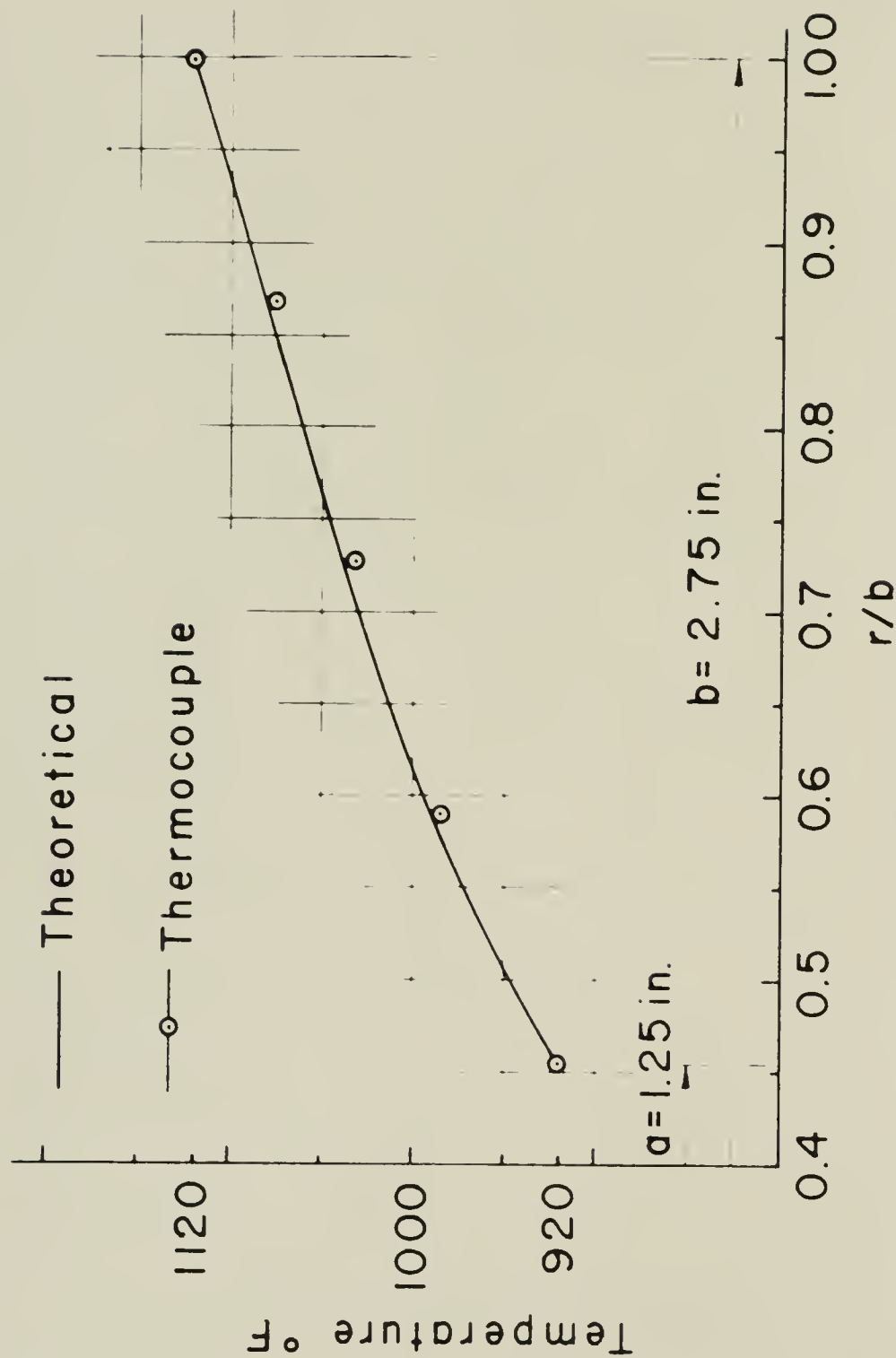
Fig. 31   Temperature Distribution in Ring No. 1
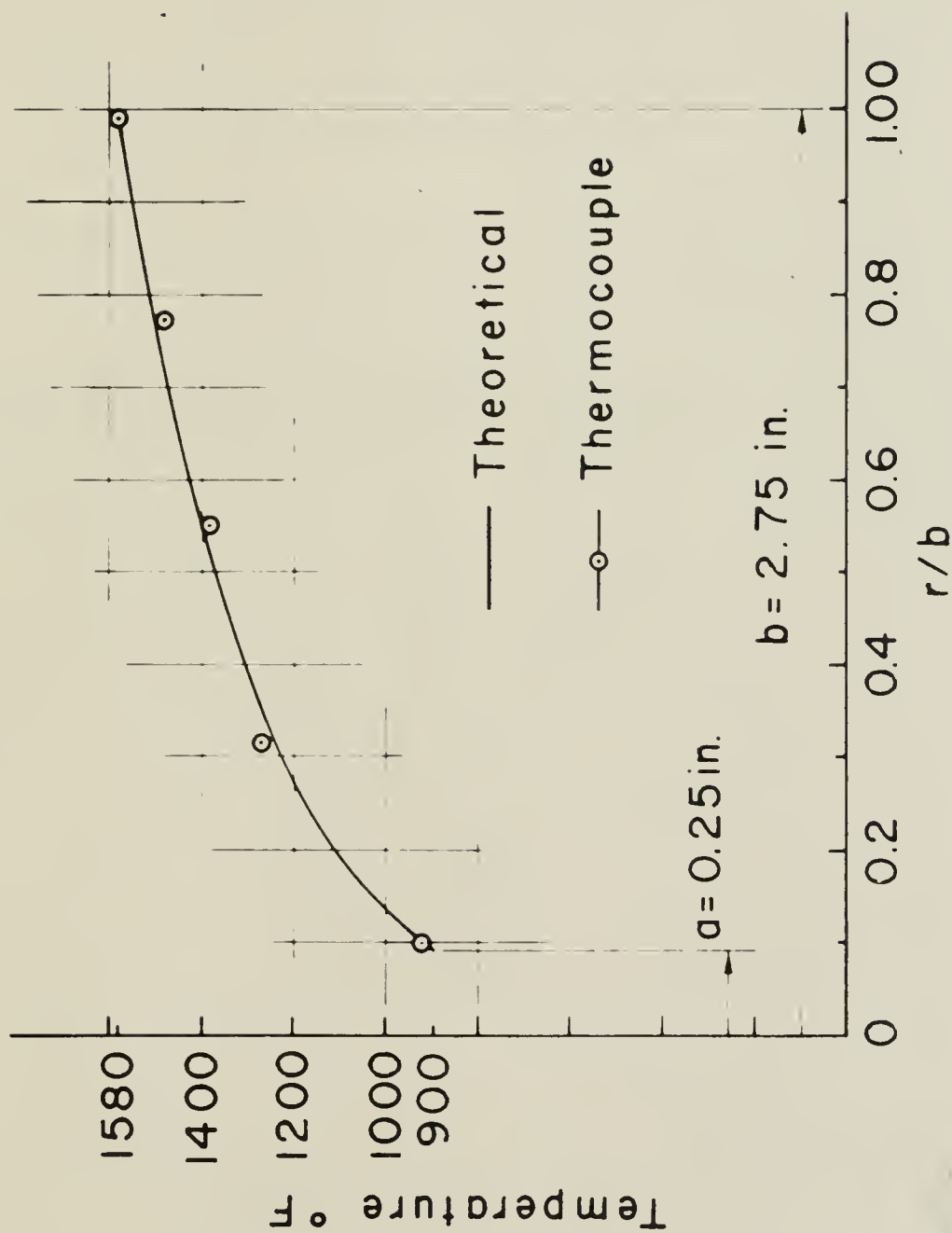
Fig. 32 Temperature Distribution in Ring No. 2
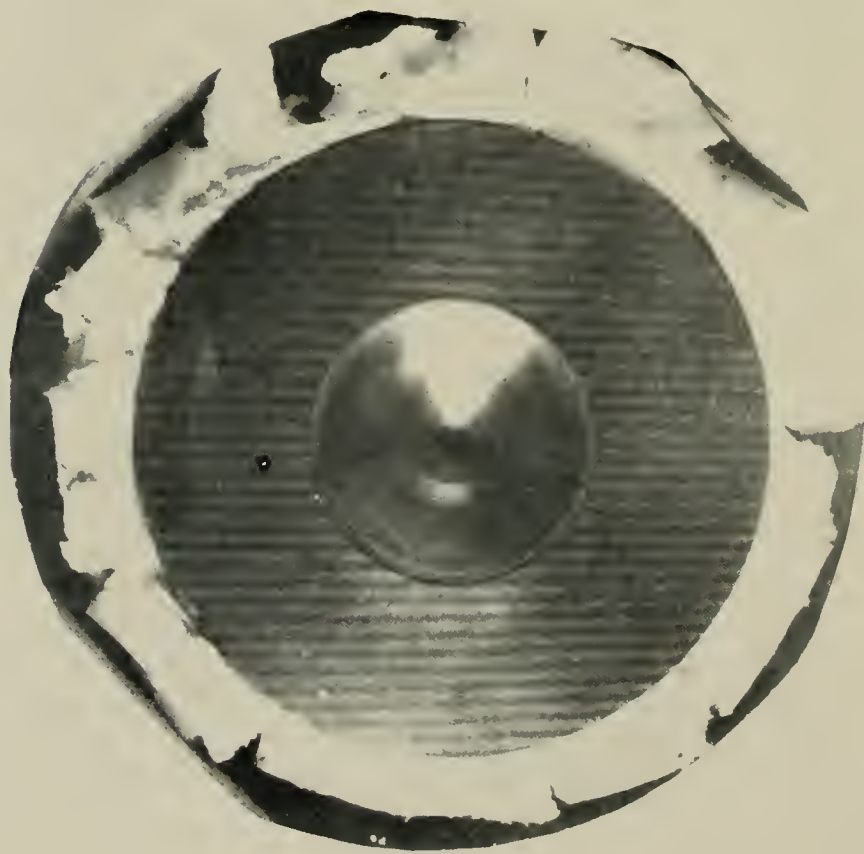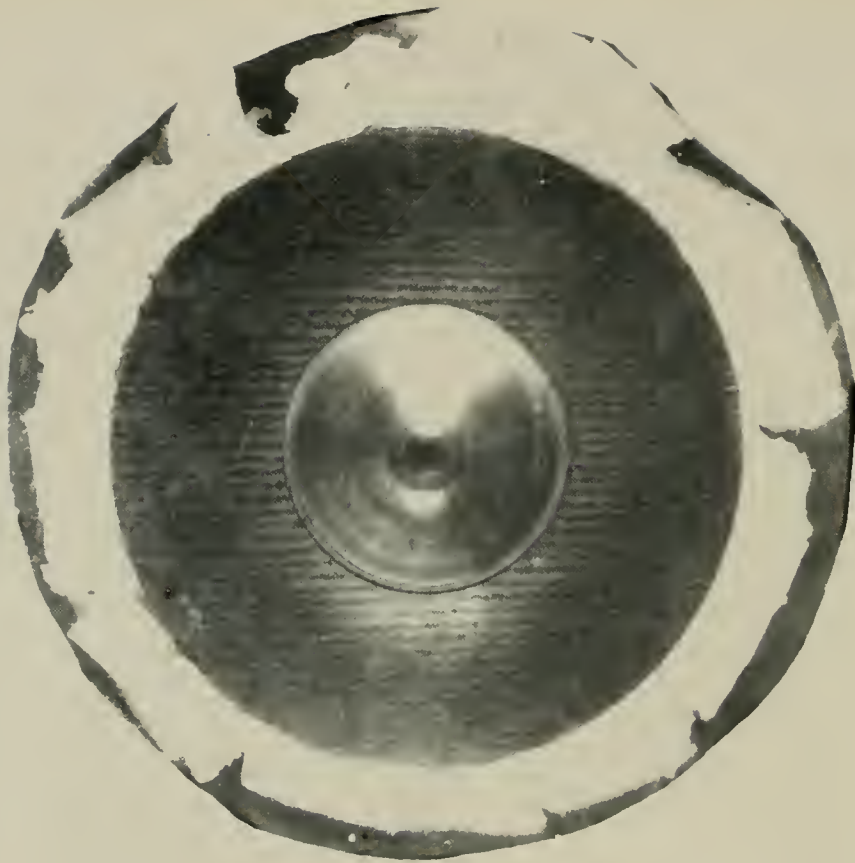
a) Room Temperature 80 °F. Initial Mismatch   b) Under Thermal Load. 1120 °F. OD, 920 °F. ID

Fig. 33 Moiré Patterns of Ring No. 1, 5.5 in. OD and 2.5 in. ID
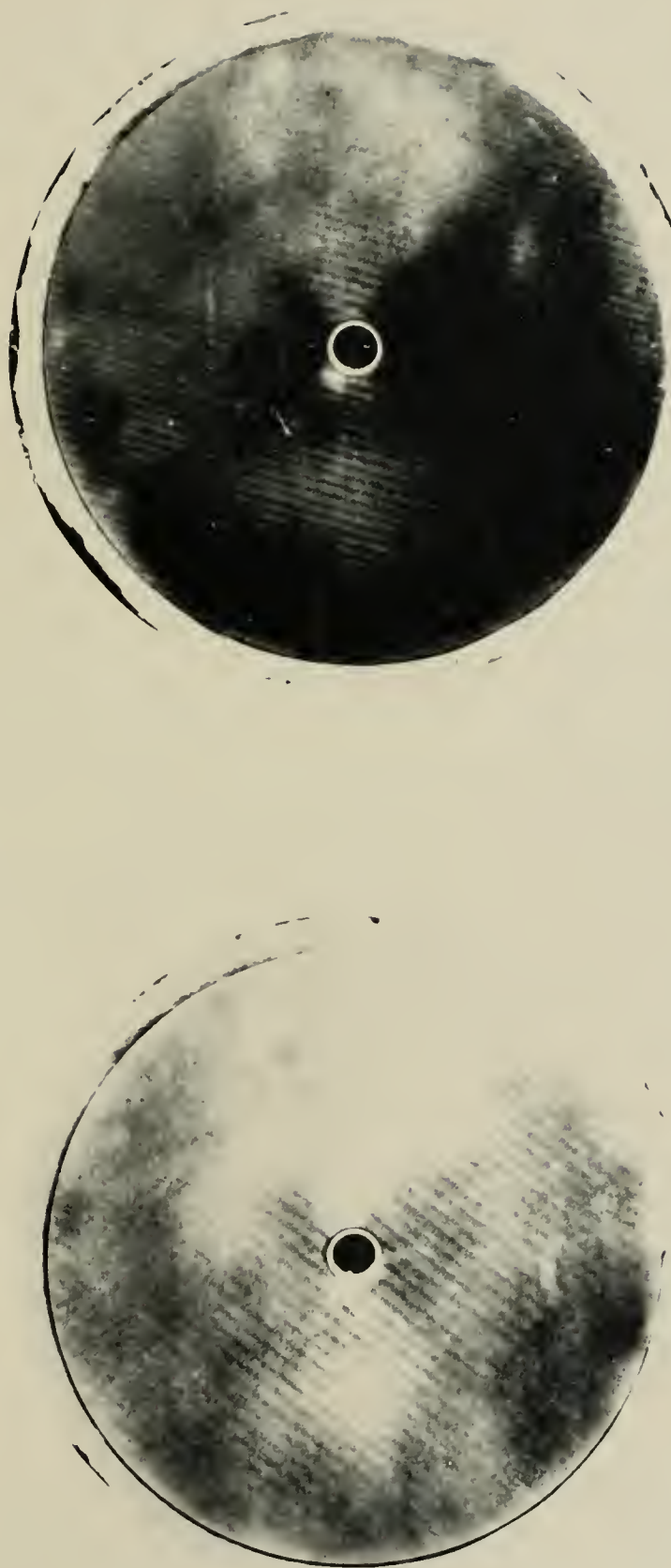
a) Room Temperature 80 °F. Initial Mismatch   b) Under Thermal Load. 1580 °F. OD, 900 °F. ID

Fig. 34 Moiré Patterns of Ring No. 2, 5.5 in. OD and 0.5 in. ID
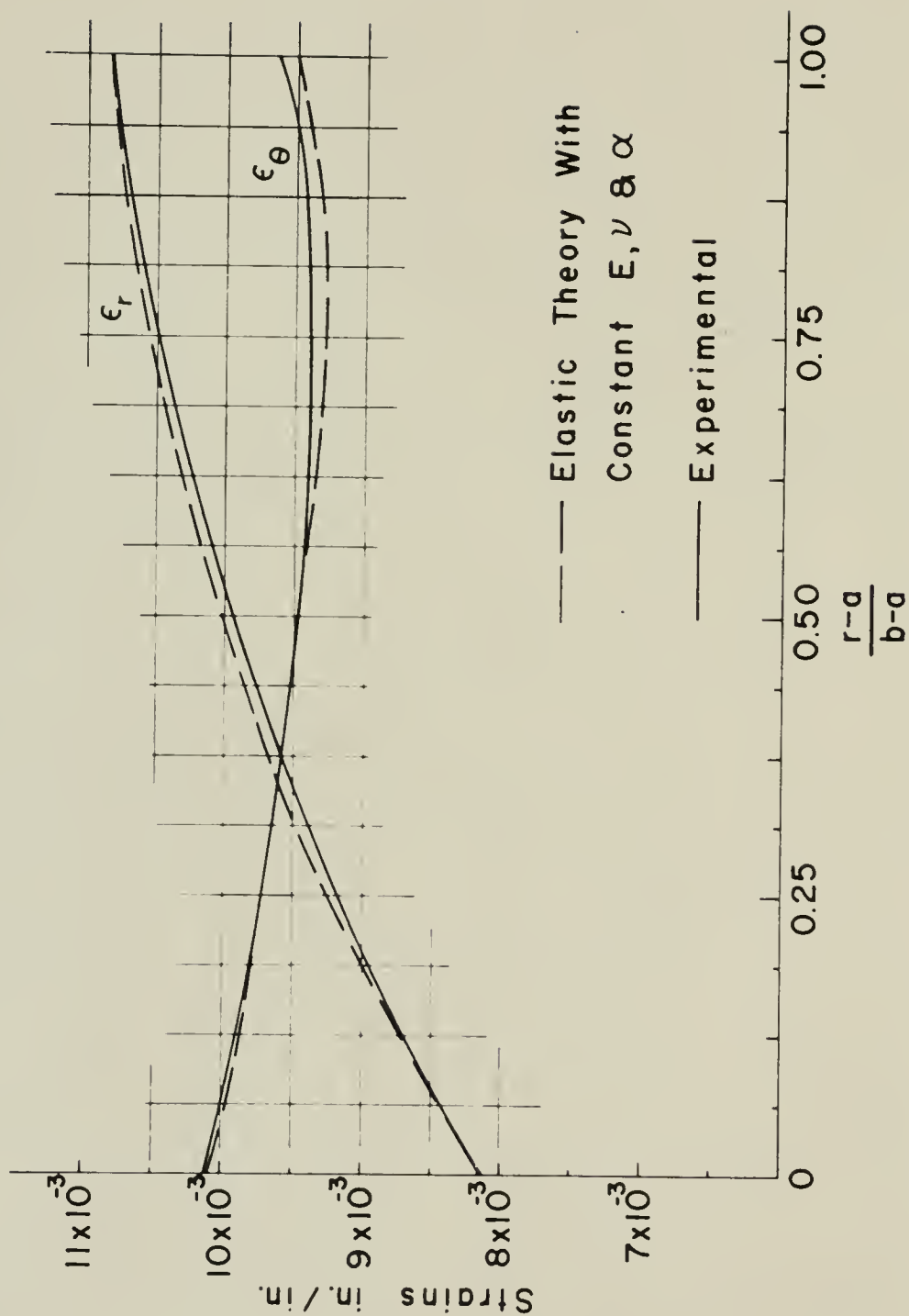
Fig. 35 Experimentally Measured Strains in Ring No. 1
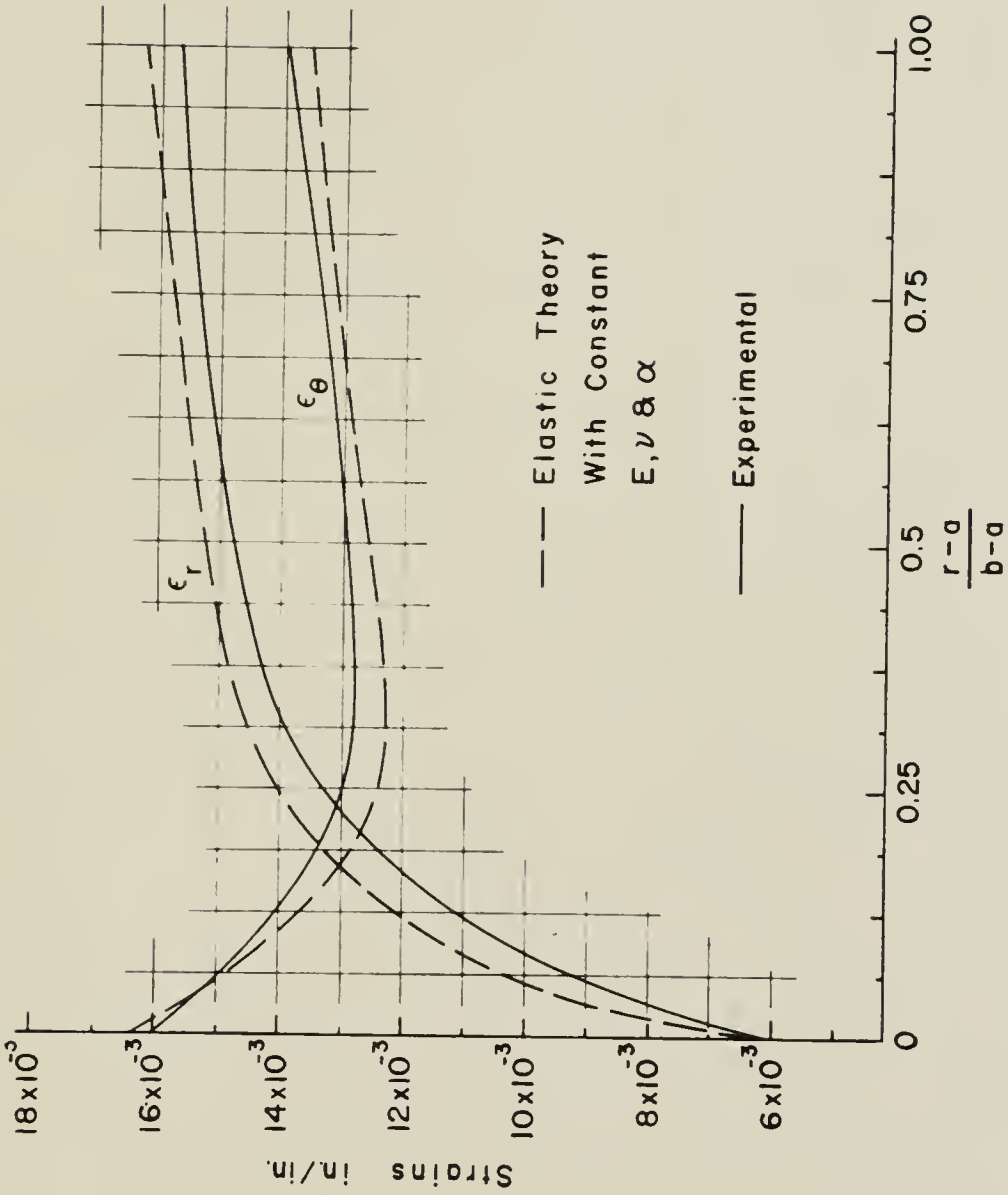
Fig. 36 Experimentally Measured Strains in Ring No. 2
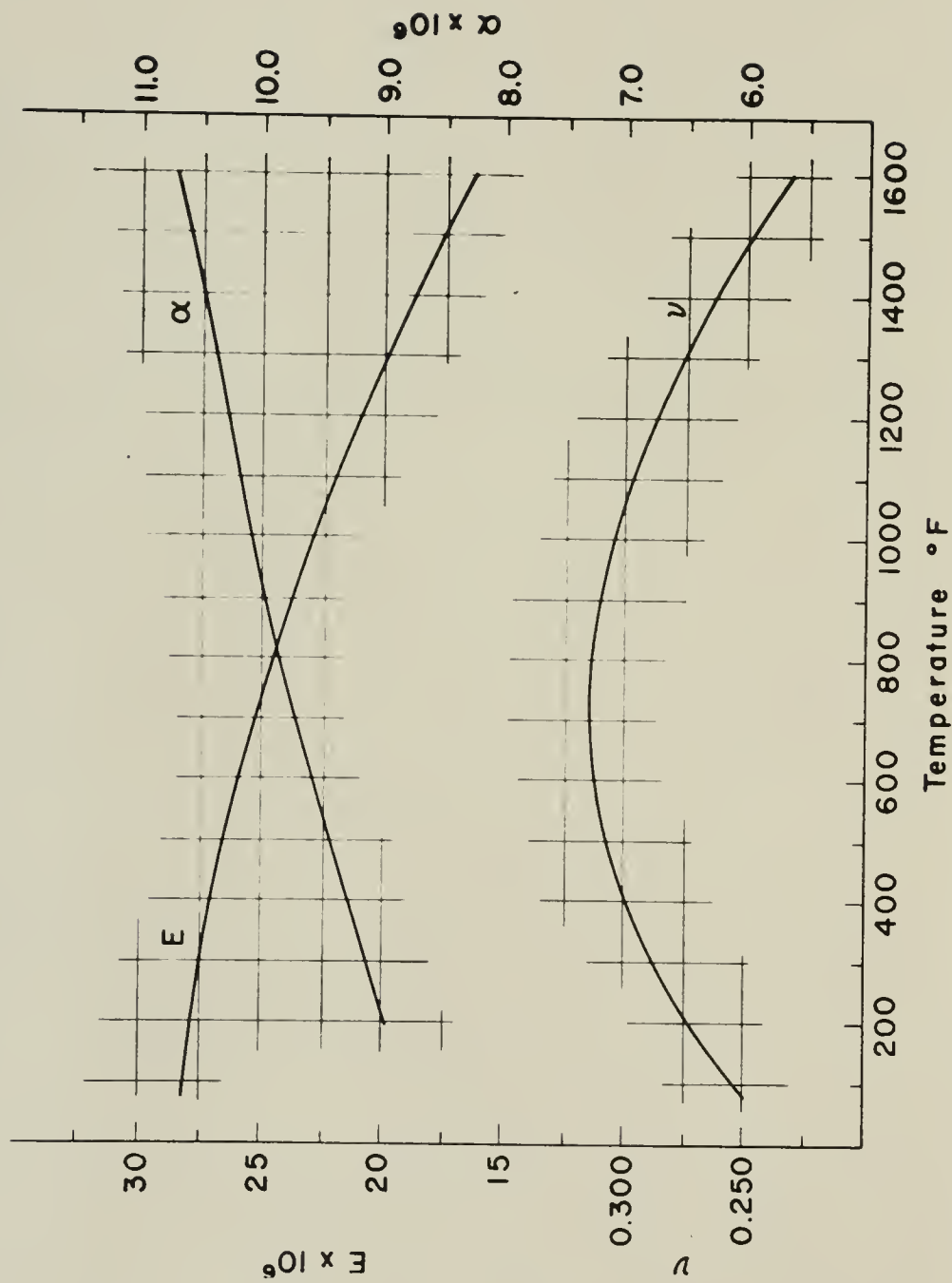
Fig. 37 Temperature Variation of the Mechanical Properties of
AISI 304 Stainless Steel
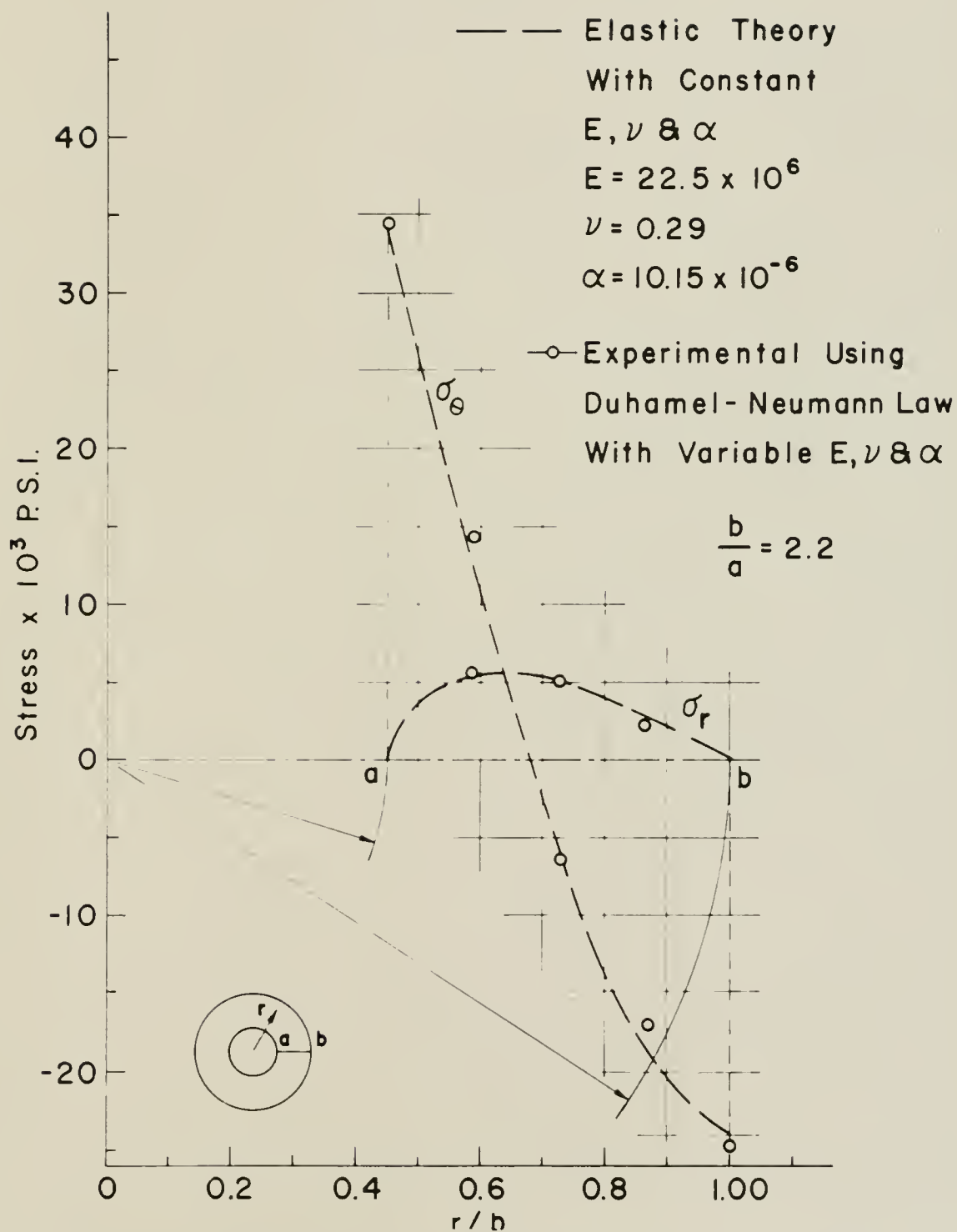
Fig. 38 Comparison of Experimental Stresses in Ring No. 1
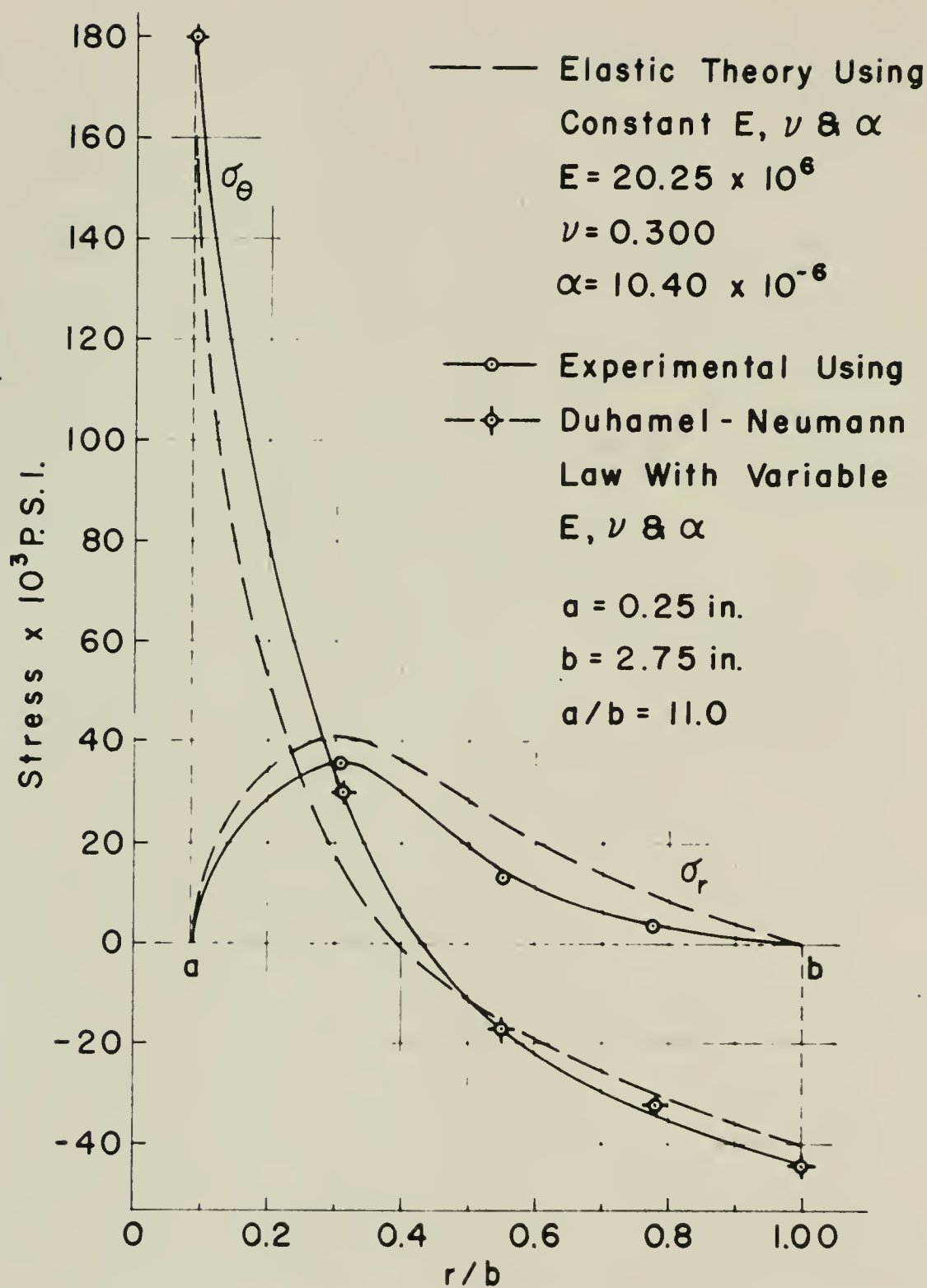with Those Predicted by Elastic Theory

Fig. 39 Comparison of Experimental Stresses in Ring No. 2
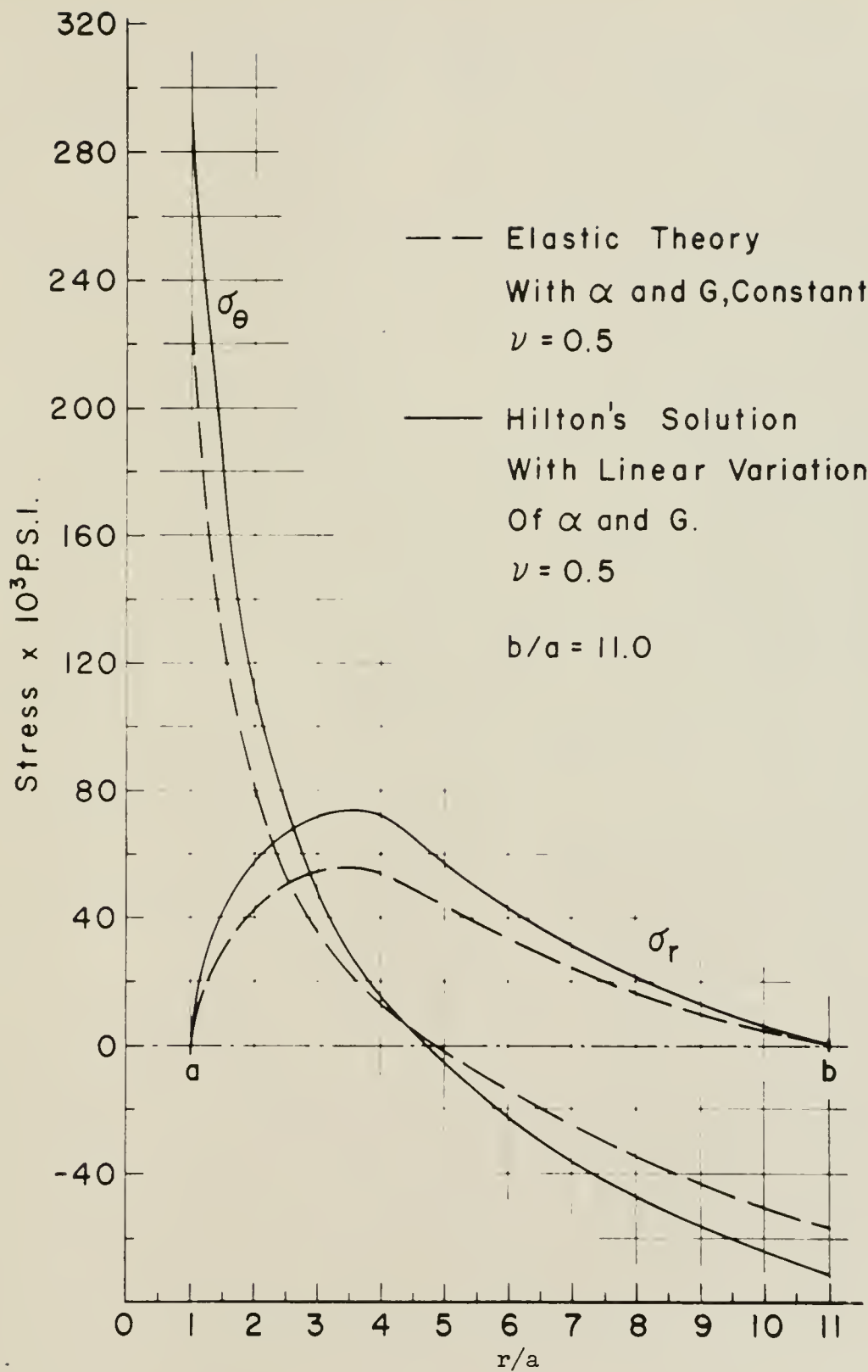with Those Predicted by Elastic Theory

Fig. 49 Comparison of Experimental Stresses for a
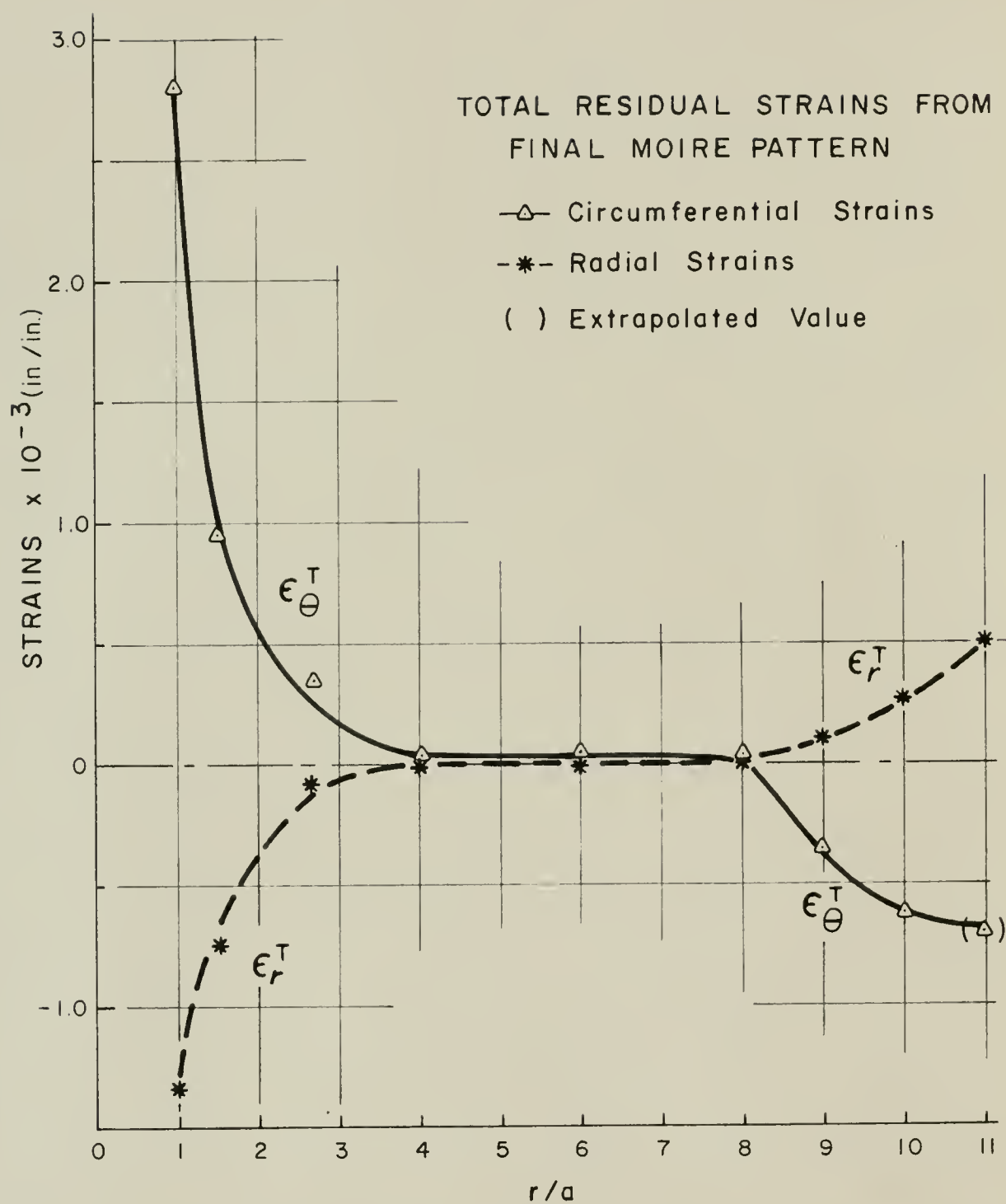Material with $\nu = 0.5$ with Hilton's Solution

Fig. 41 Total Residual Strains in Ring No. 2 by the Moiré Method
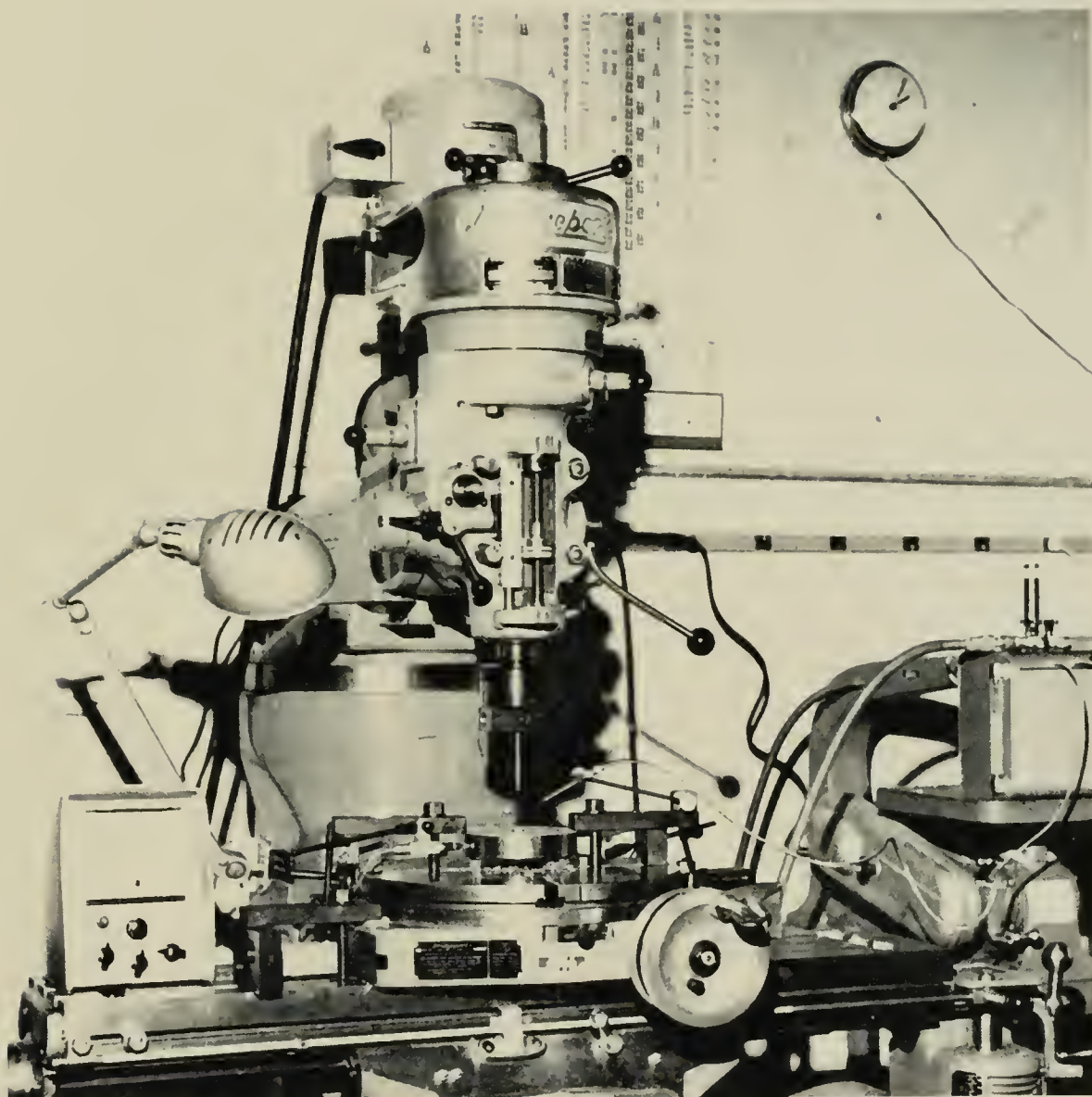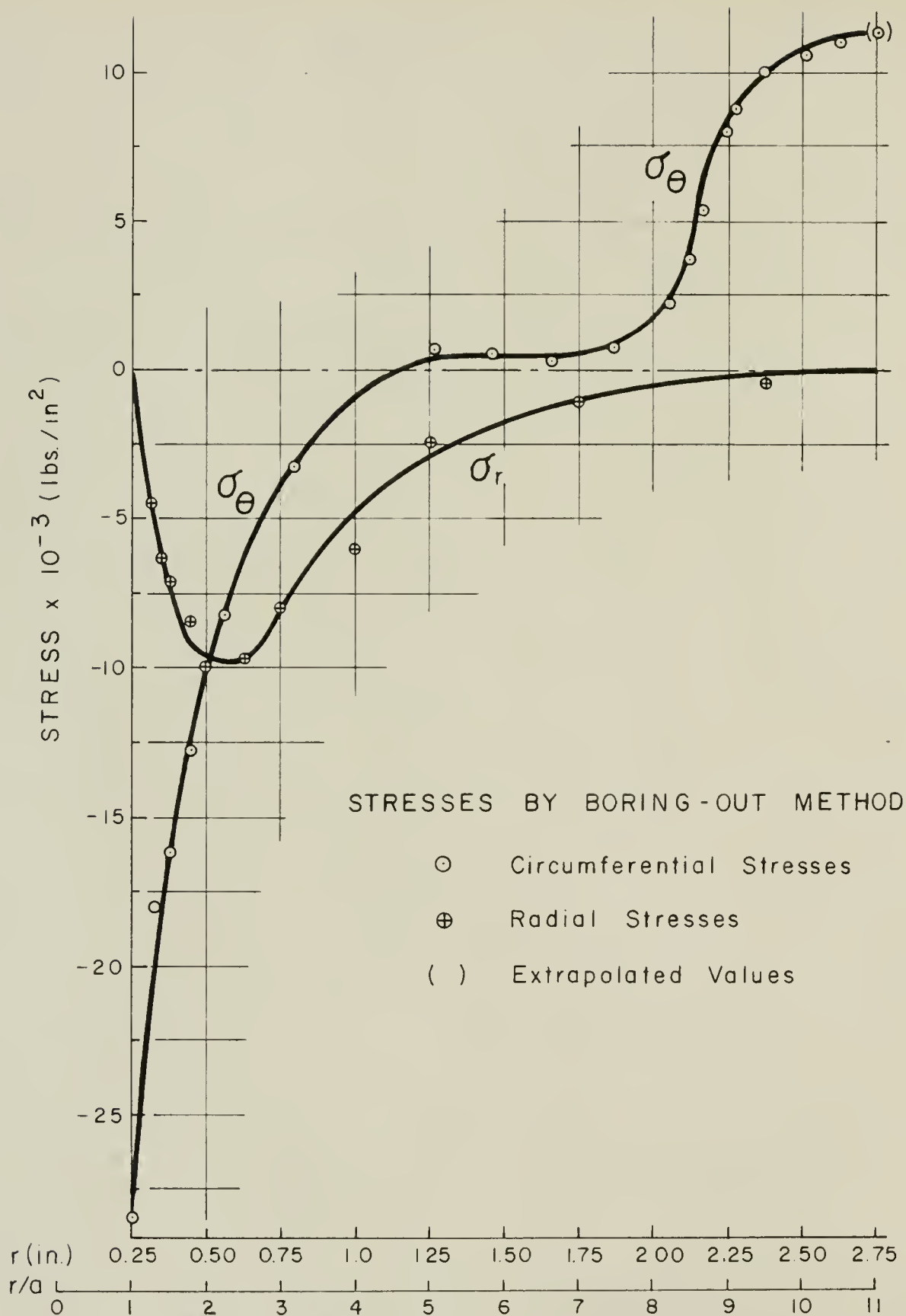
Fig. 42 Boring-Out Test Set-Up

Fig. 43 Residual Elastic Stresses in Ring No. 2
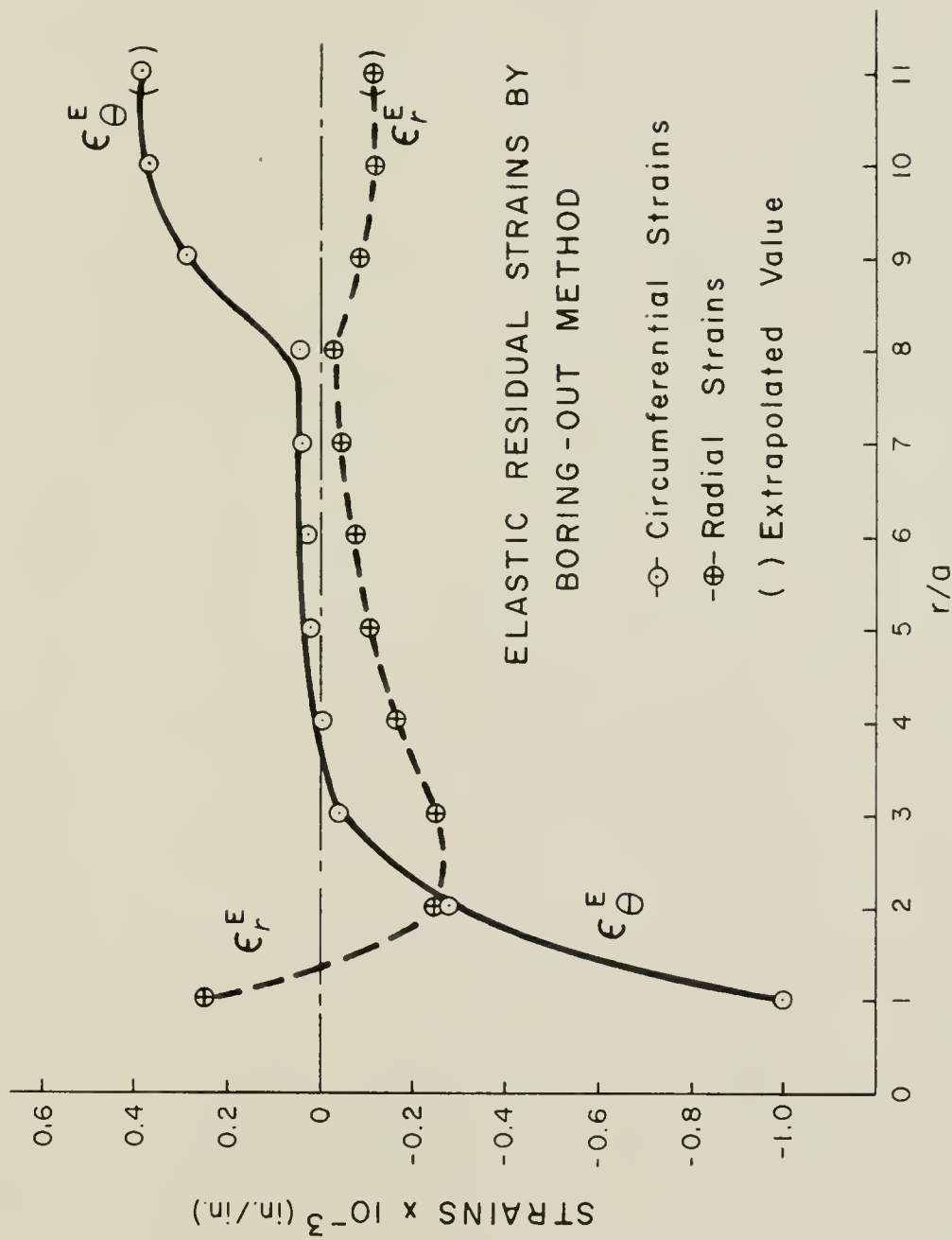
Fig. 44 Residual Elastic Strains in Ring No. 2
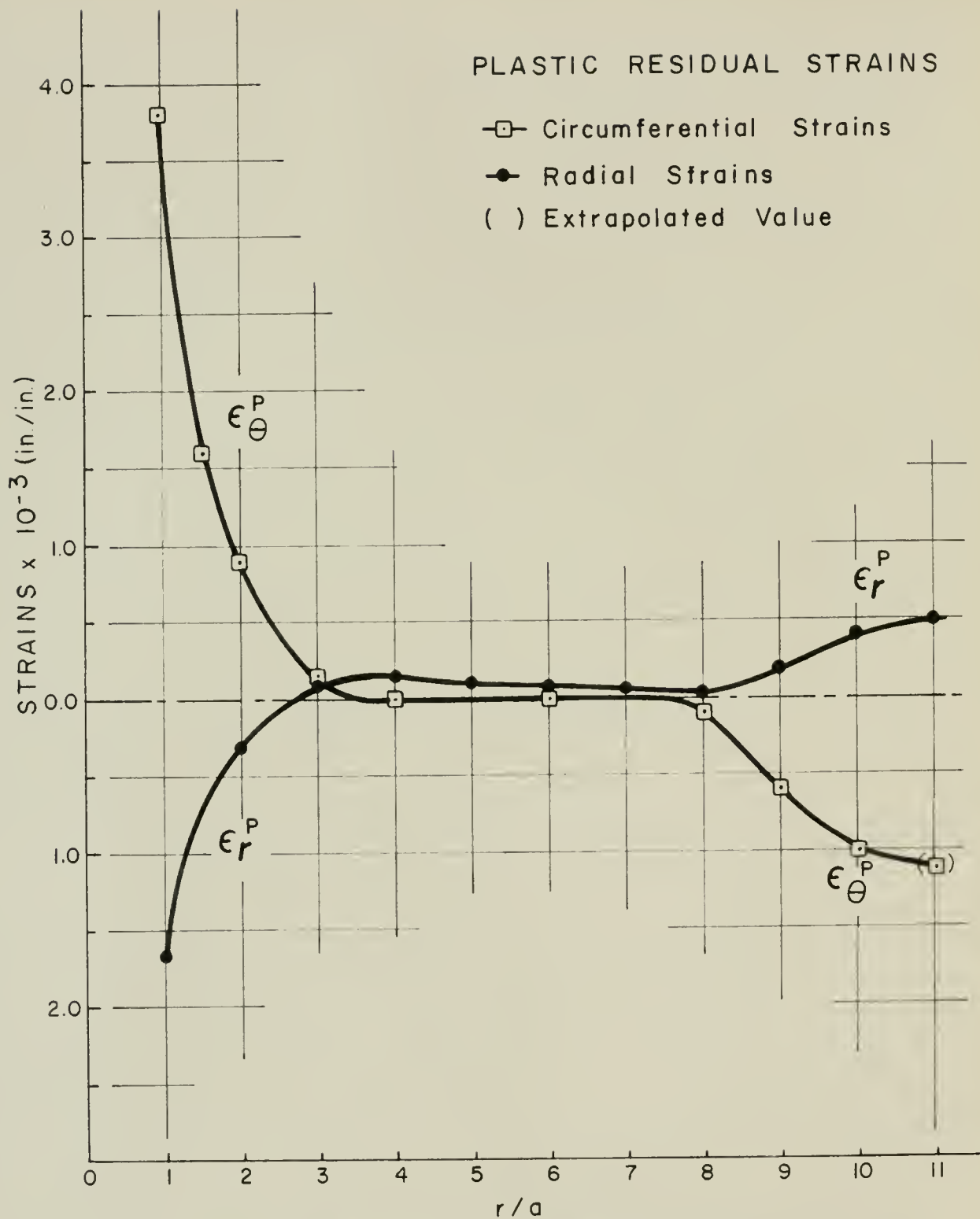
156

Fig. 45 Residual Plastic Strains in Ring No. 2
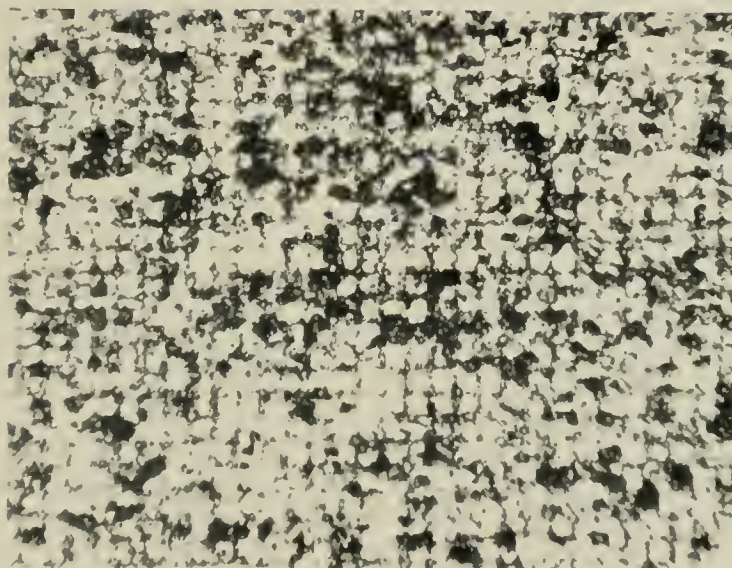
Fig. 46   100X   Magnification of an Attempt to Engrave 750 Lines
per Inch on an Insufficiently Polished Aluminum Sample
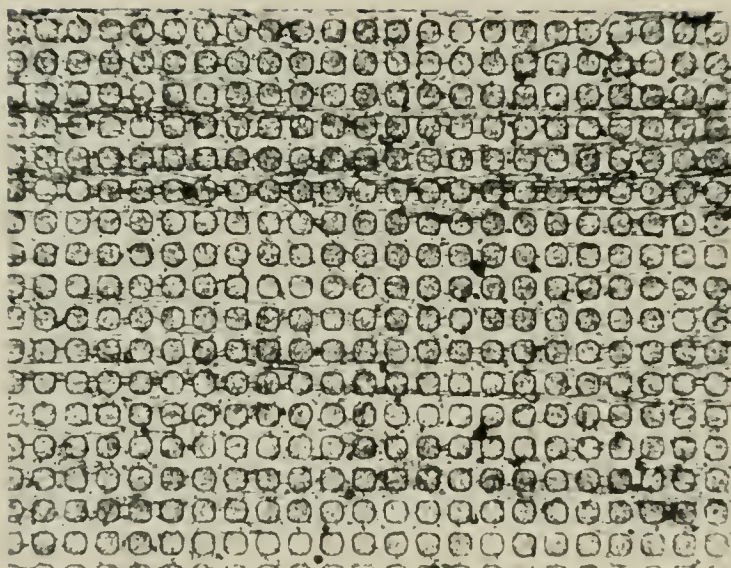
Fig. 47   40X Magnification of a Photoengraved Cross Grid of 300
Lines per Inch

PHOTORESIST

METAL
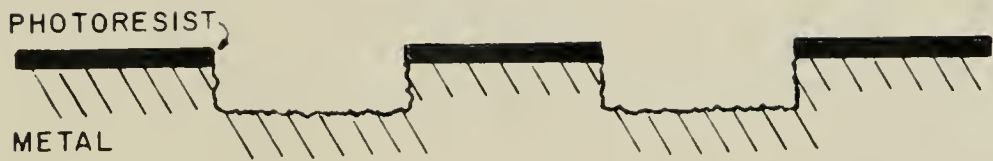
ETCHING WITH NO UNDERETCH

a
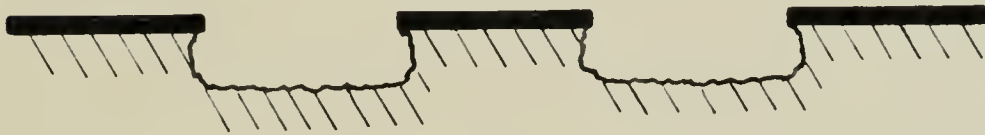
BEGINING OF UNDERETCHING

b

SUBSTANTIAL UNDERETCHING WITH
DESTRUCTION OF RONCHI RULING CHARACTER

c

DRAGON'S
BLOOD

ADDED PROTECTION AFFORDED BY
DRAGON'S BLOOD

d

Fig. 48   Diagram Showing Underetching Effect

Fig. 49   40X Magnification of an Etched Cross Grid of 300 Lines
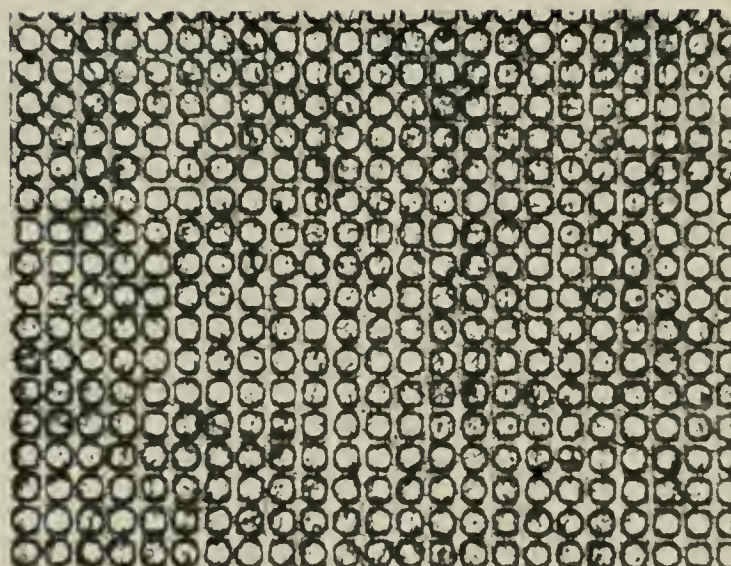per Inch After Removal of the Resist

APPENDIX E

DETERMINATION OF FILTER PARAMETERS

Numerous comment cards have been included in the programs of Appendix C to aid the user and to clarify the meaning of the abbreviations of the Fortran Statements.

We will describe here the sequence of operations leading to the determination of the adequate values for the independent parameters of Filters 1 and 2.

Filter 1

This filter possesses two independent parameters, the center frequency f_o and the number of terms in the trigonometric approximation of the transfer function m.

It is important to notice, Figure 21, that the band width, $\Delta f = 2\pi/m$, and the roll-off frequency interval, $2\pi/m$, depend on the value of m.

Keeping this in mind we proceed as follows:

a) Display in a standard IBM 80 x 80 listing the digitalized values of the light intensity trace obtained at equally spaced intervals along the direction of scan.

b) Determine the shortest and longest wavelength of the fringes in the trace in data point numbers. The difference of these two quantities defines the wavelength deviation $\Delta\lambda$. The frequency deviation is obtained as $\Delta f = 2\pi/\Delta\lambda$.

161

c) Obtain the center wavelength λ_o of the trace as the average of the shortest and longest wavelengths determined in (b). The center frequency will then be $f_o = 2\pi/\lambda_o$.

d) Assume for the first trial run that the band width of the filter is twice the frequency deviation. Then

$$2\Delta f = \frac{4\pi}{\lambda} = \frac{2\pi}{m} \tag{E.1}$$

and the parameter m can be defined by

$$m = \frac{\pi}{\Delta f} = \frac{\Delta\lambda}{2} \tag{E.2}$$

e) Load the calculated parameters f_o and m into the program of Page 97 and perform the first trial run.

f) Inspect the plotted output of the amplitude vector that has been called phaser length in the program. These values should be approximately constant for minimum error in a properly tuned filter. Inspect the plotted output of the displacement curve to determine the wavelength of the noise, if any, that is passing through the filter.

g) If unsatisfactory results have been obtained in the first trial, adjust the values of f_o and m in successive runs until the filter yields a smooth displacement curve with minimum variations in the magnitude of the amplitude vector.

In evaluating this filter for a possible moiré application the reader should keep in mind the following:

Some spurious disturbances in the output of the filter can be due to noise content close to the signal frequencies that are passing through the filter in the roll-off interval $2\pi/m$. In order to narrow this interval m can be increased. However, this decreases the band

width and might obliterate some information on the desired signal.

On the other hand, if the useful signal is contained in a broad band, the value of m necessarily must be small to widen the band pass of the filter. This will cause the roll-off interval to widen and will reduce the number of terms in the series approximation of the transfer function imparing the accuracy of the procedure.

The shortcomings mentioned above lead us to believe that the use of Filter 1 should be restricted to moiré light intensity traces of narrow-band frequency composition with noise spectra well removed from the signal spectra.

Filter 2

This filter possesses five independent parameters, the number of terms in the trigonometric approximation of the transfer function N, the center frequency f_o, the cut-off frequency f_c, the termination frequency f_t and the coefficient k that defines the extent of the parabolic transitions of the roll-off, Figure 22.

This filter affords the possibility of defining the number of terms in the expansion of the transfer function, the band width and the roll-off frequency interval independently.

The independent parameters are determined as follows:

a), b) and c) are the same as for Filter 1.

d) Assume for the first trial run that the cut-off frequency is

$$f_c = f_o + \frac{\Delta f}{2} = f_o + \frac{2\pi}{\Delta \lambda} \qquad (E.3)$$

e) The values for N and k will depend on the noise composition of the input; however, N will rarely exceed 40 and a value of k between

0.2 and 0.4 will produce good results in most cases.

    f) The parameter

$$\lambda_r = \frac{f_t - f_c}{f_s} \qquad\qquad (E.4)$$

that permits us to define the termination frequency f_t as a function of the cut-off frequency f_c and the sampling frequency f_s, can be obtained by using the criteria given in [30].

    g) Load the calculated parameters f_o, N, k, f_c and f_t into the program of Page 100 and perform the first trial run.

    h) Perform the inspections described in (d) of Filter 1.

    i) If unsatisfactory results are obtained in the first trial, adjust the values of the independent parameters in successive runs until the filter is properly tuned.

    The existence of five independent parameters will permit more accurate and fast tuning of this filter than of Filter 1.

LIST OF REFERENCES

1. Sciammarella, C.A., Theoretical and Experimental Study of Moiré Fringes, Illinois Institute of Technology, pp. 1-6, 188-189, June 1960.

2. Theocardis, P. S., "Moiré Fringes, A Powerful Measuring Device," Applied Mechanics Reviews, Vol. 15, No. 5, pp. 333-339, May 1962.

3. Sciammarella, C. A., "Basic Optical Law in the Interpretation of Moiré Patterns Applied to the Analysis of Strains, Part I," Experimental Mechanics, Vol. 5, No. 5, pp. 154-160, May 1965.

4. Ross, B. E., Sciammarella, C. A., and Sturgeon, D., "Basic Optical Law in the Interpretation of Moiré Patterns Applied to the Analysis of Strains, Part II," Experimental Mechanics, Vol. 5, No. 6, pp. 161-166, June 1965.

5. Dantu, P., "Utilisation de Reseaux pour l'Etude Experimentale des Phenomenes Elastiques et Plastiques," Comptes Rendues Academie des Sciences, Paris, Vol. 239, pp. 1769-1771, December 1954.

6. Sciammarella, C. A., "Techniques of Moiré Fringe Interpolation," to be published in Experimental Mechanics.

7. Hempenius, S. A., "Aspects of Photographic Engineering," Applied Optics, Vol. 3, No. 1, pp. 45-53, January 1964.

8. Kelly, D. H., "Systems Analysis of the Photographic Process. II, Transfer Function Measurements," Journal of the Optical Society of America, Vol. 51, No. 3, pp. 319-330, March 1961.

9. Modulation Transfer Data for Kodak Films, Kodak Pamphlet No. P-49, Eastman Kodak Company, Rochester, New York.

10. Washer, F. E., "The Testing of Photographic Lenses," Photographic Engineering, Vol. 5, No. 1, pp. 37-53, 1954.

11. Lamberts, R. L., "Measurement of Sine Wave Response of a Photographic Emulsion," Vol. 49, No. 5, pp. 425-428, May 1959.

12. Lamberts, R. L., "The Production and Use of Variable Transmittance Sinusoidal Test Objects," Applied Optics, Vol. 2, No. 3, pp. 273-276, March 1963.

13. Dawton, R. H., "The Integration of Large Numbers of X-Ray Crystal Reflections," Vol. 50, pp. 919-926, 1938.

14. O'Neill, E. L., "Spatial Filtering in Optics," IRE Transactions on Information Theory, Vol. IT-2, No. 2, pp. 56-65, June 1956.

15. Cutrona, L. J., Leith, E. N., Palermo, C. J., and Porcello, L. J., "Optical Data Processing and Filtering Systems," IRE Transactions on Information Theory, Vol. IT-6, pp. 386-400, June 1960.

16. Tsujiuchi, J., "Correction of Optical Images by Compensation of Aberrations and by Spatial Frequency Filtering," Progress in Optics, ed., E. Wolf, pp. 131-180, 1963.

17. Vander, Lugt A., "Signal Detection by Complex Spatial Filtering," IRE Transactions on Information Theory, Vol. IT-10, No. 2, pp. 139-145, April 1964.

18. Cheatham, T. P., and Kohlenberg, A., "Optical Filters, Their Equivalence and Difference from Electrical Networks," IRE Convention Record, Part 4, pp. 6-12, 1954.

19. Steel, W. H., "Etude des Effets Combines des Aberrations et d'une Obturation Centrale de la Pupille Sur le Contraste des Images Optiques," Revue d'Optique, Vol. 32, pp. 4-26, 143-178, 269-306, 1953.

20. O'Neill, E. L., Introduction to Statistical Optics, Addison-Wesley Series in Advanced Physics, Addison-Wesley Publishing Co., United States, pp. 86-99, 1963.

21. Françon, M., Modern Applications of Physical Optics, No. 13, Interscience Tracts in Physics and Astronomy, Interscience Publishers, New York, pp. 70-74, 1963.

22. Lanczos, C., Applied Analysis, Prentice-Hall Mathematical Series, Prentice-Hall, Inc., New York, pp. 321-327, 1956.

23. Timoshenko, A. J., and Goodier, J. N., Theory of Elasticity, 4th Edition, McGraw-Hill Book Co., New York, pp. 107-109, 412-416, 1951.

24. Durelli, A. J., and Mulzet, A. P., "Large Strain Analysis in Linear Materials," Journal of the Engineering Mechanics Division, ASCE, EM 3, 65-91, June 1965.

25. Goodier, J. N., "Compression of Rectangular Blocks and the Bending of Beams by Non-Linear Distributions of Bending Forces," Transactions ASME, Vol. 54, pp. 173-183, 1932.

26. Gabor, D., "Theory of Communication," Journal of the Institution of Electrical Engineers, Vol. 93, Part III, No. 26, pp. 432-433, November 1946.

27. Middleton, D., An Introduction to Statistical Communication Theory, McGraw-Hill Book Co., New York, p. 102, 1960.

28. Ville, J., "Théorie et Applications de la Notion de Signal Analytique," Cables et Transmissions, Vol. 2, p. 61, 1948.

29. Woodward, P. M., Probability and Information Theory with Applications to Radar," McGraw-Hill Book Co., New York, 1953.

30. Ormsby, J. F. A., "Design of Numerical Filters with Applications to Missile Data Processing," Journal of the Association for Computing Machinery, Vol. 8, No. 3, pp. 440-466, July 1963.

31. Goodman, N. R., "Measuring Amplitude and Phase," Journal of the Franklin Institute, Vol. 270, pp. 437-450, December 1960.

32. Anders, E. B., Johnson, J. J., Lasaine, A. D., Spikes, P. W., and Taylor, J. T., "Digital Filters," NASA Contract No. NAS8-5164, pp. 43-75, July 1964.

33. von Sanden, H., Praktische Mathematic, Verlagsgesellschaft, Stuttgart, pp. 138-143, 1961.

34. Moore, M. N., The Dispersion of Thermal Neutron Pulses in Neutronic Systems, USAEC Contract AT (11-1), pp. 8-11, 1964.

35. Friant, R. T.,Jr., Practical Digital Data Smoothing, G. E. Technical Information Series, Appendices I and VIII, June 1958.

36. Ross, B. E., A Generalization of the Moiré Method with Applications to the Thermal Stress Problem, University of Florida, pp. 101-102, 103-105, December 1960.

37. Sciammarella, C. A., and Sturgeon, D., "Thermal Stresses at High Temperatures in Stainless Steel Rings by the Moiré Method," presented at the 2nd International Congress of Experimental Mechanics, October 1965, to be published in Experimental Mechanics.

38. Hilton, H. H., "Thermal Stresses in Bodies Exhibiting Temperature-Dependent Elastic Properties," Journal of Applied Mechanics, pp. 350-354, September 1952.

39. Chang, C. C., and Chu, W. W., "Stresses in a Metal Tube Under Both High Radial Temperature Variation and Internal Pressure," Journal of Applied Mechanics, pp. 101-108, June 1954.

40. Trostel, R., "Warmespannungen in Hohlzylindern mit temperature-abhängigen Stoffwerten," Ingenieur-Archiv XXVI, 134-142, 1958.

41. Nowacki, W., Thermoelasticity, Addison-Wesley Publishing Co., Reading, Massachusetts, pp. 593-594, 1962.

42. Boley, B. A., and Weiner, T. H., Theory of Thermal Stresses, John Wiley and Sons, Inc., New York, pp. 288-291, 1960.

43. Garofalo, F., Malenock, P. R., and Smith, G. V., "The influence of temperature on the elastic constants of some commercial steels," ASTM Symposium on elastic constants STP No. 129, p. 17, 1952.

44. Haythorn, P. A., "Sheet Metals for High Temperature Service Iron Age," Vol. 162, p. 93, September 23, 1948.

45. Sachs, G., and Espey, G., "The Measurement of Residual Stresses in Metals," The Iron Age, pp. 63-71, September 18, 1941.

46. Bühler, H., "Complete Determination of the State of Residual Stress in Solid and Hollow Metal Cylinders," Residual Stresses in Metals and Metal Construction, Reinhold Publishing Corp., New York, pp. 305-329, 1954.

47. Guild, T., Diffraction Gratings as Measuring Scales, Oxford University Press, London, 1960.

48. Burch, T. M., "The Metrological Application of Diffraction Gratings," Progress in Optics, ed., E. Wolf, Vol. 2, pp. 73-108, 1960.

49. McIlraith, A. H., "An Introduction to the Theory of Crossed Diffraction Gratings and Their Application to Linear Measurement," Machine Shop, Vol. 23, No. 4, pp. 202-213, April 1962.

50. Dantu, P., "Utilization des Reseaux pour l'Etude des Déformations," Laboratoire Central des Ponts et Chaussés, Paris, Publication 57-6, 1957.

51. Parks, V. T., and Durelli, A. T., Moiré Patterns of Partial Derivatives of Displacement Components, School of Engineering and Architecture, The Catholic University of America, Washington, D.C., June 1965.

52. Sciammarella, C. A., and Ross, B. E., "Thermal Stresses in Cylinders by the Moiré Method," Experimental Mechanics, Vol. 4, No. 10, pp. 289-296, October 1964.

53. Industrial Uses of Kodak Photo Resist, Kodak Pamphlet No. Q-24, Eastman Kodak Company, Rochester, New York, 1959.

54. Theocardis, P., private communication.

BIOGRAPHICAL SKETCH

Donald L. G. Sturgeon was born January 15, 1937, at General Pico,
La Pampa, Argentina. He obtained his Diploma in Civil Engineering from
the College of Engineering of the University of Buenos Aires in August,
1959.

During the period July, 1958, to December, 1960, he was employed
with Sir William Halcrow and Partners, a British firm of consulting engi-
neers on location in Buenos Aires, Argentina. From January, 1961, to May,
1963, he was self-employed as a registered engineer in a professional
partnership concerned with the analysis and design of reinforced concrete
structures. During this same period he acted as Graduate Assistant to the
Chair of Advanced Strength of Materials at his Alma Mater.

In April, 1963, the author enrolled in the Graduate School of the
University of Florida. Since that date he has held a Research Assistant-
ship in the Department of Engineering Science and Mechanics while ful-
filling the academic requirements for the degree of Doctor of Philosophy.

The writer is married to the former Nelda Mabel Altuna and is
the father of one daughter. He is a student member of the Society for
Experimental Stress Analysis.

This dissertation was prepared under the direction of the chairman of the candidate's supervisory committee and has been approved by all members of that committee. It was submitted to the Dean of the College of Engineering and to the Graduate Council, and was approved as partial fulfillment of the requirements for the degree of Doctor of Philosophy.

April 23, 1966

_____
Dean, College of Engineering

_____
Dean, Graduate School

Supervisory Committee:

_____
Chairman

_____
E. H. Hadlock

_____